Geologic Framework Models for the Alluvial Basin Reference Case

Spent Fuel and Waste Disposition

Prepared for
U.S. Department of Energy
Spent Fuel and Waste Science and Technology
Milestone M3SF-20LA010304022

Los Alamos National Laboratory
M. Gross, E. Miller, D. Milazzo, T.A. Miller, A. Lavadie-Bulnes, E. Swanson, N. Hayes-Rich, R. Roback, P.H. Stauffer

Sandia National Laboratories
T. LaForce and M.S. Ebeida

July 31, 2020

Los Alamos National Laboratory Document **LA-UR-20-25594**

Disclaimer

Appendix E

Revision 6
10/7/2019

APPENDIX E
NFCSC DOCUMENT COVER SHEET[1]

Name/Title of Deliverable/Milestone/Revision No.	Geologic Framework Models for the Alluvial Basin Reference Case / Milestone M3SF-20LA010304022 / Revision No. 1
Work Package Title and Number	GDSA - Geologic Modeling - LANL/ SF-20LA01030402
Work Package WBS Number	1.08.01.03.04
Responsible Work Package Manager	Michael Gross / Michael R. Gross (Name/Signature)
Date Submitted	Original submission: 07/31/2020; Revision submitted 08/24/2020

Quality Rigor Level for Deliverable/Milestone[2]	☐ QRL-1 ☐ Nuclear Data	☐ QRL-2	☒ QRL-3	☐ QRL-4 Lab QA Program[3]

This deliverable was prepared in accordance with Los Alamos National Laboratory
(Participant/National Laboratory Name)

QA program which meets the requirements of

☒ DOE Order 414.1 ☐ NQA-1 ☐ Other

This Deliverable was subjected to:

☒ Technical Review ☐ Peer Review

Technical Review (TR)
Review Documentation Provided

☐ Signed TR Report or,
☐ Signed TR Concurrence Sheet or,
☒ Signature of TR Reviewer(s) below

Peer Review (PR)
Review Documentation Provided

☐ Signed PR Report or,
☐ Signed PR Concurrence Sheet or,
☐ Signature of PR Reviewer(s) below

Name and Signature of Reviewers

Florie Caporusco / Florie Caporuscio
Kirsten Sauer / Kirsten B. Sauer

NOTE 1: *Appendix E should be filled out and submitted with the deliverable. Or, if the PICS:NE system permits, completely enter all applicable information in the PICS:NE Deliverable Form. The requirement is to ensure that all applicable information is entered either in the PICS:NE system or by using the NFCSC Document Cover Sheet.*

- *In some cases there may be a milestone where an item is being fabricated, maintenance is being performed on a facility, or a document is being issued through a formal document control process where it specifically calls out a formal review of the document. In these cases, documentation (e.g., inspection report, maintenance request, work planning package documentation or the documented review of the issued document through the document control process) of the completion of the activity, along with the Document Cover Sheet, is sufficient to demonstrate achieving the milestone.*

NOTE 2: *If QRL 1, 2, or 3 is not assigned, then the QRL 4 box must be checked, and the work is understood to be performed using laboratory QA requirements. This includes any deliverable developed in conformance with the respective National Laboratory / Participant, DOE or NNSA-approved QA Program.*

NOTE 3: *If the lab has an NQA-1 program and the work to be conducted requires an NQA-1 program, then the QRL-1 box must be checked in the work Package and on the Appendix E cover sheet and the work must be performed in accordance with the Lab's NQA-1 program. The QRL-4 box should not be checked.*

Table of Contents

List of Figures

List of Tables

List of Acronyms

AoI	area of interest
DEM	digital elevation model
DOE	Department of Energy
DOE-EM	DOE Office of Environmental Management
DOE-NE	DOE Office of Nuclear Energy
EBS	engineered barrier system
ESRI	Environmental Systems Research Institute
FEHM	Finite Element Heat and Mass Transfer (simulation code)
FY	fiscal year (October-September)
GDACC	Geospatial Data Acquisition Coordination Committee
GDSA	geologic disposal safety assessment
GFM	geologic framework model
HLW	high level nuclear waste
HSU	hydrostratigraphic units
LaGriT	Los Alamos Grid Toolbox
LANL	Los Alamos National Laboratory
LFA	lithofacies assemblages
Ma	millions of years ago
MD	measured depth
MSL	mean sea level (amsl = above mean sea level; bmsl = below mean sea level)
NMBGMR	New Mexico Bureau of Geology and Mineral Resources
PA	performance assessment
PFLOTRAN	Parallel Flow and Transport (simulation code)
R&D	research and development
RGIS	New Mexico Resource Geographic Information System
SFWD	Spent Fuel & Waste Disposition (DOE-NE program)
SFWST	Spent Fuel and Waste Science and Technology (DOE-NE program)
SGS	sequential gaussian simulation
SNF	spent nuclear fuel
SNL	Sandia National Laboratories
TGS	truncated gaussian simulation
TOUGH	Transport of Unsaturated Groundwater and Heat (simulation code)
TVDSS	true vertical depth sub-sea
US	United States
USGS	United States Geological Survey
UWI	unique well identifier
UZ	unsaturated zone
VoI	volume of interest
WFMF	West Florida Mountain Fault

1 Introduction

This report summarizes research conducted in FY20 on the geologic characterization of alluvial basins as potential repositories for nuclear waste. This project supports the Spent Fuel and Waste Science and Technology Campaign (SFWST) of the U.S. Department of Energy Office of Nuclear Energy, Office of Spent Fuel and Waste Disposition (SFWD). The team was tasked with developing techniques and workflows for creating a regional-scale geologic framework model (GFM) of a generic alluvial basin using publicly available data, e.g., published maps, scientific reports and journal articles. We used the Baker Hughes JewelSuite™ Subsurface Modeling software to generate a comprehensive basin-scale GFM that accounts for subsurface complexities inherent to alluvial basins, such as highly variable sediment thickness, unmapped buried faults and complex lithofacies relationships. We follow-up on last year's regional study of the Mimbres Basin with a focused effort on one of its sub-basins, the Deming sub-basin, located in the Basin and Range province of southwestern New Mexico (Figure 1-1). The Deming sub-basin was selected as the study area because it has never been characterized for repository potential, and thus typifies a generic alluvial basin during the phase of initial reconnaissance.

Following the introduction, Chapter 2 presents an overview of the geologic setting and descriptions of the data inputs for the GFM. We also present a summary of the dominant depositional environments during formation of the alluvial sediments and the resulting distribution of lithofacies across the Deming sub-basin. An interpreted cross-section of alluvium perpendicular to the basin axis is also presented as the conceptual framework for lithofacies modeling. The workflow for GFM construction is described in Chapter 3. Data preparation and model construction is of paramount importance, as the success of downstream modeling relies upon the integrity of the GFM. We started with a basic GFM that consists of only two surfaces and three normal faults that divide the volume into two main lithologic units: alluvium and bedrock. Chapter 4 presents increased GFM complexity with the results of facies and property modeling at the sub-basin scale. Various degrees of complexity and geostatistical parameters were explored. Chapter 5 provides details of a small volume of the GFM that served as a test case to establish a working interface between the GFM software and the computational meshing programs (LaGriT and Vorocrust) developed at Los Alamos and Sandia National Laboratories. Finally, Chapter 6 tests the computational meshes of the small volume with the FEHM (FEHM, 2020) and PFLOTRAN (PFLOTRAN, 2020) multiphase porous flow and chemical transport simulators. The results are promising and suggest the subsurface complexity captured by GFMs can be incorporated into the simulators to account for geologic heterogeneity in alluvial basins.

Advances made during FY20 for the GDSA alluvium reference case include:

- Development of a GFM for the Deming sub-basin (~30 x 20 km) with three main normal faults and two lithologic units (alluvium and bedrock).
- Interpretation of alluvial lithofacies distribution in a basin-normal cross section.
- Generation of facies models for different levels of geologic complexity in the alluvium.

- Stochastic modeling in 3D of porosity and permeability for the sub-basin volume.
- Established a workflow that facilitates a seamless transition from JewelSuite™ to LaGriT to FEHM/PFLOTRAN that demonstrates the capability to tackle complex geologic data and create realistic numerical meshes.
- Successful porous flow simulations on meshes created from the GFM using FEHM and PFLOTRAN for cases of saturated and unsaturated flow with isotropic and heterogeneous permeability distributions.

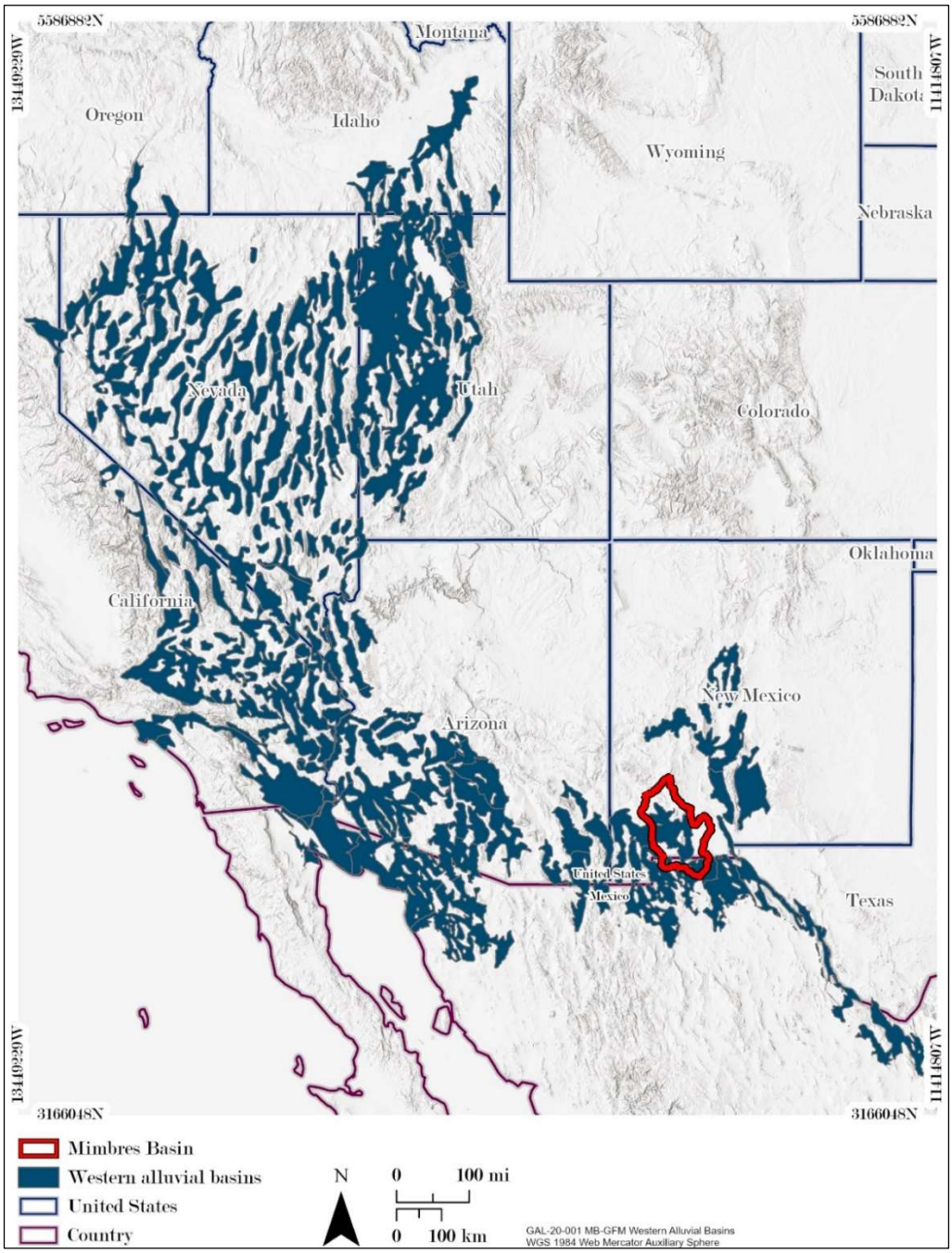

Figure 1-1: Alluvial basins of the Basin and Range province in western North America, with the outline of the Mimbres Basin in southwestern New Mexico.

2 Overview of the Deming Sub-Basin

2.1 Tectonic & Geologic Setting

The Mimbres Basin of southwestern New Mexico, located in the eastern-most sector of the southern Basin and Range province (Figure 2-1), formed as a result of east-west regional extension from the Middle Miocene (~15 Ma) to present. The basin consists of north- and northwest-trending mountain ranges underlain by Precambrian to Tertiary age bedrock. These mountain ranges divide the Mimbres Basin into a series of fault-bounded sub-basins that are filled with alluvial sediments, in some cases more than 1 km thick. A more detailed description of Mimbres Basin geology may be found in our FY19 report (Gross et al., 2019).

In FY19, we focused our modeling efforts on the bedrock geology and structural elements, i.e., building the "container" in which the alluvial sediments are deposited. In FY20, our primary focus is on the alluvial material filling up the container, which represents the repository medium. The FY20 Area of Interest (AoI) encompasses an area of the Deming sub-basin defined by a rectangle with sides of 30 km and 20 km (Figure 2-1). The rectangle, along with a series of orthogonal cross sections, are aligned with the local NNE-SSW structural trend (Figure 2-2). The main structural feature in the AoI is the West Florida Mountain Fault (WFMF), a west-dipping normal fault that appears on published geologic maps (NMBGMR, 2003) and bounds the Deming sub-basin to the east (labeled "Eastern Fault" in Figure 2-2). Two additional normal faults were identified in FY19 (Gross et al., 2019), a synthetic fault that parallels the WFMF ("Central Fault") and an antithetic, east-dipping fault ("Western Fault") that marks the western boundary of the Deming sub-basin. The overall basin structure resembles a half-graben, with the underlying bedrock strata dipping 5 to 10 degrees to the east (Figure 2-3). The basin asymmetry can be observed in maps of alluvial thickness derived from gravity surveys (Heywood, 2002), with the main depocenter in the hanging wall of the WFMF (Figure 2-4).

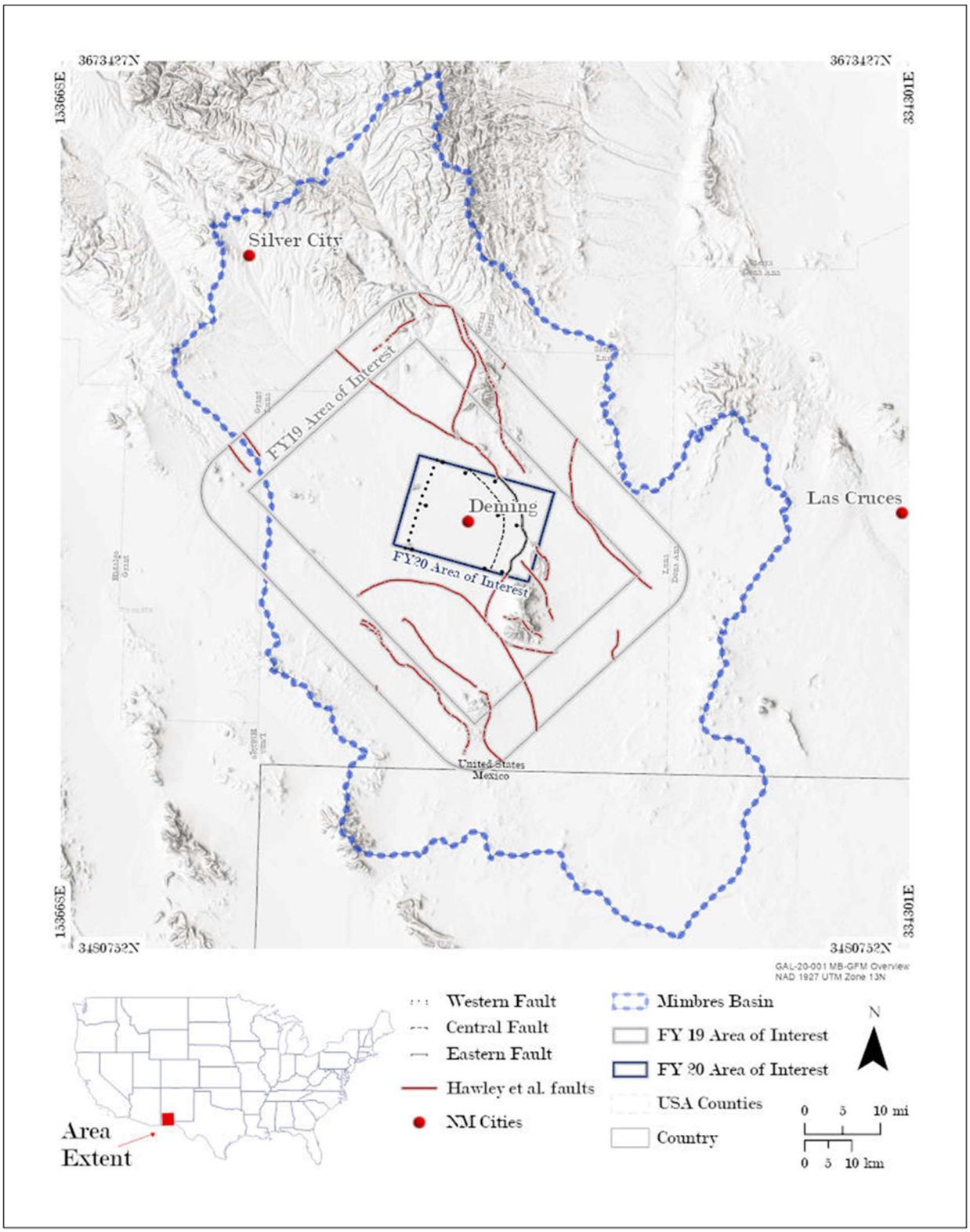

Figure 2-1: Shaded relief map of the Mimbres Basin showing FY19 and FY20 areas of interest, regional faults from Hawley et al. (2000) and the three normal faults incorporated into the geologic framework model (GFM).

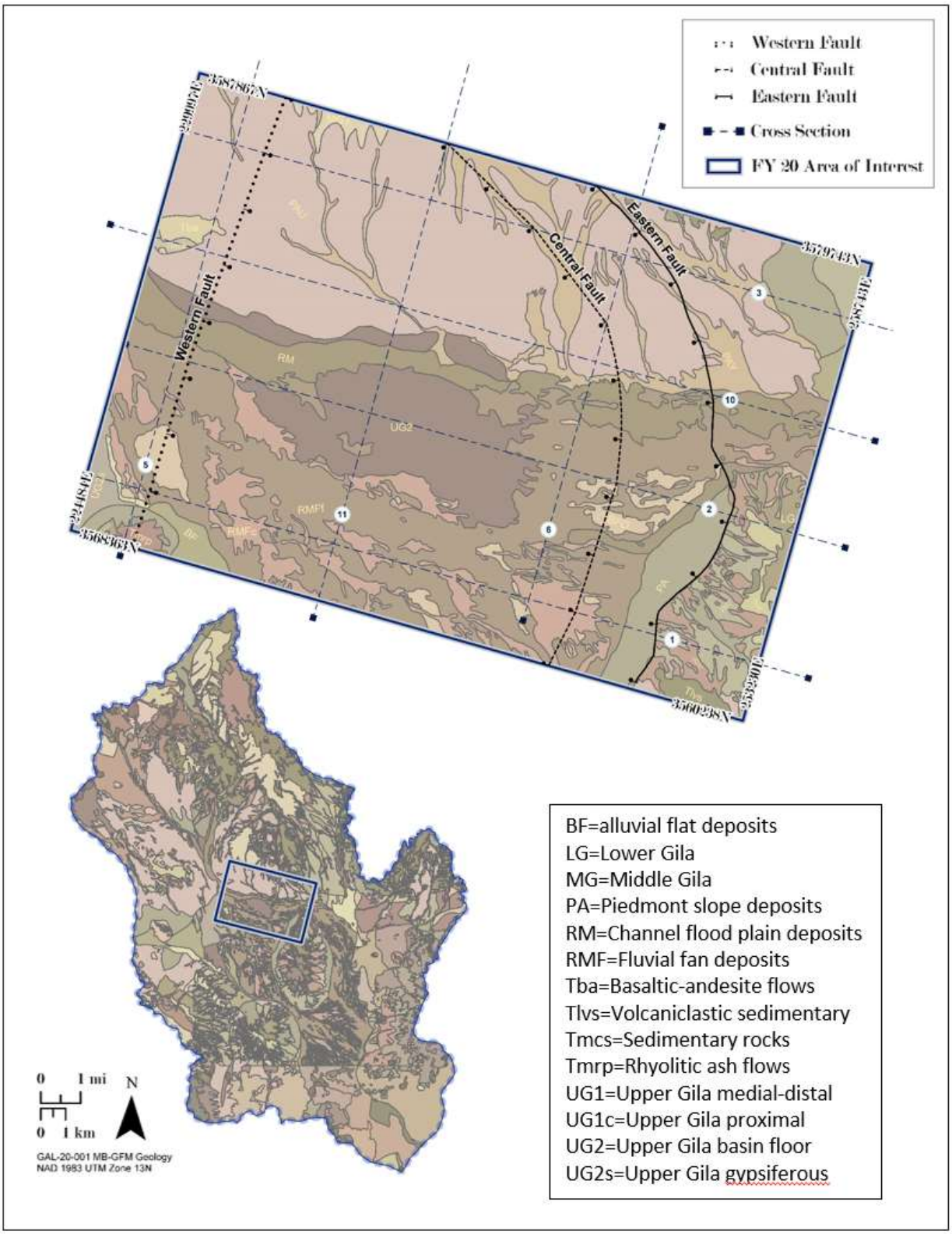

Figure 2-2: Surface geologic map adapted from Hawley et al. (2000) for the FY20 AoI including main normal faults and numbered cross section lines used to build the GFM.

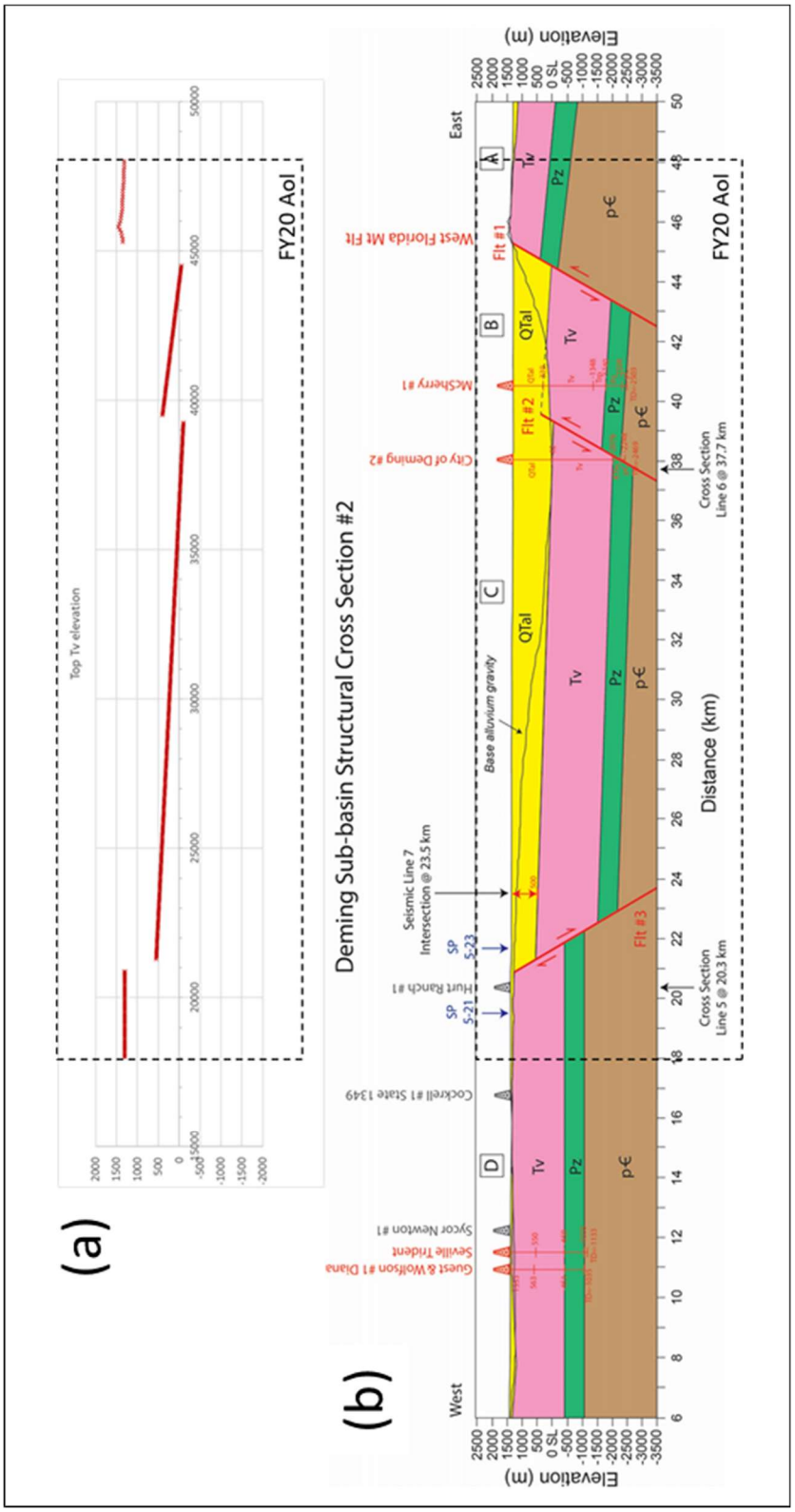

Figure 2-3: (a) Sampling of bedrock elevation points (Top Tv) from cross section #2 at 50 m spacing for the FY20 AoI; (b) Structural cross-section #2 across the Deming sub-basin (refer to Figure 3-2 for location) showing normal faults, down-thrown blocks, tilted strata and accumulation of alluvial sediments (Qtal). pC=Precambrian, Pz=Paleozoic, Tv=Tertiary volcanics, QTal=Quaternary-Tertiary alluvium.

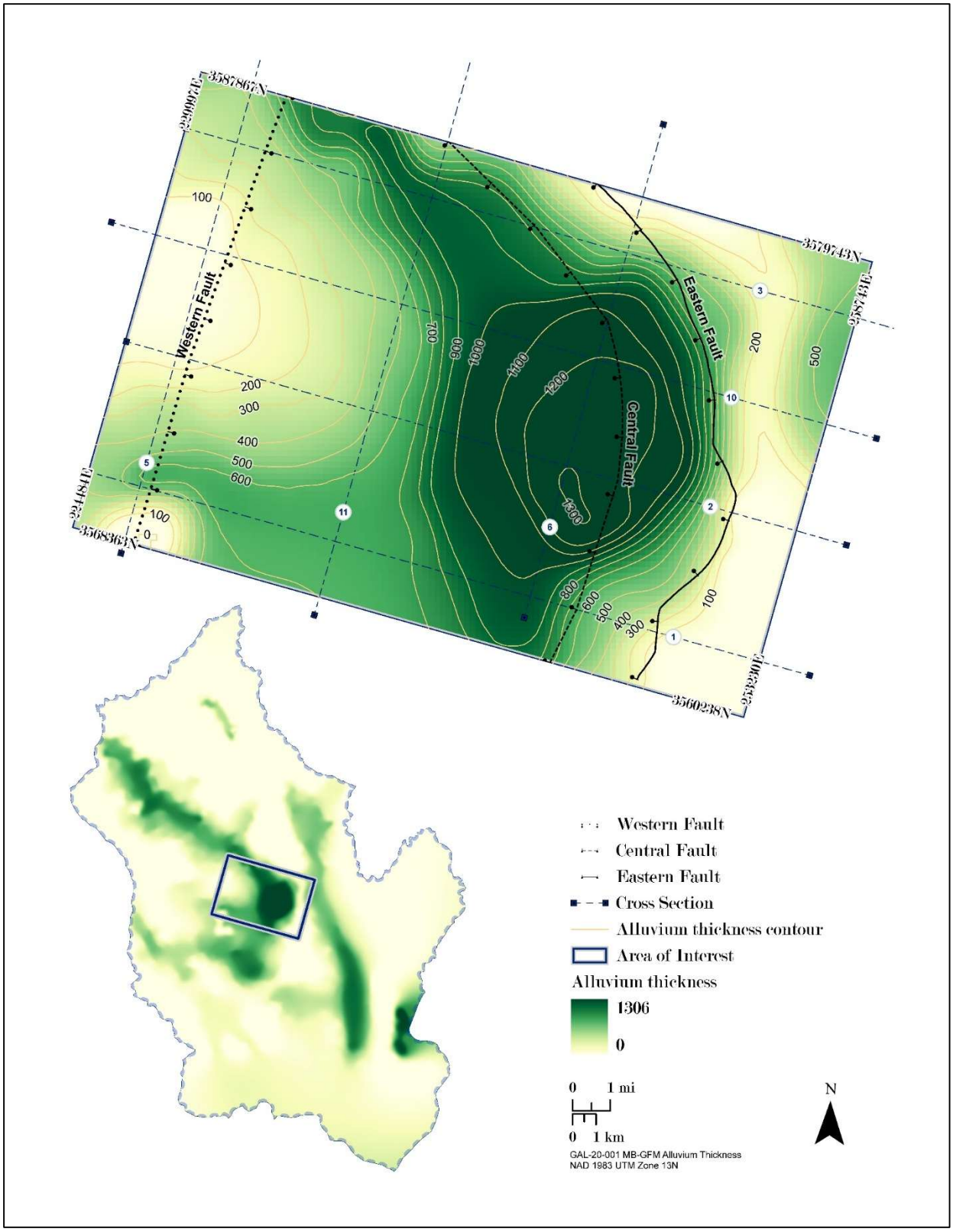

Figure 2-4: Maps of alluvial sediment thickness derived from Heywood (2002) gravity surveys for the entire Mimbres Basin and for the FY20 area of interest.

2.2 Input Data for the Geologic Framework Model

At its core, a geologic framework model consists of a combination of stratigraphic horizons and faults. These surfaces are typically derived from 3D seismic surveys and/or large numbers of wells that intersect the geologic formations of interest (Shepherd, 2009a). As well and seismic survey data are lacking for the Deming sub-basin, we developed alternative methods to characterize the subsurface geology. In addition to the three identified faults in the study area (Figure 2-3), the two other surface horizons derived from geologic mapping include the ground surface and the top of bedrock, which correspond to the upper and lower boundaries of alluvium, respectively. For the ground surface, we used a point cloud representation of a 10 m resolution digital elevation model (Figure 2-5; GDACC, 2018) resampled to 100 m resolution; resampling decreased processing time without sacrificing resolution over such a large AoI. We used synthetic well data derived from cross sections to define the top of bedrock, and resampled all of the cross sections at 50 m spacing to yield a high density of points *(x,y,z)* along each of the seven section lines (Figure 2-2 and Figure 2-3).

We also produced a surface for the top of the water table, using numerous water wells that tap alluvial aquifers in the Deming sub-basin for agricultural irrigation and municipal water supply (Finch et al., 2008; Rinehart et al., 2015). The U.S. Geological Survey and the New Mexico Bureau of Geology and Mineral Resources maintain comprehensive databases of these wells, which include information about the operator, drilling, well construction and measurements of historical water levels. A total of 379 water wells are located within the FY20 AoI, of which 14 contain lithologic descriptions of the alluvial sediments encountered during drilling (Figure 2-6). A pre-development water table was constructed in ArcGIS by applying an inverse distance weighted (IDW) interpolation using “first head” (prior to pumping) water level measurements (Figure 2-7). Contours of the water table reflect the overall northwest to southeast flow of groundwater in the Mimbres Basin, with groundwater diverted around the West Florida Mountains in the southeast corner of the FY20 AoI (Figure 2-7).

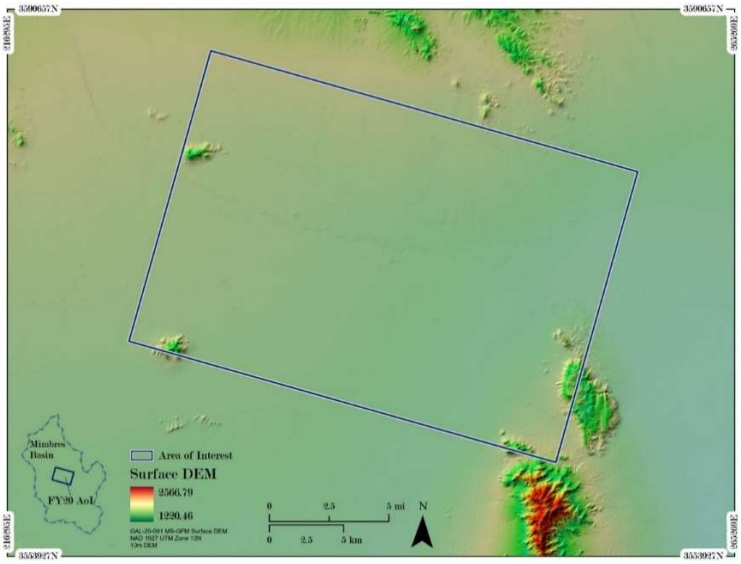

Figure 2-5: Surface digital elevation model (DEM) for the FY20 AoI (GDACC, 2018)

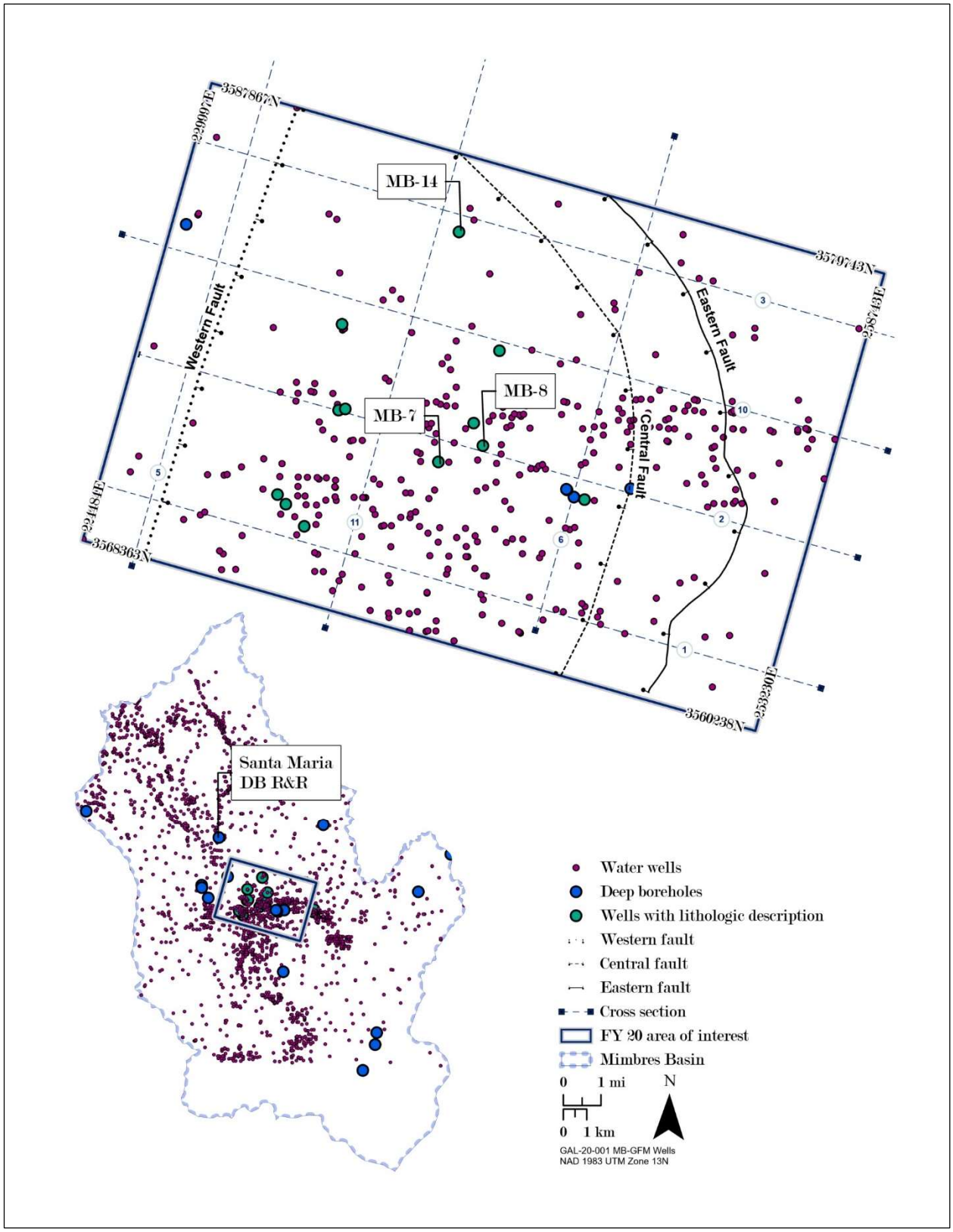

Figure 2-6: Map of water wells in the Mimbres Basin and the FY20 area of interest from the US Geological Survey and the New Mexico Bureau of Geology and Mineral Resources databases as provided by Hawley et al. (2000).

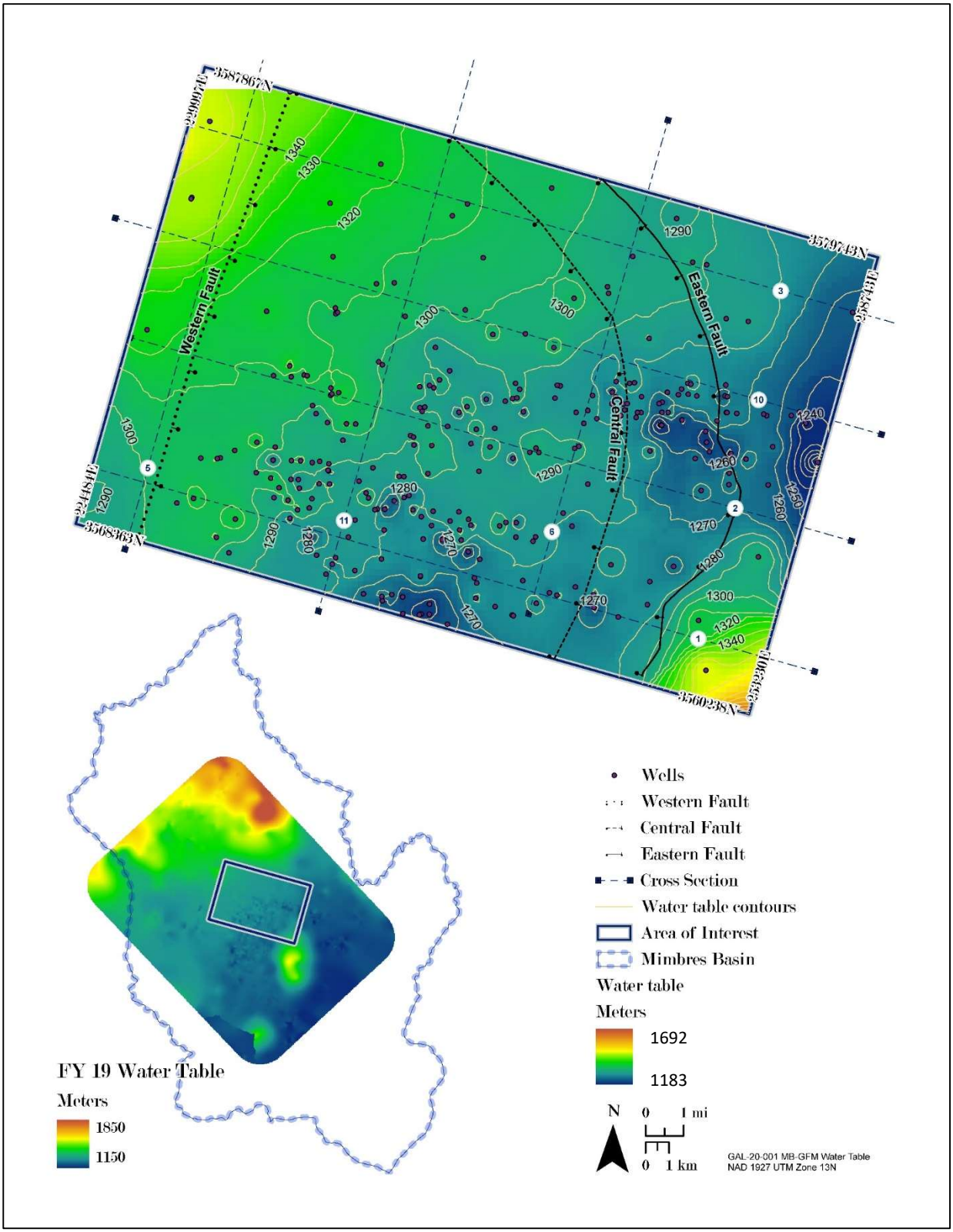

Figure 2-7: Contours of pre-development water table elevation for the FY20 area of interest.

2.3 Alluvial Facies & Interpreted Cross Section

An important component of this year's study is to provide a framework for modeling the distribution of alluvial lithofacies in a generic alluvial basin. Ideally, there would be boreholes with lithologic descriptions of the complete alluvial section. However, because borehole information for the Deming sub-basin is lacking, we rely upon evidence from (1) depositional environments, (2) climate fluctuations, (3) lithologic descriptions of shallow water wells, (4) surface geologic maps (Hawley et al., 2000; Geologic Map of New Mexico 2003) and (5) conceptual models of lithofacies assemblages specific to the Mimbres Basin (Kennedy et al., 2000). Depositional environment exerts a primary control on the physical and hydrologic properties of basin-fill sediment. For example, a channel that deposits material only during high-energy floods will generate much coarser-grained, permeable material than a playa or lake in which clays accumulate in low energy environments.

The following paragraphs describe the geologic interpretations of the study area that were used to build the cross section of alluvial lithofacies in Figure 2-8. This cross section was constructed normal to the basin axis in the plane of structural cross section number 2 (Figure 2-2).

Intermontane regions within the Mimbres Basin consist of broad piedmont-alluvial fans on the margins grading basinward into playa-lake depressions, with some fluvial deposits along valley axes (Hawley et al., 2000). The alluvial fans are generally coarse-grained, whereas the fluvial and lacustrine deposits range in grain size from coarse to fine (Kennedy et al., 2000). The fluvial/lacustrine mix depends on the position of the river and its channels, and whether the river flowed through the channel and exited the basin or drained internally to a low-energy lake at various times in its history. The available sedimentary record suggests at least two lake-forming events in the Deming sub-basin.

The most recent lake-forming event likely occurred in the Pleistocene, when the lower part of the Mimbres Basin flooded in an event referred to as pluvial Lake Palomas (Love and Seager, 1996; Hawley et al., 2000). According to Love and Seager (1996), the highest stand of pluvial Lake Palomas in the downstream Bolson (a flat desert valley that drains into a playa) de Los Muertos was at an elevation of 1225 m. This elevation is too low to have flooded the Deming sub-basin. However, flooding downstream indicates a wetter than normal climate in the Pleistocene, which suggests the presence of a lake in the deepest part of our AoI. The presence of a Pleistocene lake is supported by water well data, with wells MB-7 and MB-8 indicating a layer of "clay/caliche" at depths of 20–40 m. We assumed a limited distribution for the lake deposits based on the extent of observations in wells MB-7 and MB-8. However, this assumption is likely a conservative estimate, given that other well logs may not have included descriptions of caliche.

Evidence for an older (i.e., pre-Pleistocene) lake-forming event is provided by a substantial (25–30 m) clay-rich section in the Santa-Maria DB (SMDB) well located approximately 8 km northwest of the FY20 AoI (Figure 2-6). This well is upstream from the Deming depocenter, where the deepest part of the lake would likely have been, implying an extensive lake

throughout the sub-basin. Within the SMDB well there are 175 m of sediment deposited above the clay-rich lacustrine interval, indicating this earlier lake event pre-dates the post-Gila units, which are less than 60 m thick throughout the region (Hawley et al., 2000). We projected this older lacustrine unit downstream at similar elevations to those observed in the SMDB well and assigned a greater thickness due to its position in the basin depocenter, therefore placing it within the Upper Gila group (Figure 2-8).

Alluvial fans (piedmont slope deposits) sourced from footwall mountains provide another major source of basin-fill material. The distance these fans extend from the mountain front varies as a function of depth in response to changing fault activity through time. Three main alluvial fan units are associated with the three main faults in the study area. The modern extent of the fan in the hanging wall of the West Florida Mountains Fault, measured from the Hawley et al. (2000) Plate 1 map, is 1.5 km. We assume the fan had less extent in the past when the synthetic Central Fault was also active and accommodating extension in the basin. The modern fan from the Treasure Mountains, north of the West Florida Mountains, is 3–5 km in extent except where dissected by the Rio Mimbres (Hawley et al., 2000). The MB-14 well, located 2.5 km from the interpreted trace of the Central Fault, contains “fanglomerate” below a depth of 53 m. The fanglomerate deposits could be attributed to tectonic activity on the Central Fault, although this seems unlikely given that fluvial deposits are present on both sides of the Central Fault (i.e., no upland source for sediments). Thus, we attribute the alluvial fan sediments observed at MB-14 to the Eastern Fault. The Western Fault has no constraints on its fan size; thus we assumed a moderate lateral fan extent compared to the other two fans in light of its intermediate amount of extensional slip. The three prominent alluvial fan units are seen in the downthrown structural blocks adjacent to the three normal faults (Figure 2-8).

The remaining basin-fill materials include fluvial units characterized by a mix of gravel, sand, silt and clay. The fluvial units are divided into the Lower Gila, Middle Gila and Upper Gila, and post-Gila units according to the proportions shown in the Hawley et al. (2000) cross sections (Figure 2-8). These distinctions are made based on age differences and inferred cementation rather than distinct depositional settings.

The Lower Gila is divided into a channel deposit and an overbank/floodplain deposit (Figure 2-8). The fluvial channels consist of a higher proportion of sandstone and conglomerate, whereas the overbank/floodplain deposits contain a higher proportion of siltstone and mudstone. The placement of the boundary between the two units is unconstrained, although the channel is located along the Central Fault as it is assumed to be the most active fault during deposition given the depth of basin sediments at that location. By the time of deposition of the Middle Gila unit, we assume the channel had migrated across the entire fluvial part of the basin.

Post-Gila units, referred to as the Mimbres alluvial fan in Figure 2-8, are based on the Hawley et al. (2000) modern map of surficial geology, which shows large early Pleistocene fluvial deposits across the entire Mimbres River Basin (Figure 2-2). These sediments are less consolidated than

the older fluvial units and thicken toward the north where water from the Rio Mimbres has occasionally flowed in the recent past.

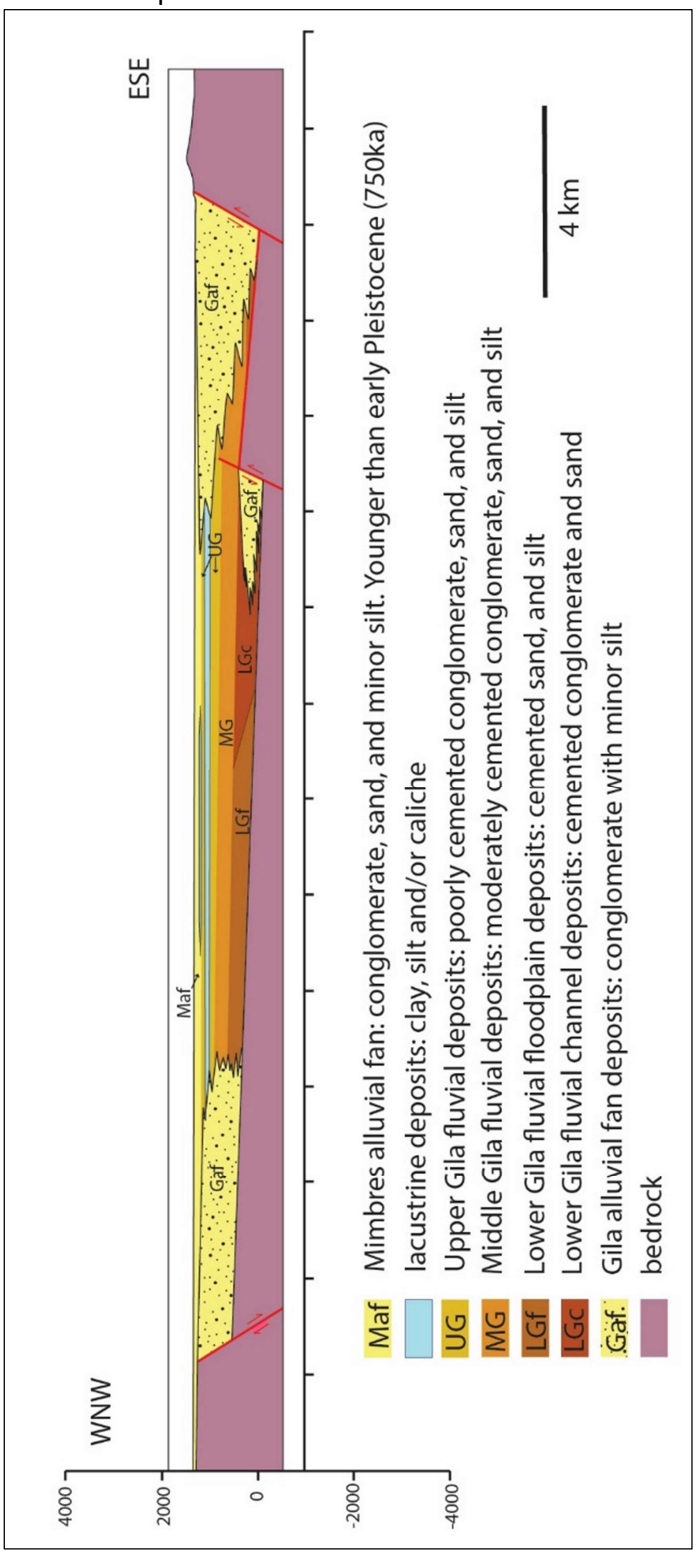

Figure 2-8: Cross-section showing the distribution of alluvial lithofacies in the basin-fill sediments along cross-section line #2 (Figure 3-2) of the Deming sub-basin. Facies distributions are schematic with extents as described in the text. Elevation in meters with respect to mean sea level. No vertical exaggeration.

3 Geologic Framework Model of the Deming Sub-Basin

3.1 Overview of the GFM workflow

Our geologic framework model (GFM) provides the opportunity to visualize geometries, quantify homo- and heterogeneous basin properties, and run numerical simulations on 3-D reservoir volumes at various scales and resolutions. GFMs are ideally suited to characterize alluvial basins for repository considerations because of their (1) ability to integrate and visualize a wide range of subsurface datasets, (2) robust geostatistical capabilities, and (3) ability to produce complex mesh properties for advanced flow and transport simulators such as PFLOTRAN and FEHM. We used the Baker Hughes JewelSuite™ 2019.4 software package to first build the GFM and then incorporate facies and property modeling parameters. The unconventional nature of our input data (structural cross-sections rather than seismic and well data) and model interaction with the ground surface posed some challenges for the software, which we were able to overcome by developing unique workflow solutions not covered in the JewelSuite™ handbook and consulting with Baker Hughes advisors. These solutions, many unique to alluvial basins, will be detailed in a forthcoming training manual in FY21.

We created two GFMs: (1) a basin scale GFM that we used to assign physical properties to distributed alluvial lithofacies, and (2) a smaller GFM, represented as a thin slice across the Central Fault. We used this smaller GFM to test file formats for export to numerical meshing and flow and transport modeling. Both GFMs originated from the same input data and were created using the workflow described below. The high-level overview of steps is as follows:

- Import data (cross-sectional, horizon marker, and surface elevation data)
- Create faults
- Create the top of bedrock surface
- Create a watertight volume
- Create a 3D Grid and a 3D Mesh
- Create output files for downstream analysis

3.2 Importing data to JewelSuite™

Cross-sectional data were imported into JewelSuite™ as pairs of well files in space-delimited text format: one file with well name, depth, and geographic coordinates, and a second file with marker horizon information. The single marker horizon of interest is the top of bedrock, which corresponds to Tertiary volcanics throughout the AoI. Each sampling point of the structural cross-section (e.g., Figure 2-3a) is represented in JewelSuite™ by a vertical well, with gaps in the cross-section lines indicating horizontal fault separation of the marker horizon (Figure 3-1). For these synthetic wells, elevation of the bedrock marker top is shown as color coded points in

Figure 3-2. This distribution of elevation points served as the input data for generating the top of bedrock surface.

The ground surface (top of alluvium, or top of bedrock where alluvium is absent) was generated from the GDACC (2018) digital elevation model (DEM) and resampled to 100 m resolution to aid with processing time (Figure 3-3). The DEM was imported as a point set to create a tri-mesh surface (Figure 3-4).

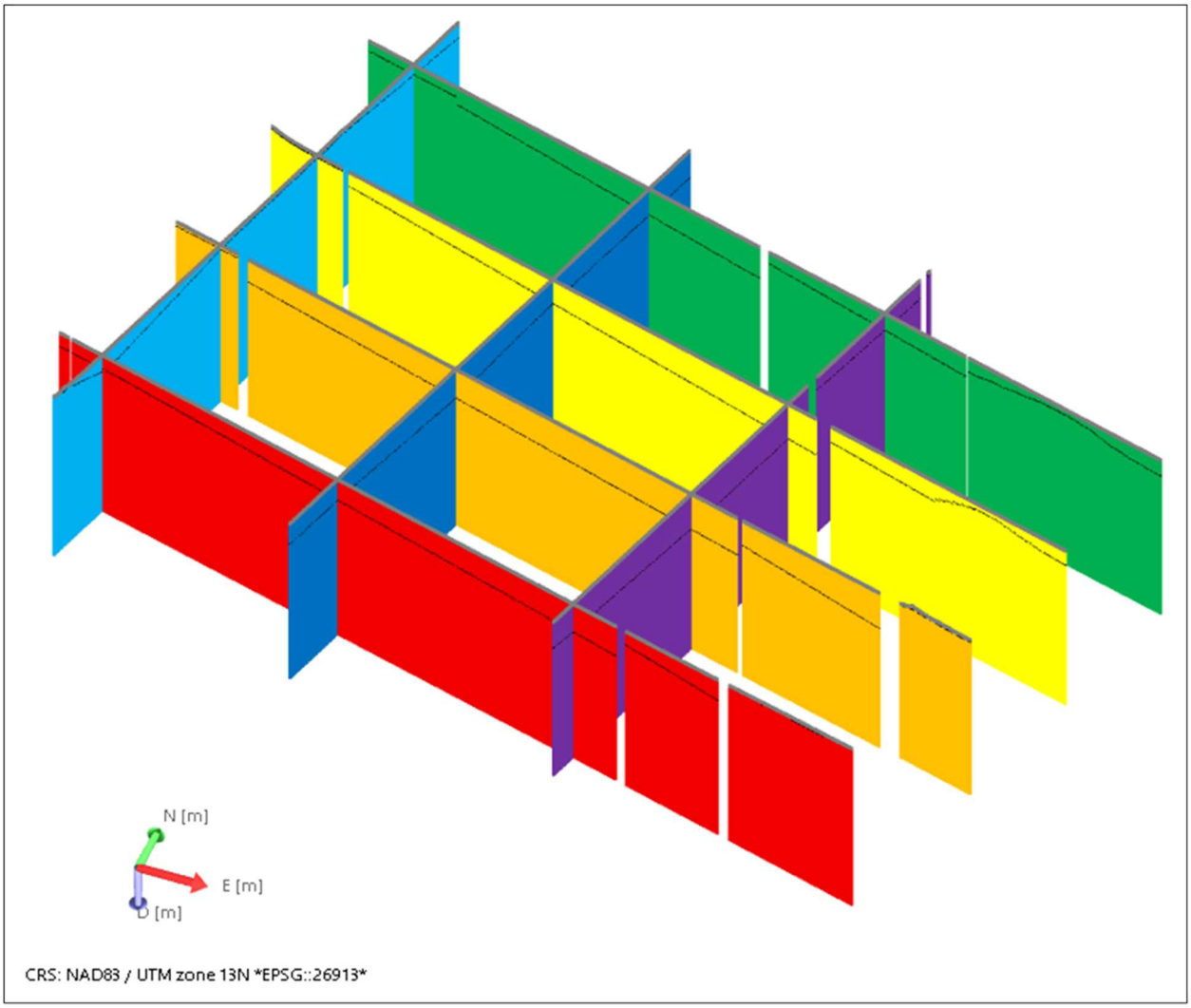

Figure 3-1: Cross-section lines comprised of vertical wells after import. The marker horizon (top of bedrock) are the black lines on each section. Gaps in the cross-sections indicate positions of normal faults.

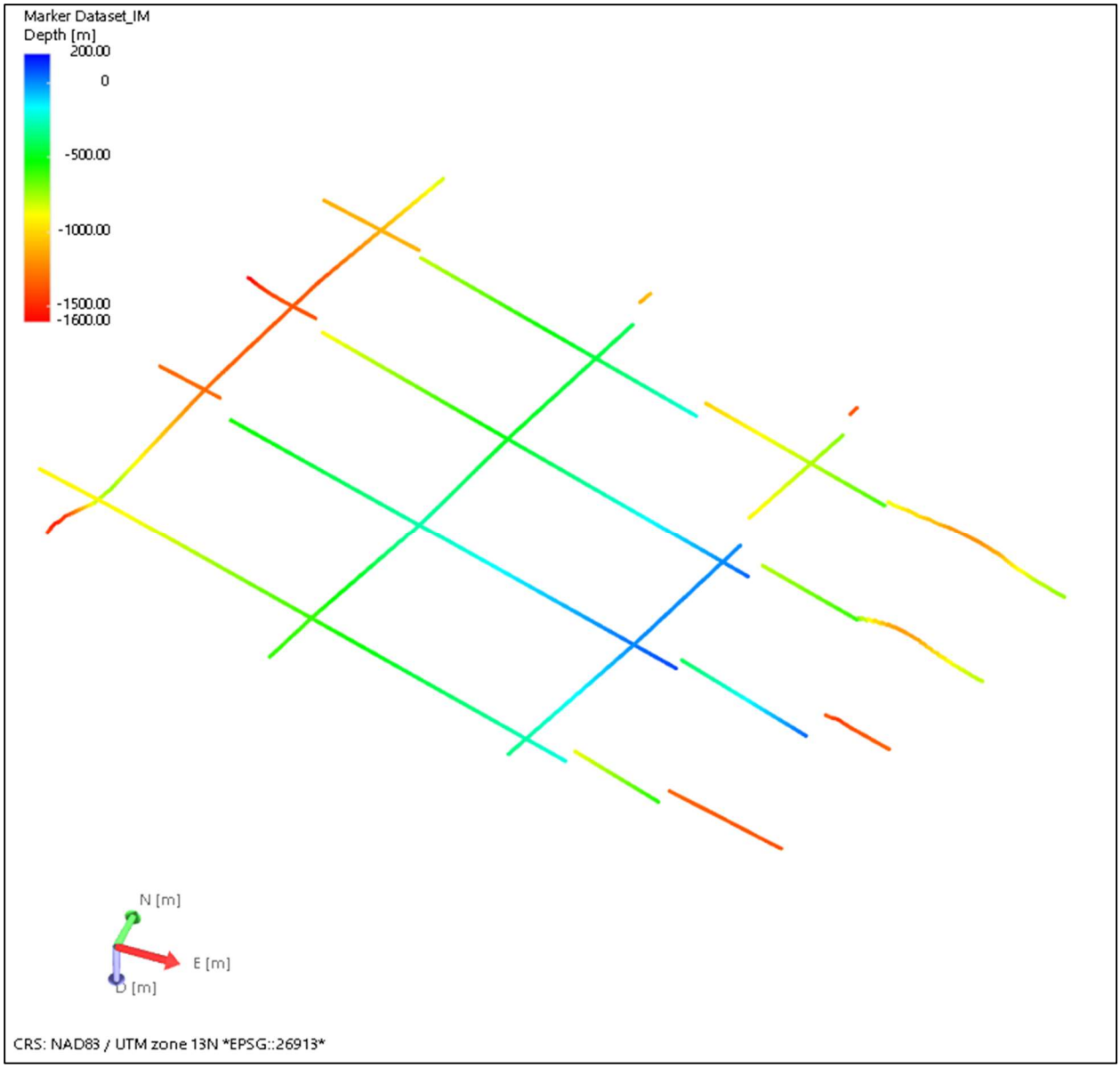

Figure 3-2: Well markers for the top of Tertiary bedrock represented by points sampled at 50 m spacing. Marker tops are color-coded by depth (TVDSS=true vertical depth sub-sea) such that positive values are depth below sea level and negative values are depth above sea level.

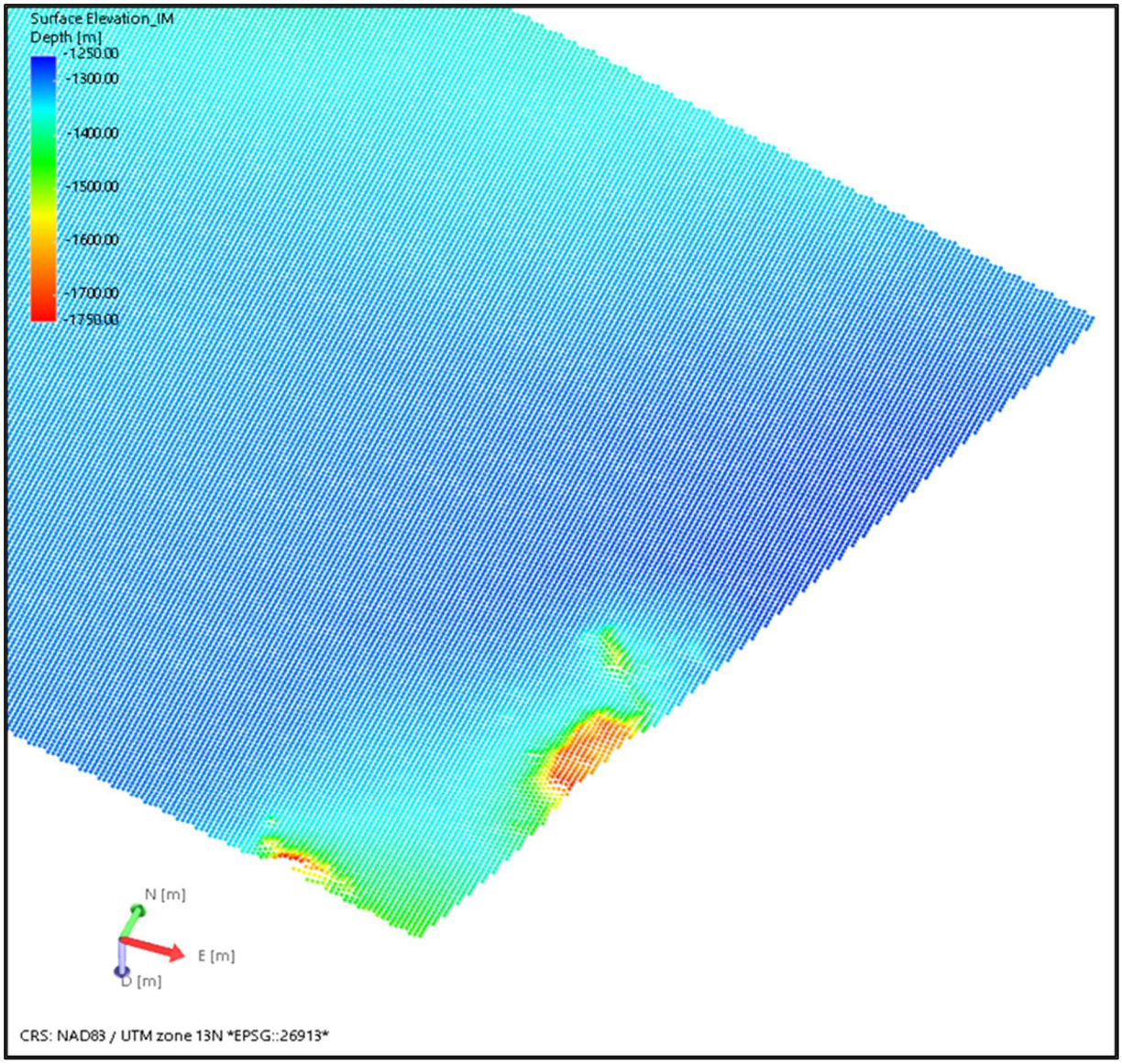

Figure 3-3 Close-up of the DEM point set data prior to creating the tri-mesh surface.

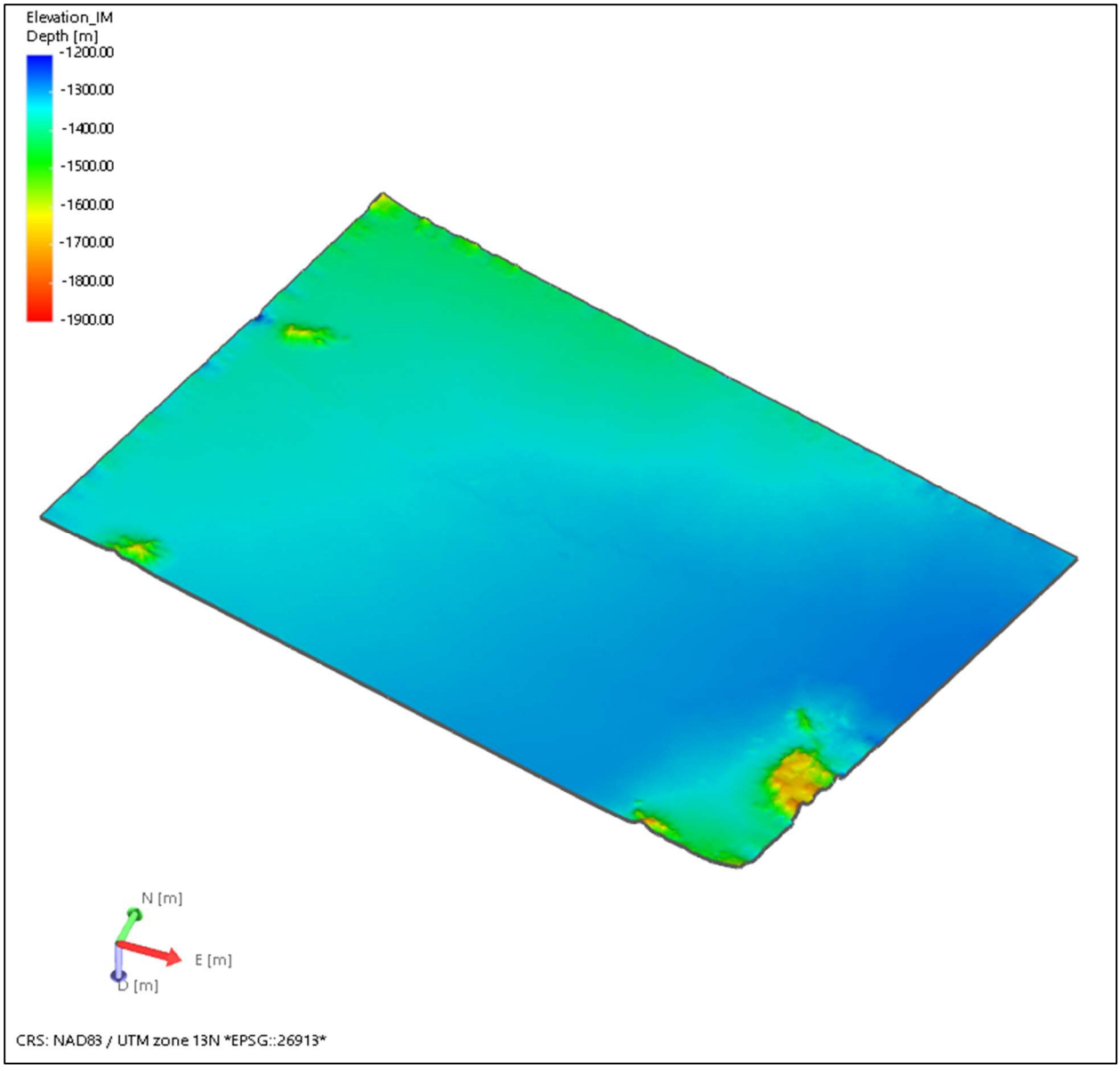

Figure 3-4: Tri-mesh output of the "Create Surface" workflow in JewelSuite™, representing the ground surface elevation in the AoI. Note the high elevations represent bedrock outcrops whereas the flat, low-lying areas represent basin-fill sediment.

3.3 Creating faults in JewelSuite™

The standard technique for creating faults in a GFM involves interpreting fault traces ("fault sticks") on vertical seismic lines and then fitting surfaces to each family of fault sticks (Shepherd, 2009a). However, this fault generation workflow was not appropriate for our model since we did not have access to seismic data. Rather, for our model we started by digitizing the three fault traces projected onto the ground surface, with each fault assigned to its own polyline file (Figure 3-5). We then quadruplicated each polyline file and shifted the duplicates downward (below the bottom of the model) with pure dip-slip motion so that the fault

maintained a 60° dip, consistent with the structural cross sections (e.g., Figure 2-3b). For our GFM, we found that four polylines for each fault proved optimal for fault surface generation, though additional polylines can be created for each fault that extend above and below the volume of interest to ensure better surface triangulation results. Fault surfaces were created for each parallel set of polylines using the JewelSuite™ "Triangulate" interpolation method. Initially the faults extended above and below the volume of interest (Figure 3-6). The fault surfaces were then truncated using a mix of editing and tri-mesh clean-up tools to reflect the structural interpretation of the Eastern Fault (WFMF) exposed on the earth's surface and the buried Central and Western Faults (Figure 3-7).

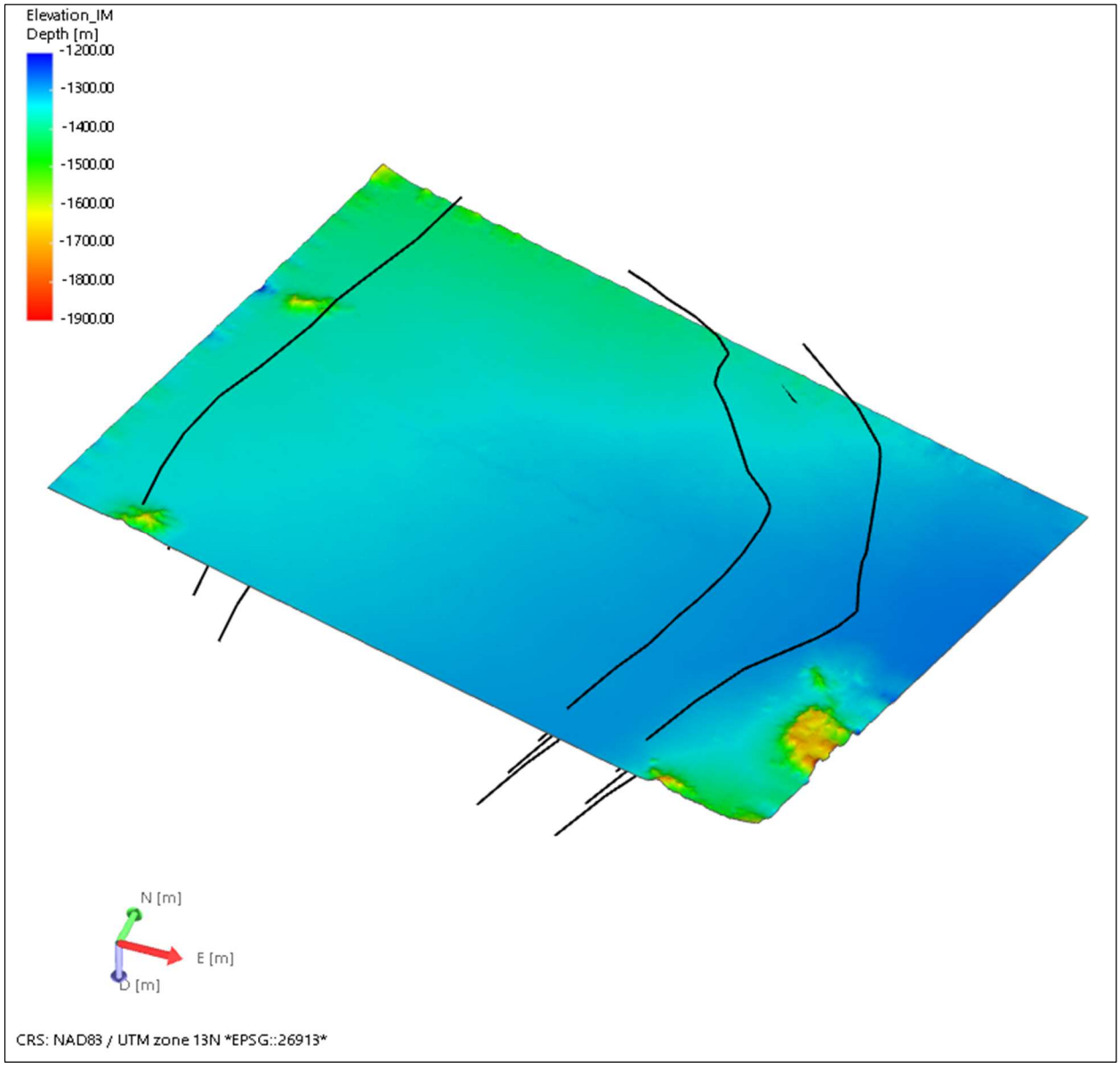

Figure 3-5: Polylines of fault traces used to generate the three fault surfaces with ground surface as reference.

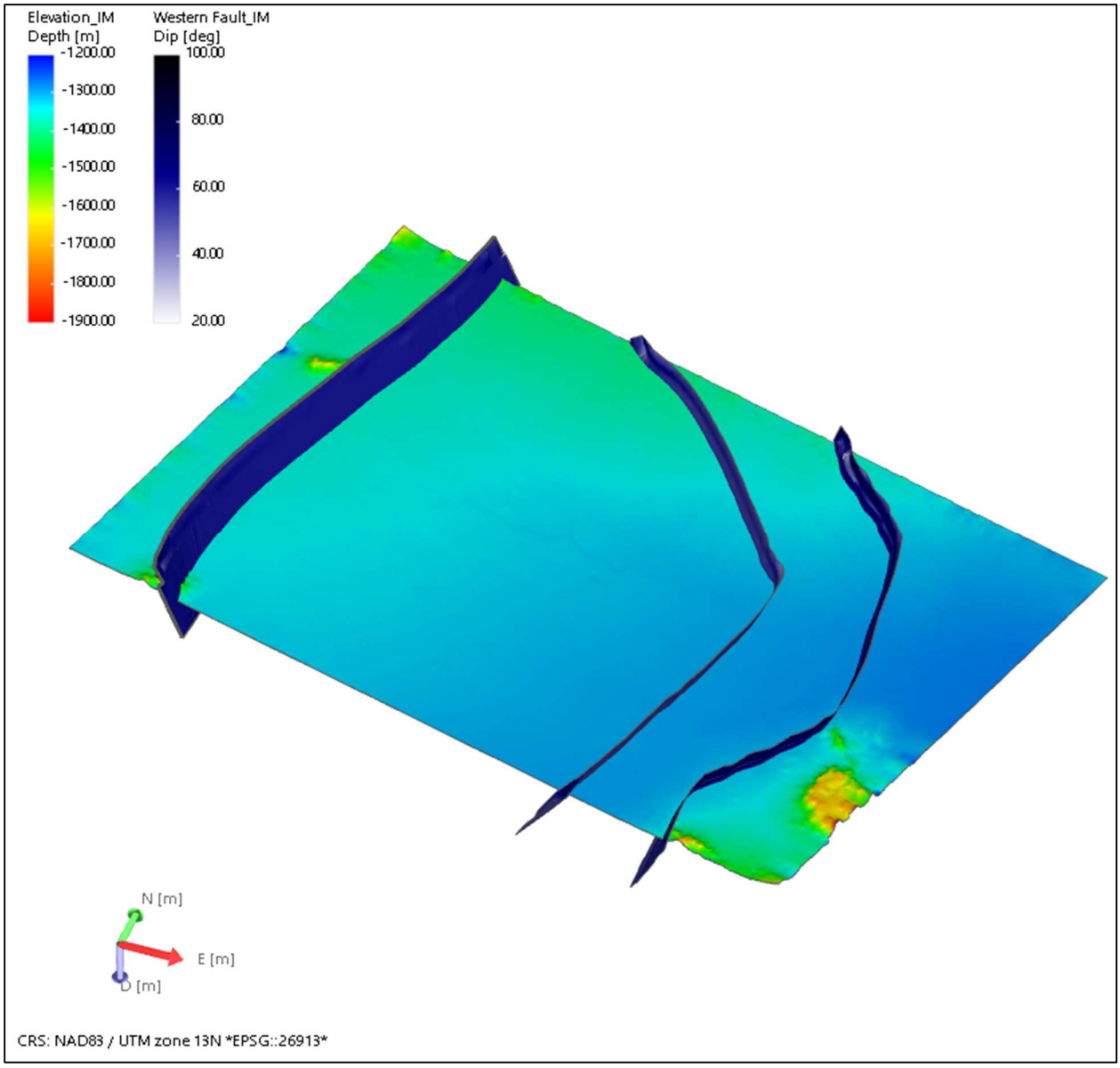

Figure 3-6: Results of the fault generation workflow prior to truncation. Note faults extend above the ground surface.

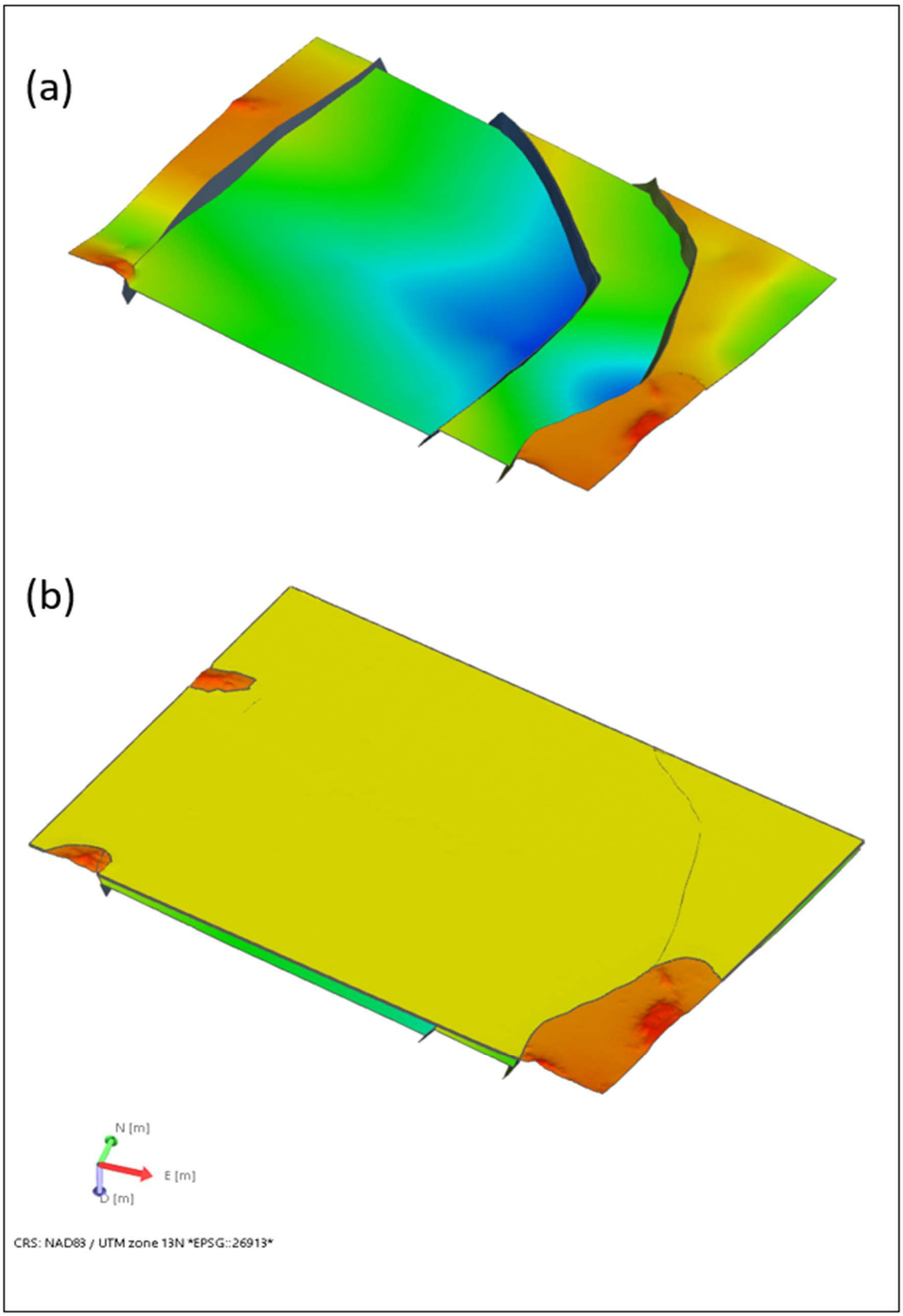

Figure 3-7: Final results of the fault generation workflow. (a) Faults with bedrock surface as reference; (b) Faults with ground surface as reference. Note only the Eastern Fault has surface expression.

3.4 Creating the top of bedrock (Top Tertiary volcanics) surface in JewelSuite™

The non-uniform distribution of the synthetic wells and subsequent horizon markers for the top of bedrock made it difficult to follow standard JewelSuite™ workflows for surface generation. As such, creating the top of bedrock surface required a unique approach using the 3D Structure Tool that merged results from the subsurface marker analysis with portions of the DEM-generated surface where alluvium is absent. After creating a point set from the top bedrock marker data and then initiating the 3D Structure Tool, the pivotal step is to select "Conformable to Top" for the layering type. This layering type selection forces the surface created from the top of bedrock points to mirror the topography of the ground surface in locations where no marker data are available. The resulting surface reveals the basin geometry (Figure 3-8), with two deep depocenters in the hanging wall blocks of the Eastern and Central Faults (blue), shallowing in depth toward the half-graben margins (green to yellow) and bright orange where bedrock is exposed on the surface. This method provides a smooth interpolation of the surface despite the grid-like distribution of our bedrock horizon marker data (Figure 3-2).

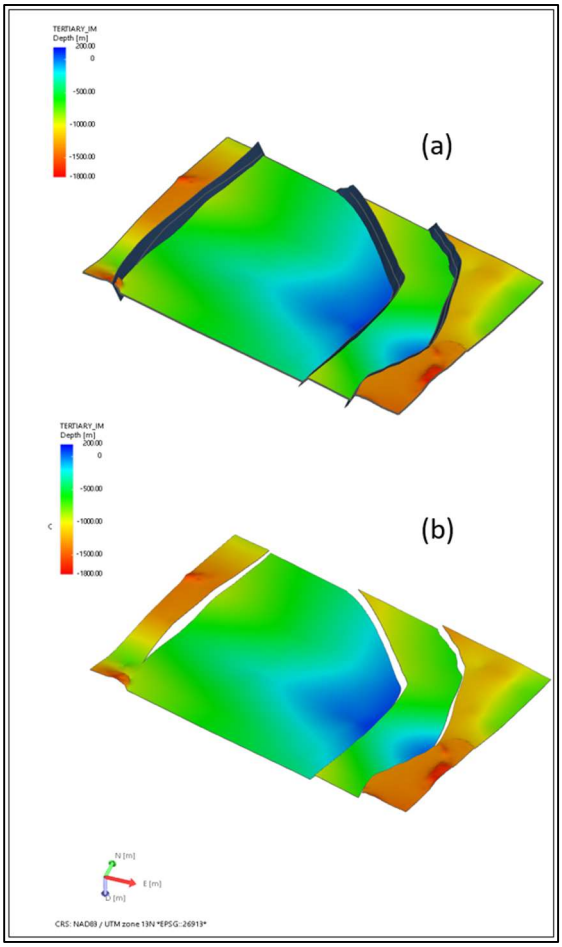

Figure 3-8: The top of bedrock surface created using the 3D Structure workflow with faults (a) and without faults (b). Note the location of depocenters (blue) in the hanging walls of the Eastern and Central Faults, where thick accumulations of alluvial sediment are projected.

3.5 Creating a watertight volume in JewelSuite

A watertight model is a GFM with no gaps in the geologic volumes and all surface elements (e.g., horizons, faults, unconformities) seamlessly stitched together. A watertight model is required for generating 3D meshes, calculating accurate volumetrics, and performing downstream computational analyses. Generating a watertight model for our AoI required inspection and remediation of mismatched horizon-horizon and horizon-fault intersections of the 3D structure created during the surface and fault generation workflows. As a first pass, the intersections were repaired using the Retract, Clear and Extend tools, which resolved the simpler watertight issues. The Diagnostic tool was then executed to identify remaining locations that were not watertight. The non-watertight nodes were repaired manually using the Editing tools and Diagnostic tool iteratively until all intersections were watertight (Figure 3-9). Once complete, the 3D structural model contains two surfaces (Top Alluvium and Top Bedrock) and three faults (Eastern, Central and Western) with all contact nodes watertight (Figure 3-10).

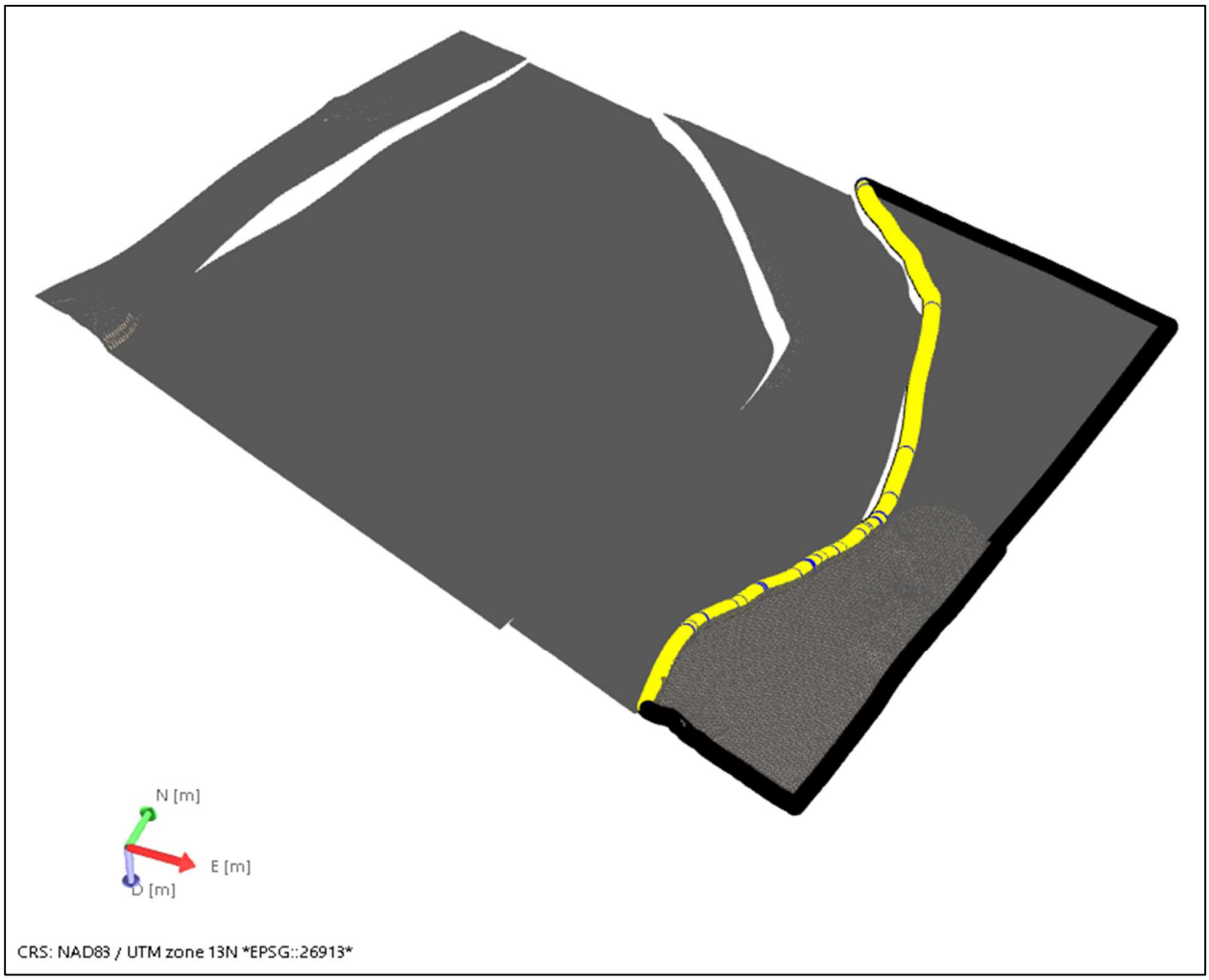

Figure 3-9: Example output from the Diagnostics tool. Black nodes are "free nodes" (i.e., no associated boundaries at model edge). Yellow nodes are watertight. In this example the easternmost block of the top bedrock surface is watertight against the Eastern Fault.

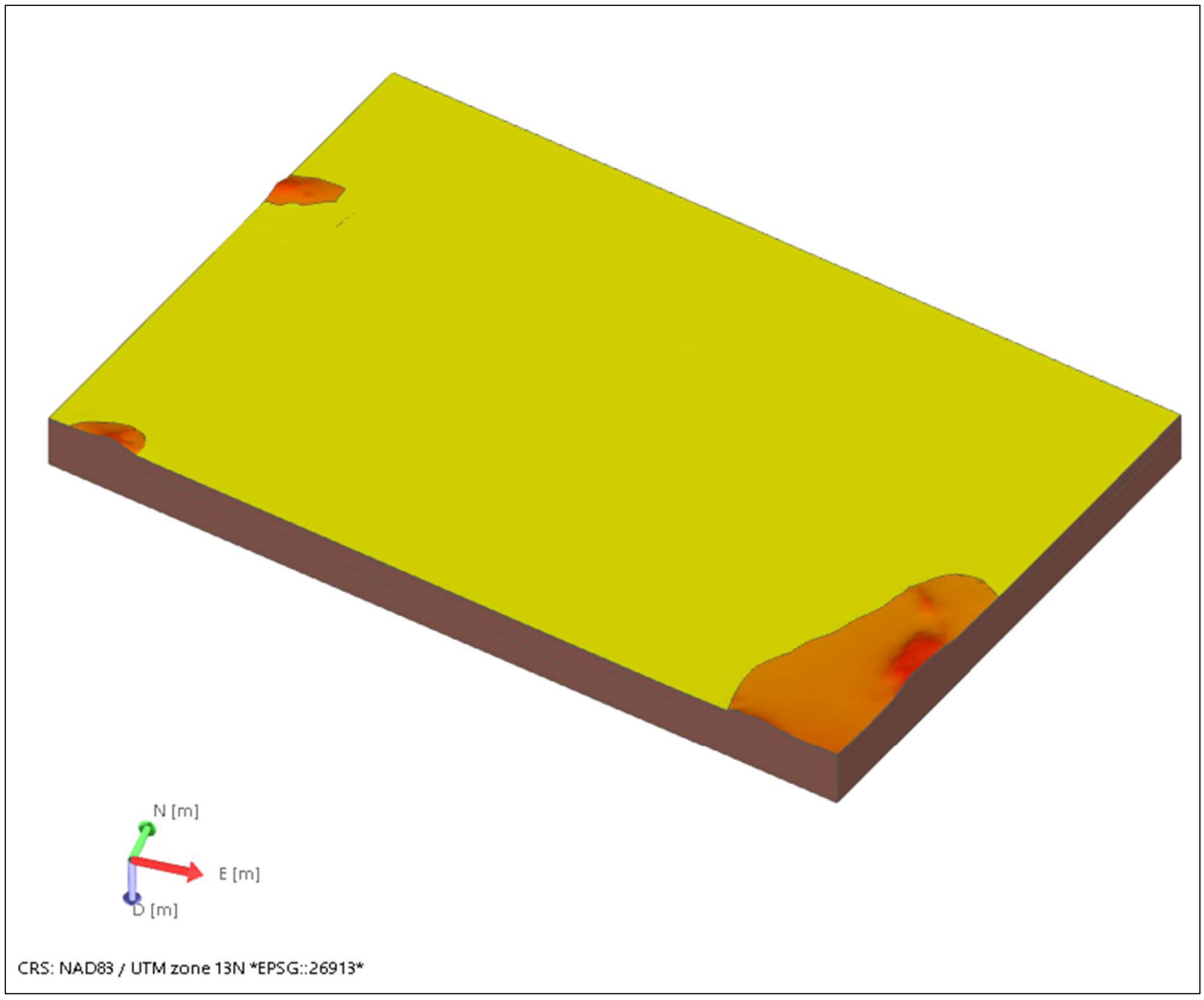

Figure 3-10: The finalized 3D structural model.

3.6 Creating a 3D Grid and a 3D Mesh in JewelSuite™

A 3D grid is generated in volumes bounded by surfaces and/or faults and is characterized by a series of 3D cells with specified horizontal *(i,j)* and vertical *(k)* dimensions. The initial grid created for the basin-scale model was divided into two volumes: alluvial sediments (between top alluvium and top bedrock surfaces) and bedrock (between top bedrock surface and the bottom of the model at 500 m below sea level). The horizontal grid cell dimensions are 200 m x 200 m and a single *k-layer* of variable thickness was assigned to each unit (Figure 3-11). The grid cell size can be customized according to scale, geologic heterogeneity and modeling needs. For example, the number of *k-layers* (or alternatively, *k-layer* thickness) can be defined for each grid volume. Physical properties such as porosity and permeability can be assigned to grid cells, which in turn can be exported for downstream applications.

The 3D Mesh Tool is necessary to generate volume meshes for computational analysis. Execution of this tool is a two-step process: (1) retriangulate the surfaces (surface meshing) to

prepare them for input into the volume meshing step, and (2) generate a tetrahedral volume (volume meshing) for numerical simulations (Baker Hughes, 2020). Downstream purposes and computing power should be considered when selecting the element sizes. We suggest generating a 3D mesh at a coarse resolution first (to make sure the mesh generation is successful) and then generating 3D meshes at finer resolutions in subsequent meshing runs. Figure 3-12 and Figure 3-13 show the fully meshed GFM upon completing the 3D mesh workflow.

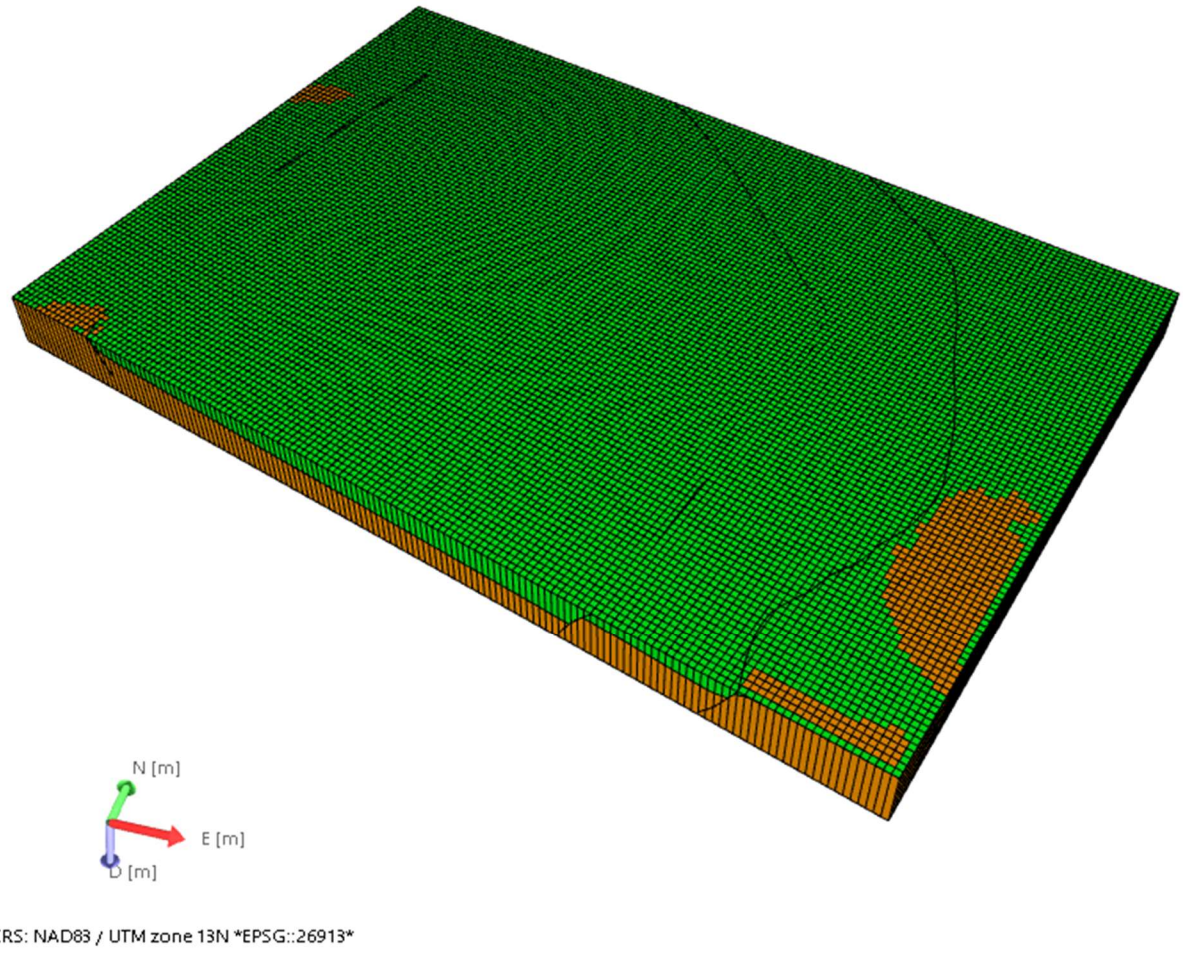

Figure 3-11: Initial results from the 3D Grid workflow, where green cells are alluvium and orange cells are bedrock. Horizontal grid cell dimensions are 200 m x 200 m.

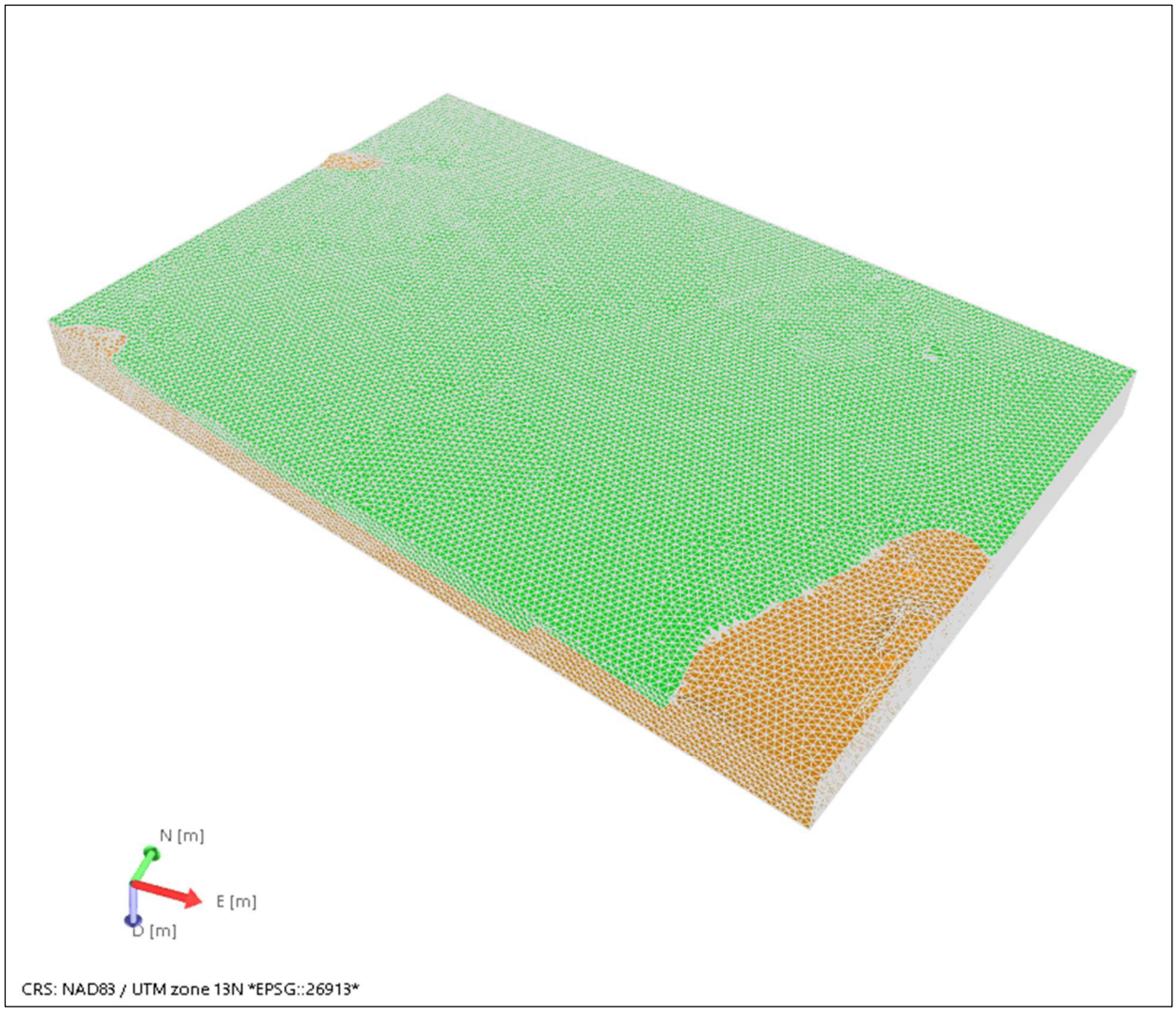

Figure 3-12: Fully meshed GFM after completing the 3D Mesh workflow. Green=alluvium; orange= bedrock.

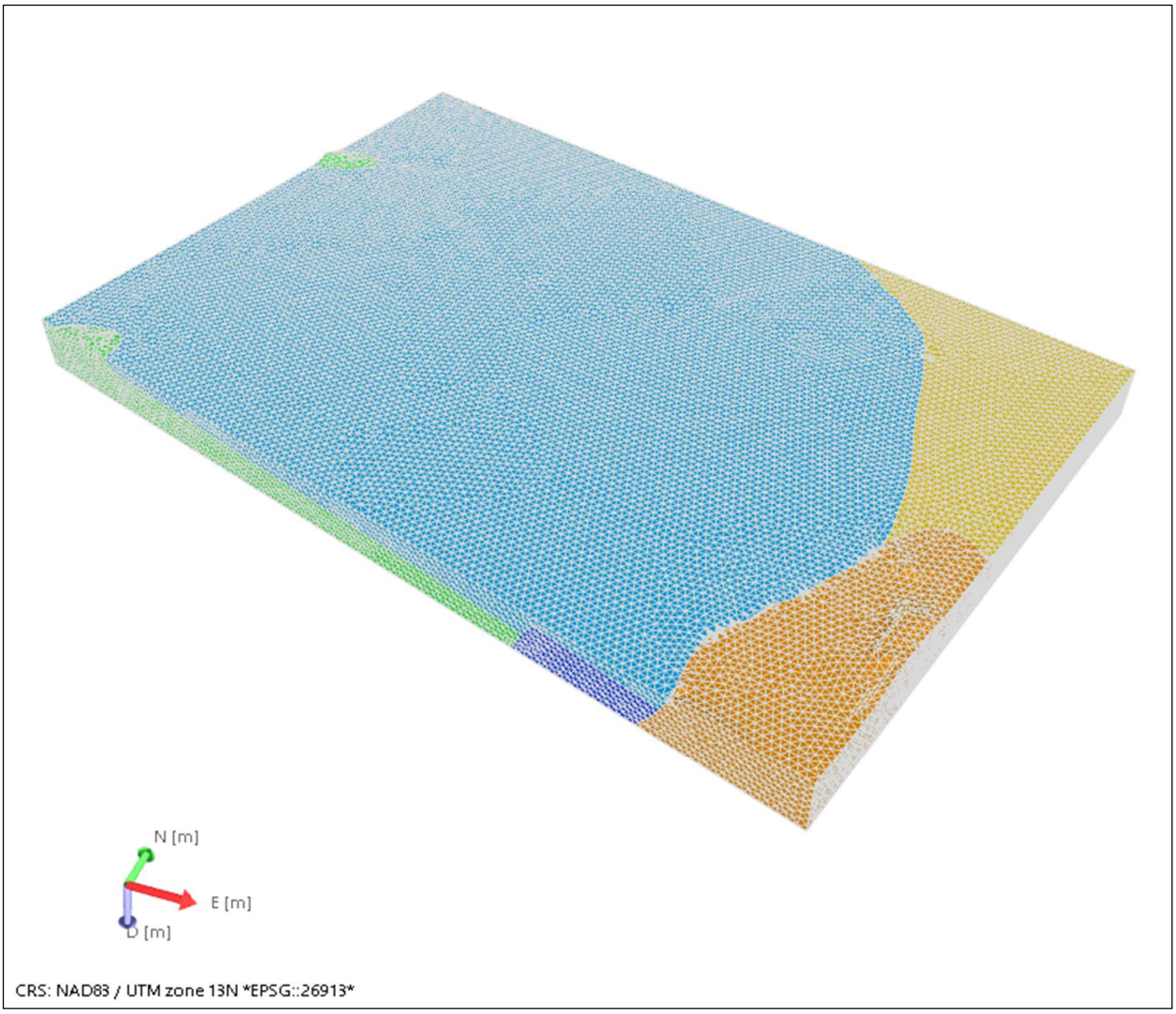

Figure 3-13: Fully meshed GFM after completing the 3D Mesh workflow, color-coded by Compartment ID.

3.7 Creating output files for downstream analysis

To explore the GFM's compatibility with modeling efforts and programs related to repository science, we sampled a sub-volume of the GFM to test file formatting for 3D mesh and grid exports and numerical simulations. The volume is a narrow slice of the GFM aligned perpendicular to the basin axis that includes the Central Fault (Figure 3-14), with horizontal dimensions of 10,000 m x 350 m and a vertical dimension of 1500 m (Figure 3-15). In order to ensure sufficient optimal upscaling during the downstream modeling process, the alluvium was divided into 10 *k-layers* and the bedrock was divided into 5 *k-layers* (Figure 3-15).

Two GFM file outputs are required for downstream modeling: (1) the unit volumes – in order to recreate the entire model volume (including compartment and zone IDs) – and (2) the desired material properties. These outputs require a specific file format to facilitate compatibility with downstream modeling programs.

To export 3D mesh geometry, select the appropriate 3D Mesh Structural Model and export to a GOCAD (.so) file. The .so file contains a header followed by two sections: vertex information and tetrahedral information, defined as 'VRTX' and 'TETRA', respectively (Figure 3-16). Vertices are defined in *x,y,z* format, whereas tetrahedrons are defined as four vertices and then assigned a Compartment ID (1-6) and a Zone ID (1-3)(Figure 3-16). We employed a generic "distance from well" calculation using the Property Calculator to create a file that represents a continuous material property (Figure 3-17). This allowed us to experiment with simple but non-homogeneous property values. To export 3D Mesh properties, right-click the "Distance" property in JewelSuite™ and then select "Create GSLIB Point Set with Coordinates". This creates a *.dat* file with *x,y,z* coordinates along with its corresponding property value (Figure 3-18). Chapter 5 describes how these exported files are incorporated into downstream meshing applications.

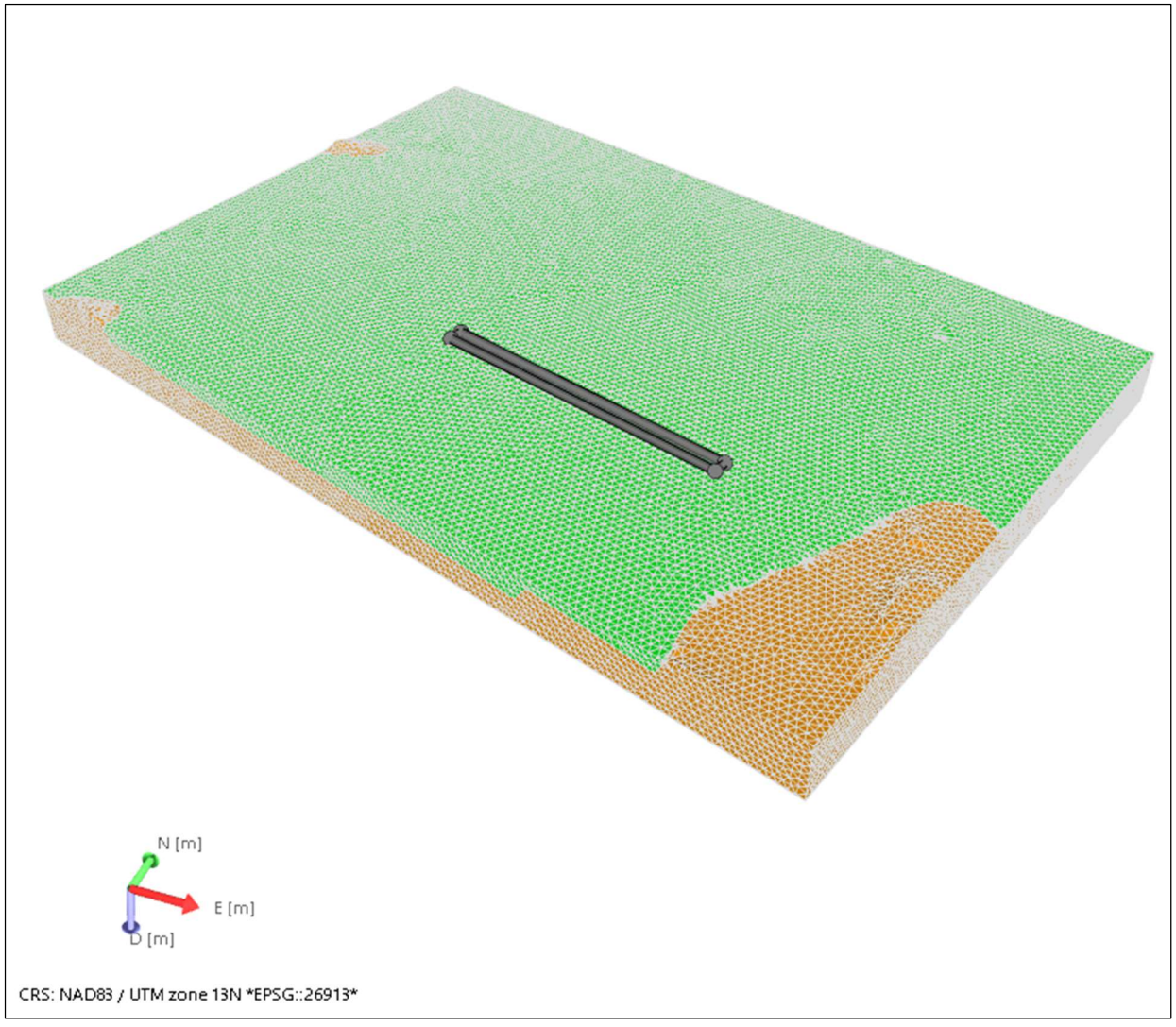

Figure 3-14: Location of sub-volume sampled for export to downstream applications. The sub-volume transects the deepest part of the alluvial basin and the Central Fault.

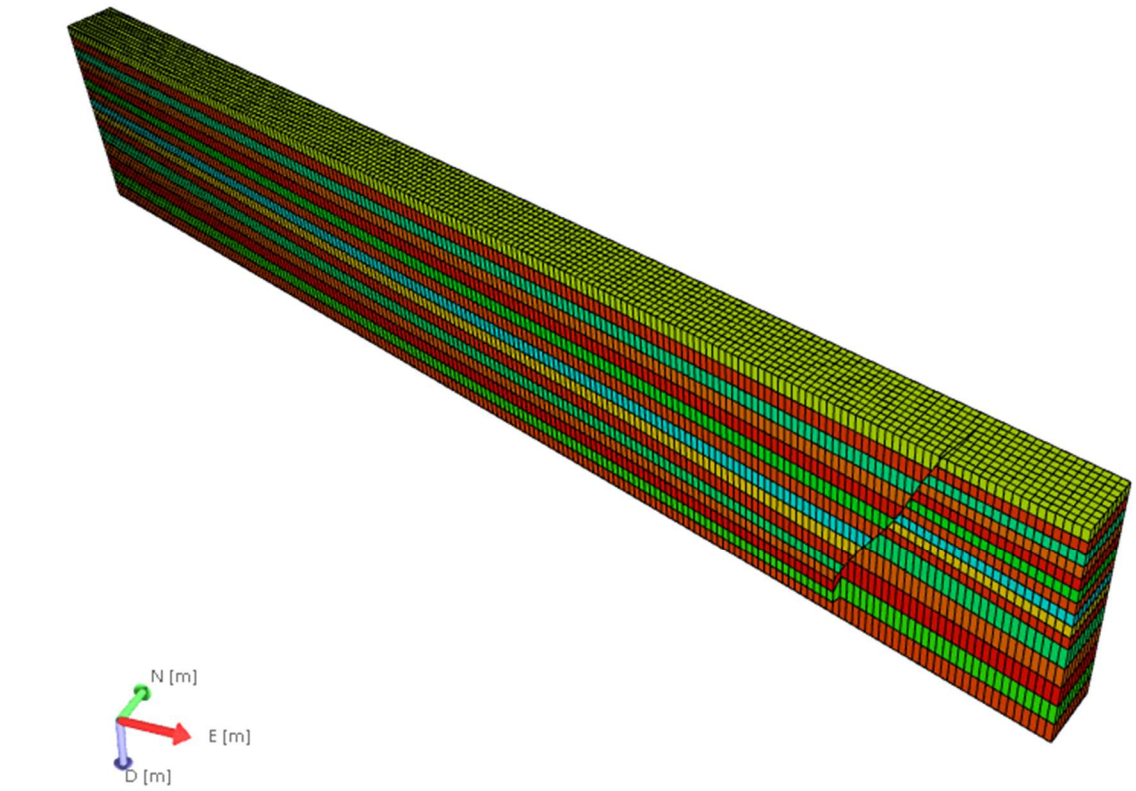

Figure 3-15: Sub-volume of the GFM sampled for downstream modeling tasks. The alluvium is divided into 10 k-layers and the bedrock is represented with 5 k-layers.

```
AXIS_NAME "X" "Y" "Z"
AXIS_UNIT "m" "m" "m"
ZPOSITIVE Depth
END_ORIGINAL_COORDINATE_SYSTEM
TETRA_PROPERTIES CompartmentId ZoneId
TETRA_PROP_LEGAL_RANGES **none** **none** **none** **none**
TETRA_NO_DATA_VALUES -999.25 -999.25
TETRA_PROPERTY_CLASSES CompartmentId ZoneId
TETRA_PROPERTY_KINDS unknown unknown
TETRA_PROPERTY_SUBCLASSES QUANTITY Float QUANTITY Float
TETRA_ESIZES 1 1
TETRA_UNITS unitless unitless
TETRA_PROPERTY_CLASS_HEADER CompartmentId{
low_clip:1
high_clip:6
}
TETRA_PROPERTY_CLASS_HEADER ZoneId{
low_clip:1
high_clip:3
}
TVOLUME
VRTX 1 238700.94799374999 3571406.5230546873 -1322.1241455078125
VRTX 2 238732.34838437499 3571519.7476640623 -1322.2924804687502
VRTX 3 238723.61010312499 3571400.2383867186 -1322.0596923828127
VRTX 4 238755.01049374999 3571513.4629960936 -1322.2176513671877
VRTX 5 247389.98705624999 3568996.8389726561 -1297.5135498046875
VRTX 6 247543.49877499999 3569421.2505937498 -1297.7565917968745
VRTX 7 238843.86791562499 3571833.8719316404 -1322.4482421874998
VRTX 8 248361.14721249999 3569194.4966874998 -1296.1353759765632
VRTX 9 248240.88939999999 3568760.8628984373 -1296.374145507813
VRTX 10 238821.20580624999 3571840.1565996092 -1322.5130615234382
...

TETRA 11559 9740 9721 13186 1 1
TETRA 13186 11526 11552 11564 1 1
TETRA 8838 4274 4273 4057 2 2
TETRA 13427 12686 6330 6323 1 1
TETRA 10144 1904 1894 1903 3 2
TETRA 9214 4957 4698 4697 2 2
TETRA 10149 1895 1850 1894 3 2
TETRA 11516 11521 11515 13186 1 1
TETRA 13795 11521 11515 13192 1 1
TETRA 7403 2630 1296 1289 3 2
...

END
```

Figure 3-16: Exported file format for LaGriT to recreate the GFM geometries and volumes.

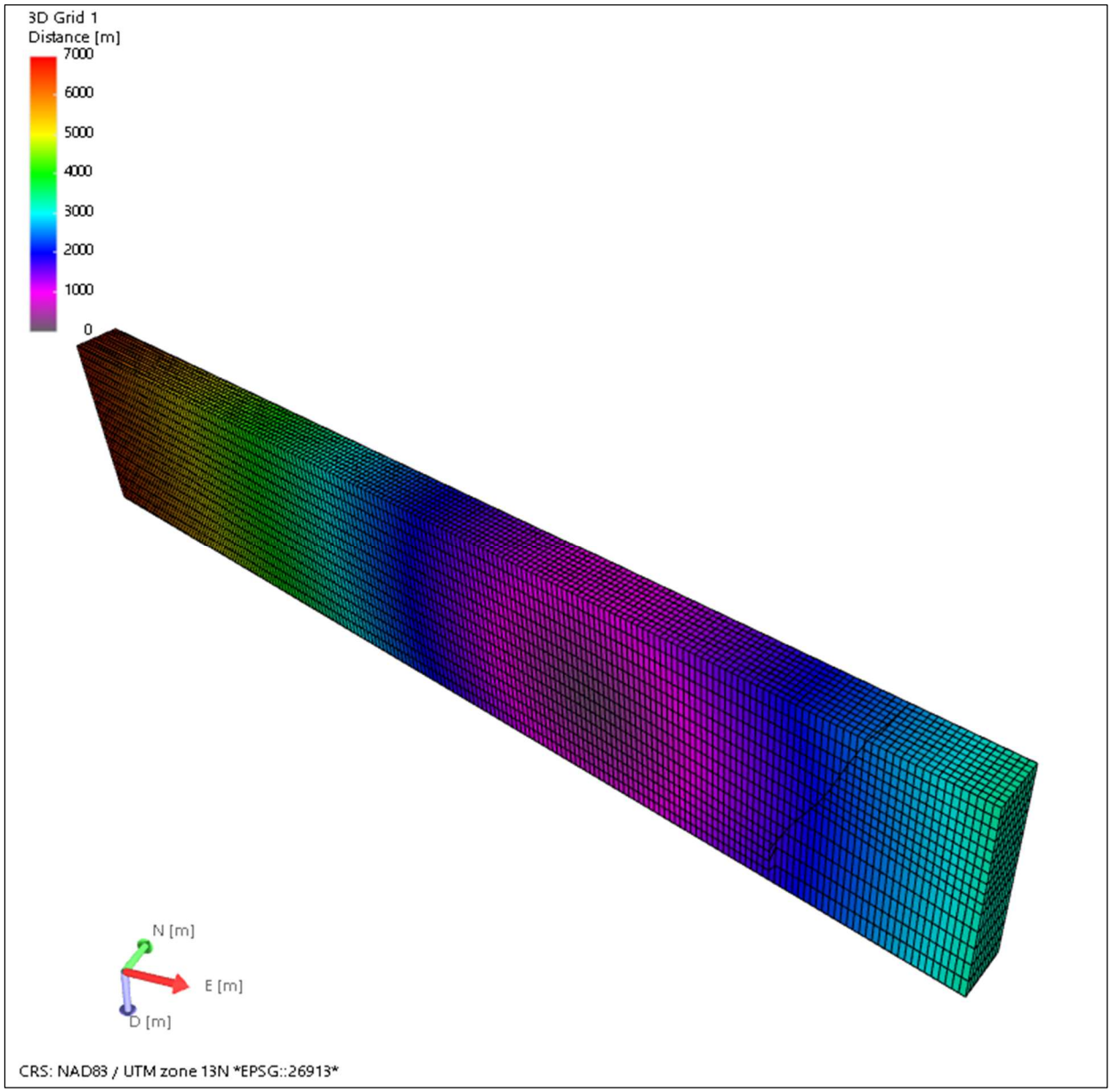

Figure 3-17: Small slice of the GFM used for downstream modeling tasks. To test the proper file format for GFM handoff, a notional well was placed in the center of the slice, and then the JewelSuite™ property calculator was used to perform a "Distance from Well" calculation. This property file was then used to test numerous export formats.

```
3D Grid 1  (9, 198, 15)  Start Depth 1
4
X  Unit m
Y  Unit m
Z  Unit m
Distance  Template Distance  Unit m
238731.719422316 3571423.93279472 -422.930961234996 6719.94291785036
238779.900945972 3571410.57087416 -423.15766431377 6670.28112964709
238828.082468495 3571397.2089556 -423.386984220641 6620.62472790031
238876.263991814 3571383.84703563 -423.611335471305 6570.97299695537
238924.44551334 3571370.48511883 -423.830386832684 6521.32600983119
238972.627036923 3571357.1231984 -424.05162439269 6471.68470731713
239020.808557792 3571343.76128276 -424.271040125397 6422.04877610722
239068.990080886 3571330.39936319 -424.494530143475 6372.41900495078
239117.171603828 3571317.03744389 -424.713680871999 6322.79457833013
239165.35312703 3571303.67552413 -424.930247899752 6273.17582493147
...
```

Figure 3-18: File format for LaGriT in order to import specific material property information.

4 Facies and Property Modeling

4.1 Framework for Geostatistical Modeling

Geostatistical analyses are a powerful tool for capturing the heterogeneity and uncertainty in subsurface geologic formations. They are especially important for modeling alluvial sediments due to the lateral and vertical variability of lithofacies across a typical alluvial basin; these variabilities are important considerations for determining the feasibility of hosting a nuclear waste repository at a desired location. The distribution of lithofacies, in turn, may have a dramatic impact on physical properties such as porosity and permeability. A 3D grid, a volume of interest (VoI) divided into cells of specified dimensions, provides the foundation for geostatistical analyses (Shepherd, 2009a, b). Various properties can be assigned to the grid cells according to input data, property calculations and statistical algorithms.

The 3D grid for our model of basin-fill sediments is defined by its bounding stratigraphic surfaces: the top of alluvium and the top of bedrock. The model geometry is laterally constrained by the three prominent normal faults, which is typical of a structurally-controlled basin (Figure 4-1). The selection of cell size is an important consideration when designing the 3D grid, as valuable information, such as lithologic heterogeneity and thin bands of contrasting permeability, may be lost during upscaling. Ultimately, the cell size depends upon model scale and volume, geologic heterogeneity, and downstream modeling requirements. For the Deming sub-basin we assigned horizontal dimensions of 200 m x 200 m and a vertical dimension of 50 m. The latter corresponds to 27 *k-layers* which are aligned conformable to the top of the alluvium (Figure 4-2). The 3D grid model of the alluvium contains ~430,000 cells; as described in the following sections, these grid cells are subsequently assigned values based on results from facies and physical properties modeling.

Figure 4-1: The 3D Grid model for alluvial sediments in the Deming sub-basin. Grid cells are 200 m x200 m in the horizontal dimension and 50 m in the vertical dimension.

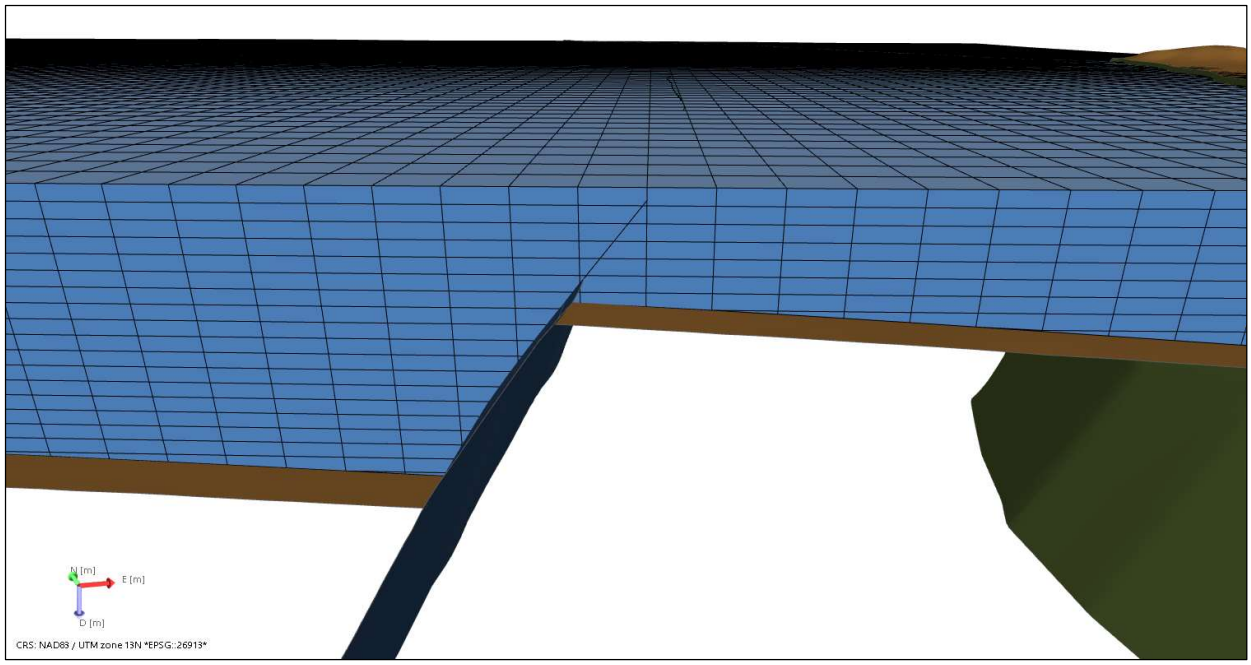

Figure 4-2: Close-up of the 3D grid in the vicinity of the Central Fault. The k-layers are conformable (i.e., parallel) to the top alluvium surface and maintain a constant thickness except where cut by horizons or faults.

4.2 Facies Modeling

We constructed three facies models in order of increasing complexity: an undifferentiated model consisting of a single facies, a horizontally layered model with three facies in stratigraphic succession and an alluvial lithofacies model to match the interpreted cross section in Figure 2-8. The increasing level of complexity reflects more realistic geologic scenarios.

4.2.1 Facies Model 1: Undifferentiated Alluvium

The undifferentiated model is the simplest facies model and consists of a single facies (Gila Group) that was created by inserting a synthetic well (Well #5) in the deepest part of the basin (Figure 4-3). Two files are needed to describe each well: a well trajectory file that describes the well properties and a well log file that describes rock properties of the well, such as facies type, gamma ray and porosity.

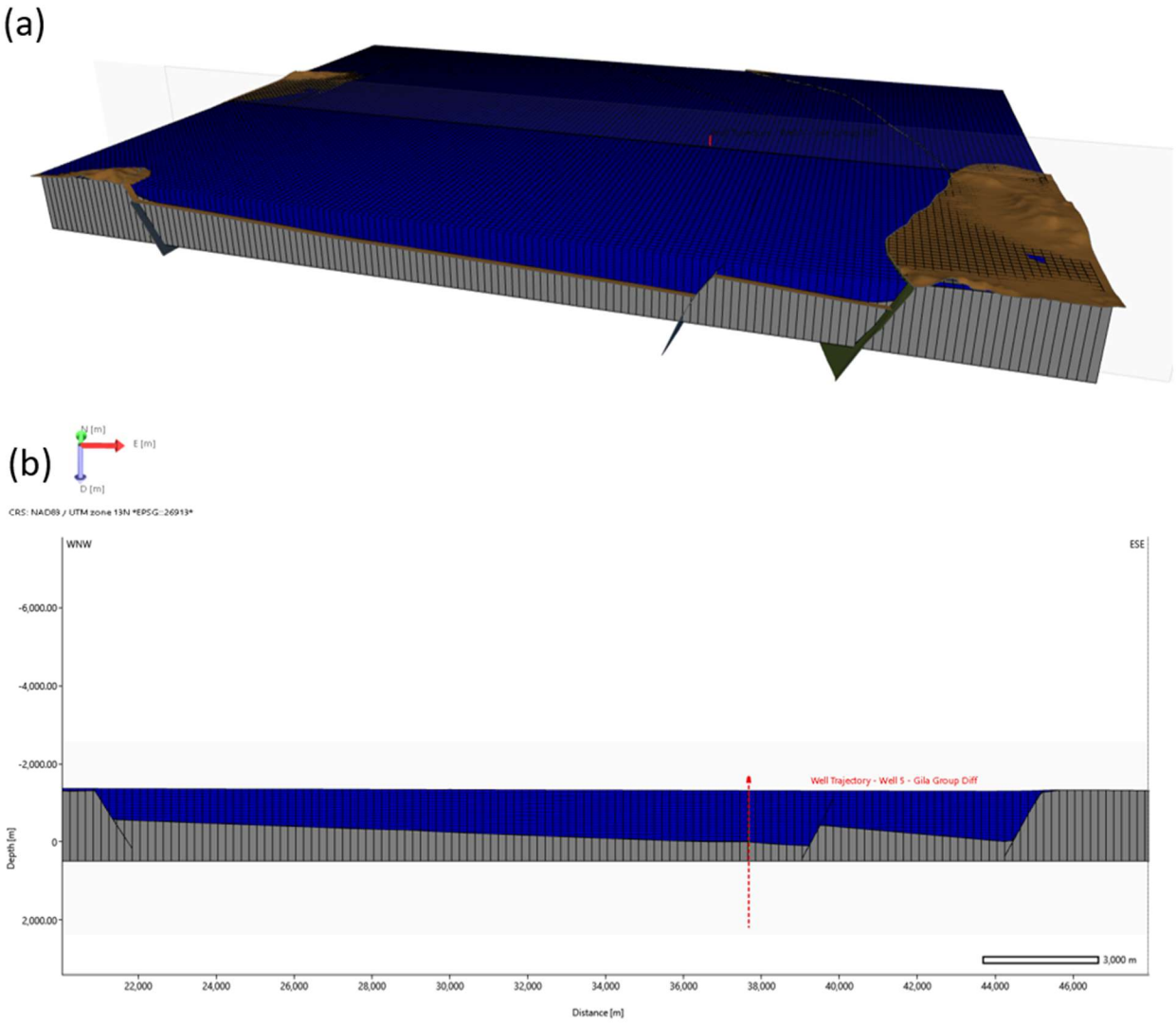

Figure 4-3: Undifferentiated facies model consisting of one lithologic facies, generated from a single synthetic well in the deep part of the basin. (a) 3D perspective, (b) cross-section normal to the basin axis.

4.2.2 Facies Model 2: Layered Alluvium

A three-layer facies model was constructed to match the general subdivision of the Gila Group into Lower, Middle and Upper units (Hawley et al., 2000), a subdivision also adopted by Sweetkind (2017) for modeling the Santa Fe Group in the Rio Grande region to the east of the study area. This was accomplished by inserting one synthetic well (Well #5) with three facies in the well log file and selecting the “Constant” method in the JewelSuite™ “Facies Modeling” workflow. This produces a three-layer model with horizontal boundaries between the facies units (Figure 4-4).

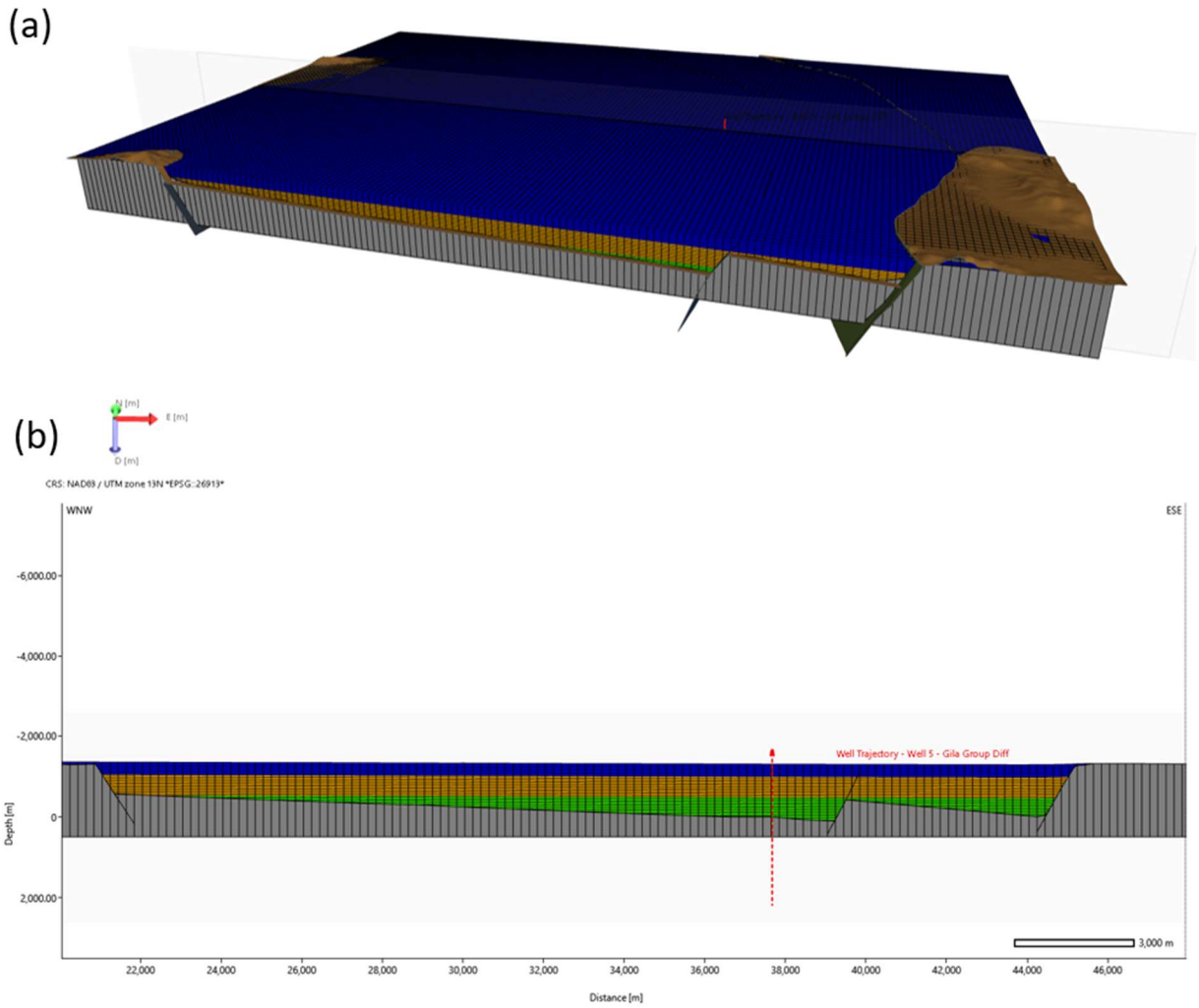

Figure 4-4: Layered facies model consisting of Lower Gila (green), Middle Gila (orange) and Upper Gila (blue) units, generated from a single synthetic well in the deep part of the basin. (a) 3D perspective, (b) cross-section normal to the basin axis.

4.2.3 Facies Model 3: Distributed Alluvial Lithofacies

We also created a GFM with a more realistic distribution of alluvial lithofacies to match the interpreted cross-section in Figure 2-8. Our goal was to explore methods in JewelSuite™ to approximate the facies distribution as depicted in the 2D cross sectional interpretation. The cross-section, aligned perpendicular to the basin axis, integrates information from geologic maps, well data, tectonic history, concepts of depositional environments and paleoclimate. The seven lithofacies exhibit a complex distribution, with lateral facies changes, variable thicknesses and limited areal extents. In a vertical well profile, a specific lithofacies could be repeated or absent depending upon location within the basin.

The cross section was sampled with 18 synthetic vertical wells (Figure 4-5). Elevations for all facies tops for each synthetic well were digitally extracted from the cross section and then entered in well log files for JewelSuite™ import. The facies property was upscaled in each well and assigned values to the grid cells intersected by the well trajectory (Figure 4-5a). The upscaled facies profiles for the 18 wells (Figure 4-5b) serve as constraints for the facies modeling algorithm.

We chose the Truncated Gaussian Simulation (TGS) method for facies modeling. TGS is a variogram-based, stochastic modeling method used to create multiple iterations to explore spatial uncertainty. This modeling method is ideally suited for analyzing information-rich but sparsely distributed sampling points such as well data. We tested different variogram ranges while keeping other parameters constant. Variogram range is defined as the distance between cells above which there is no correlation in the property of interest. The range has an ellipsoidal geometry, with major and minor horizontal axes and a vertical axis. For our application, the property of interest is the alluvial facies.

Running the TGS model generated a 3D grid with facies assigned to each cell (Figure 4-6). Although we focused on the facies distribution model along the 2D cross section, the TGS model can be applied across a volume as large as the Deming sub-basin. Note that uncertainty in facies modeling increases with distance from the cross section line as defined by the wells, with Lower Gila exposed on the surface (northeast and northwest corners) and the youngest Mimbres alluvial fan sediments found at depth in the vertical face marking the SW boundary of the model.

Results of the facies modeling for constant horizontal variogram ranges (5000 m x 5000 m) and vertical variogram ranges from 25 m to 1000 m are shown in Figure 4-7. The vertical range of 100 m yielded the best results; the Gila alluvial fans are portrayed correctly in the hanging walls of the normal faults, the Lower and Middle Gila are in appropriate stratigraphic positions and exhibiting tabular geometries, and a thin layer of Mimbres alluvium covers the central and western basin above the lacustrine sediments. A vertical range of 50 m or less adds noise without improving the results, likely due to cell size limitations in the vertical dimension. At vertical ranges of 250 m and above the older alluvium appears in the central basin above the Upper Gila and the unit boundaries become wavy (non-planar). Model results for a constant vertical variogram range and variable horizontal ranges are presented in Figure 4-8. Note that horizontal ranges of 1250 m and 2500 m do not adequately interpolate the facies between the wells.

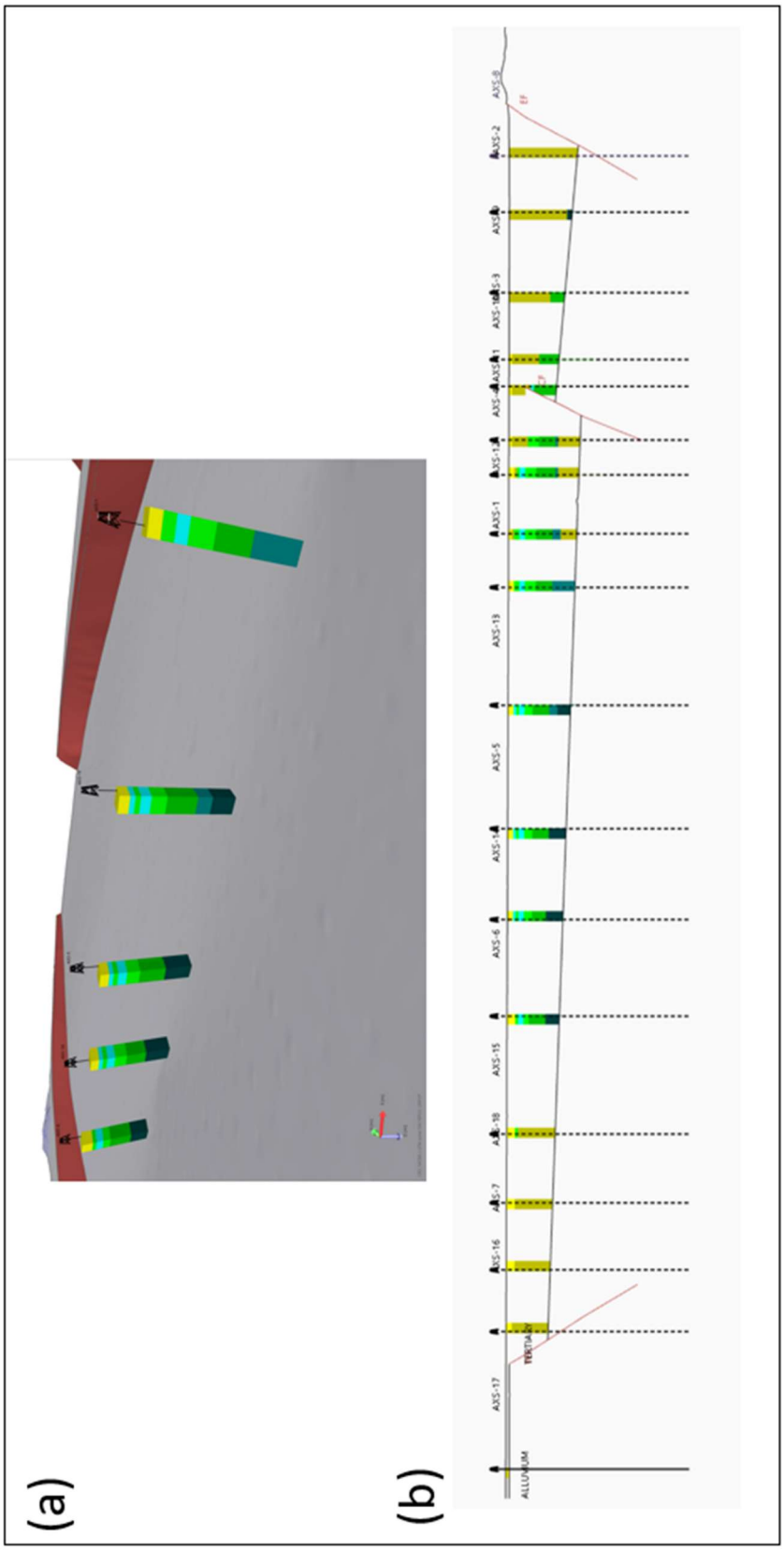

Figure 4-5: (a) Close-up perspective of upscaled facies for synthetic wells in the center of the basin; (b) Profile of the 18 synthetic vertical wells with upscaled facies used to model alluvial lithofacies.

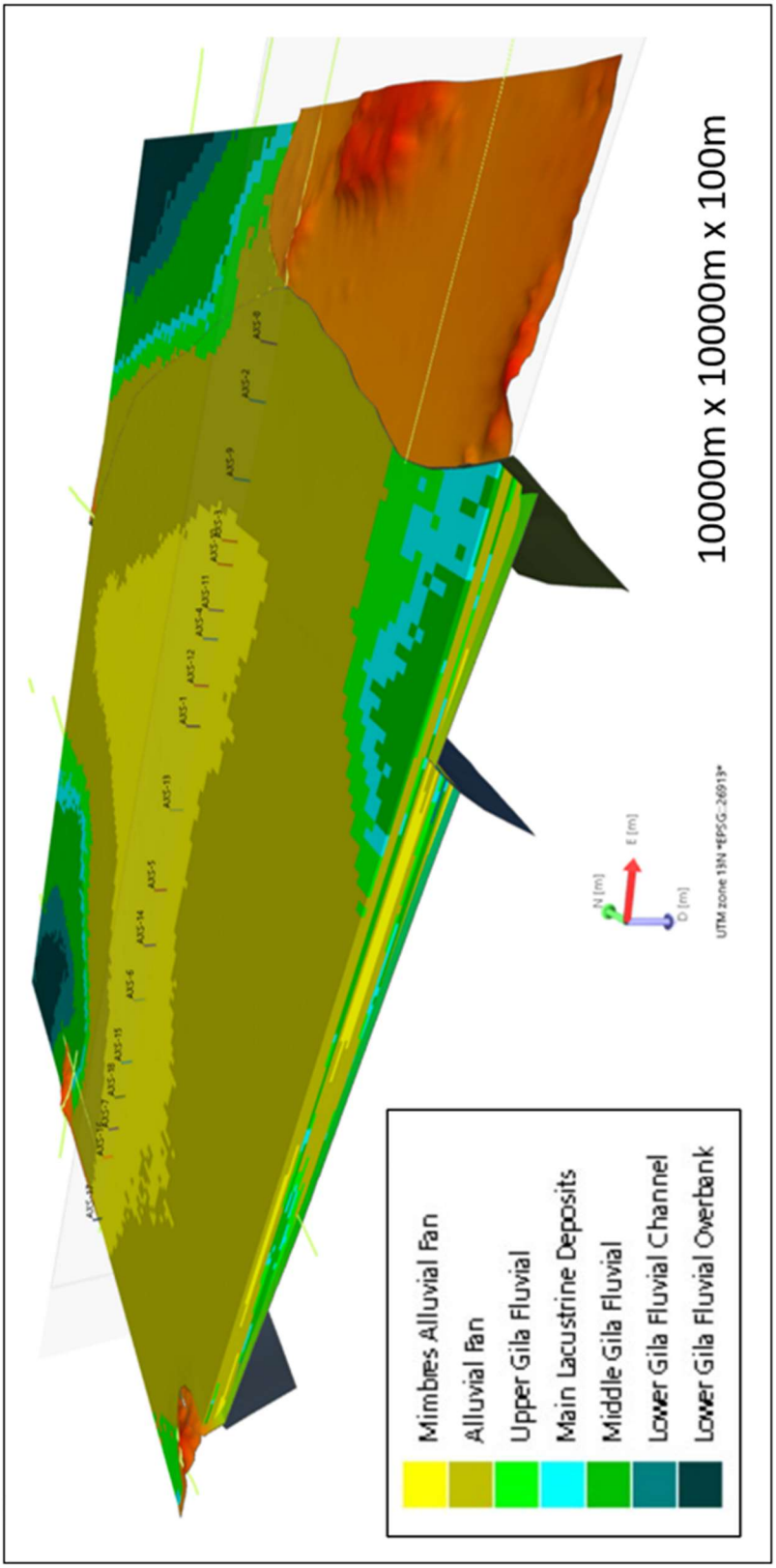

Figure 4-6: 3D gridded results of TGS facies modeling for variogram ranges of 10,000 m (major horizontal axis), 10,000 m (minor horizontal axis) and 100 m (vertical axis). Note the alignment of vertical wells defines the cross-section line in Figure 4-7 and Figure 4-8.

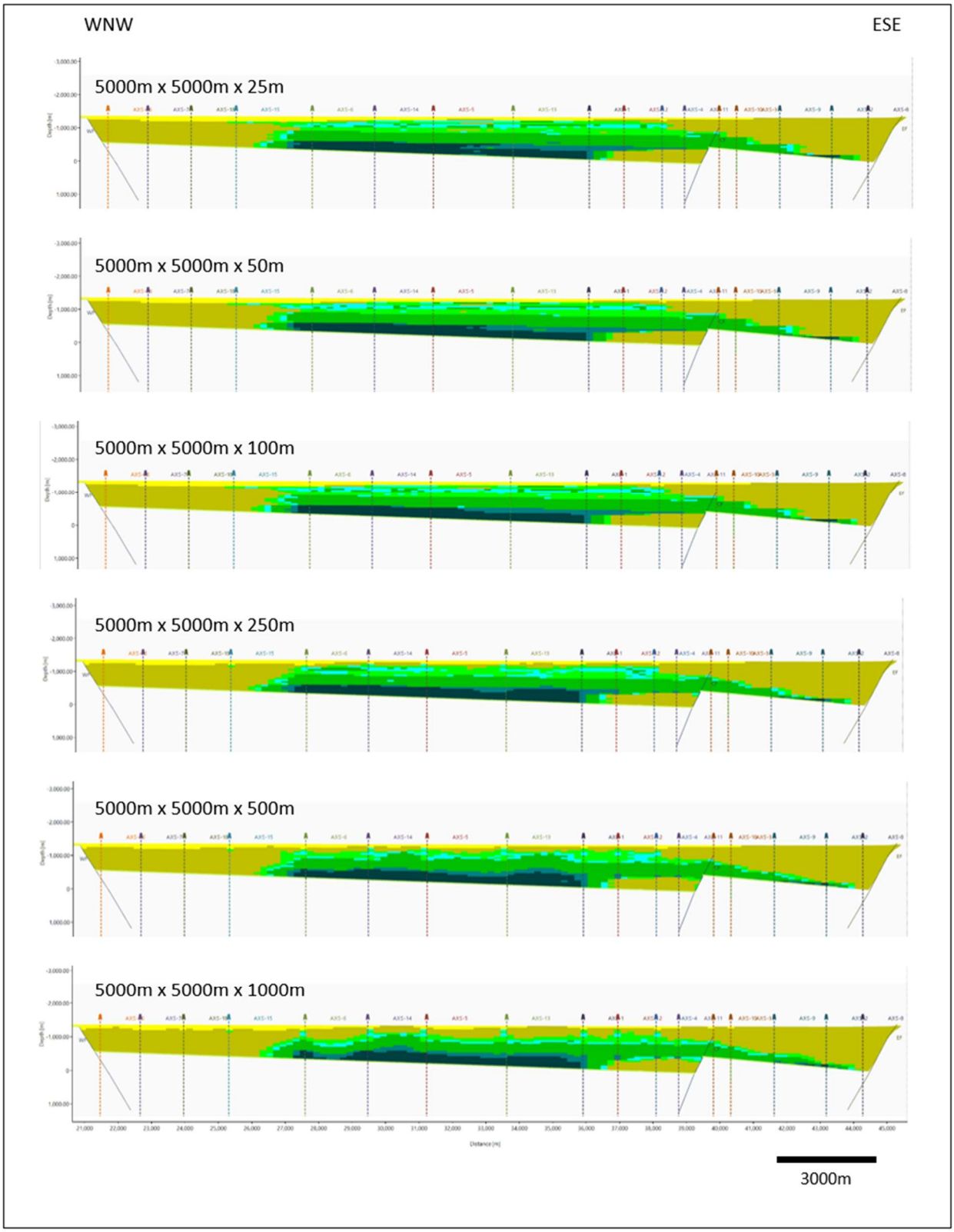

Figure 4-7: Results of TGS facies modeling for the 2D cross section perpendicular to the basin axis (refer to Figure 4-6 for cross section location and facies legend). The horizontal variogram ranges area held constant (5000 m) while the vertical variogram ranges are varied from 25 m to 1000 m.

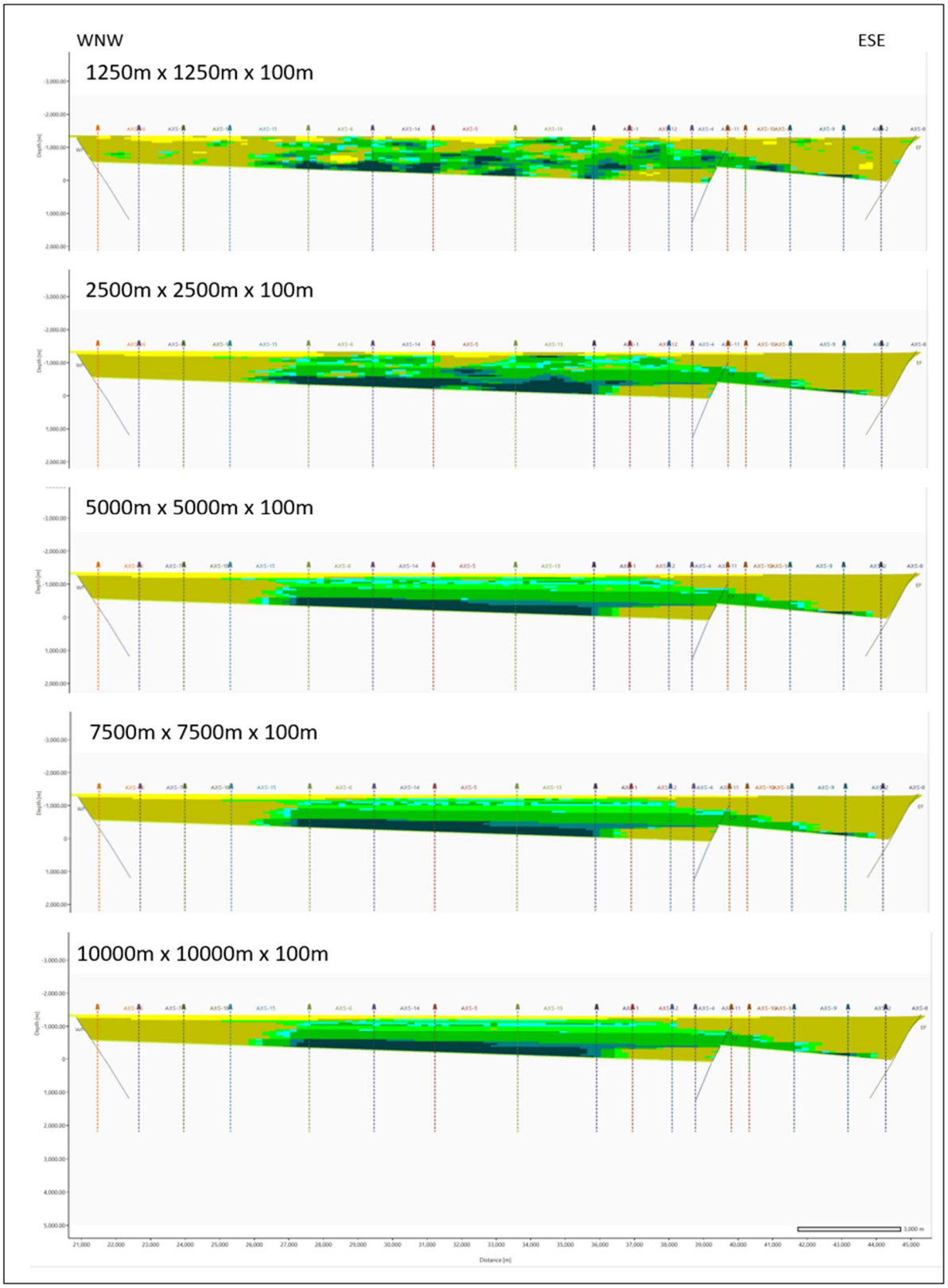

Figure 4-8: Results of TGS facies modeling for the 2D cross section perpendicular to the basin axis (refer to Figure 4-6 for cross section location and facies legend). The vertical range is fixed at 100 m and the horizontal ranges vary from 1250 m to 10000 m.

4.3 Porosity and Permeability Modeling

Porosity and permeability values for alluvial lithofacies in the Mimbres Basin are not readily available in the published literature. Therefore, we integrated the limited hydrologic property values measured in our study area with measurements of porosity and permeability reported from other alluvial basins in the Basin and Range province (Hanson et al., 1994; Anderson, 1995; Thomas et al., 1989; Harrill and Preissler, 1994; Hawley et al., 2000; Brooks, 2017; Mariner et al., 2018; Sevougian et al., 2019). Representative values used in the porosity and permeability models may be found in Table 4-1 and Table 4-2, respectively.

Two sets of porosity models were developed and executed: one set using the undifferentiated facies grid and a second set using the three-layer grid. We used one well in the center of the basin (Well #5) to assign porosity values as a function of depth and then upscaled the property to the appropriate grid. For the undifferentiated models, we assigned a mean porosity of 25%. For the layered facies models, we used porosities of 40%, 25% and 10% for the Upper, Middle and Lower units, respectively (Table 4-1), since porosity is expected to decrease with depth due to compaction and cementation. Lower and upper truncations for all porosity models were set at 1% and 70%, respectively.

We selected Sequential Gaussian Simulation (SGS) as the appropriate geostatistical method for modeling reservoir properties such as porosity and permeability (Shepherd, 2009a). After experimenting with SGS variogram input parameters, we chose a vertical range of 100 m, which consistently yielded realistic geologic interpretations. Holding the minor horizontal range constant at 1500 m, we then varied the major range from 1500 m to 7500 m to evaluate the impact of horizontal anisotropy on the modeled porosity distribution. The major horizontal range axis is oriented at an azimuth of 15° in accordance with flow parallel to the basin axis. Results of porosity modeling for the Deming sub-basin alluvium are presented in Figure 4-9 through Figure 4-11. Example histograms of porosity distribution in the model grid cells are found in Figure 4-12.

The simplest case to consider is the undifferentiated, horizontally isotropic case (Figure 4-9a, b). Note that high and low values of porosity appear as thin lenticular bodies distributed randomly in the cross section (Figure 4-9b). This is a geologically reasonable depiction of the geometry of stratigraphically controlled physical properties but does not account for the expected decrease in porosity as a function of depth. Similarly, the patches of high and low porosity in map view are appropriate in their dimensions, i.e. at the sub-lithofacies scale (hundreds of meters), but do not reflect the anisotropy expected as a result of depositional processes (Figure 4-9a). The layered anisotropic case provides a stepwise decrease in porosity with increasing depth from the Upper, Middle to Lower Gila units (Figure 4-9c). Overlapping porosities among the three units versus the single facies case is reflected in different histogram shapes and maxima for porosity distribution (Figure 4-12). Horizontal anisotropy results in linear streaks of high porosity in the Upper Gila that may reflect depositional current flow parallel to the basin axis (Figure 4-9d).

Table 4-1: Porosity Modeling Parameters

		Porosity (fraction)				Major Azimuth	Major Dip	Major Range	Minor Range	Vertical Range
Model #	Facies Unit	Mean	Stan Dev	Min Trunc	Max Trunc	(degrees)	(degrees)	meters	meters	meters
POR-UN-V1	All Gila	0.25	0.1	0.01	0.7	15.5	0	1500	1500	100
POR-UN-V2	All Gila	0.25	0.1	0.01	0.7	15.5	0	3000	1500	100
POR-UN-V3	All Gila	0.25	0.1	0.01	0.7	15.5	0	4500	1500	100
POR-UN-V4	All Gila	0.25	0.1	0.01	0.7	15.5	0	7500	1500	100
POR-3L-V1	Upper Gila	0.4	0.1	0.01	0.7	15.5	0	1500	1500	100
	Middle Gila	0.25	0.063	0.01	0.7	15.5	0	1500	1500	100
	Lower Gila	0.1	0.025	0.01	0.7	15.5	0	1500	1500	100
POR-3L-V2	Upper Gila	0.4	0.1	0.01	0.7	15.5	0	3000	1500	100
	Middle Gila	0.25	0.063	0.01	0.7	15.5	0	3000	1500	100
	Lower Gila	0.1	0.025	0.01	0.7	15.5	0	3000	1500	100
POR-3L-V3	Upper Gila	0.4	0.1	0.01	0.7	15.5	0	4500	1500	100
	Middle Gila	0.25	0.063	0.01	0.7	15.5	0	4500	1500	100
	Lower Gila	0.1	0.025	0.01	0.7	15.5	0	4500	1500	100
POR-3L-V4	Upper Gila	0.4	0.1	0.01	0.7	15.5	0	7500	1500	100
	Middle Gila	0.25	0.063	0.01	0.7	15.5	0	7500	1500	100
	Lower Gila	0.1	0.025	0.01	0.7	15.5	0	7500	1500	100

Table 4-2: Permeability Modeling Parameters

		Perm (m^2)	Perm log(mD)				Major Azimuth	Major Dip	Major Range	Minor Range	Vertical Range
Model #	Facies Unit	Mean	Mean	Stan Dev	Min Trunc	Max Trunc	(degrees)	(degrees)	meters	meters	meters
PERM-UN-V1	All Gila	$1x10^{-12}$	3.006	0.301	1	4	15.5	0	1500	1500	100
PERM-UN-V2	All Gila	$1x10^{-12}$	3.006	0.301	1	4	15.5	0	3000	1500	100
PERM-UN-V3	All Gila	$1x10^{-12}$	3.006	0.301	1	4	15.5	0	4500	1500	100
PERM-UN-V4	All Gila	$1x10^{-12}$	3.006	0.301	1	4	15.5	0	7500	1500	100
PERM-3L-V1	Upper Gila	$2.3x10^{-12}$	3.367	0.337	0	5	15.5	0	1500	1500	100
	Middle Gila	$1.20x10^{-12}$	2.673	0.267	0	5	15.5	0	1500	1500	100
	Lower Gila	$9.4x10^{-14}$	1.979	0.198	0	5	15.5	0	1500	1500	100
PERM-3L-V2	Upper Gila	$2.3x10^{-12}$	3.367	0.337	0	5	15.5	0	3000	1500	100
	Middle Gila	$1.20x10^{-12}$	2.673	0.267	0	5	15.5	0	3000	1500	100
	Lower Gila	$9.4x10^{-14}$	1.979	0.198	0	5	15.5	0	3000	1500	100
PERM-3L-V3	Upper Gila	$2.3x10^{-12}$	3.367	0.337	0	5	15.5	0	4500	1500	100
	Middle Gila	$1.20x10^{-12}$	2.673	0.267	0	5	15.5	0	4500	1500	100
	Lower Gila	$9.4x10^{-14}$	1.979	0.198	0	5	15.5	0	4500	1500	100
PERM-3L-V4	Upper Gila	$2.3x10^{-12}$	3.367	0.337	0	5	15.5	0	7500	1500	100
	Middle Gila	$1.20x10^{-12}$	2.673	0.267	0	5	15.5	0	7500	1500	100
	Lower Gila	$9.4x10^{-14}$	1.979	0.198	0	5	15.5	0	7500	1500	100

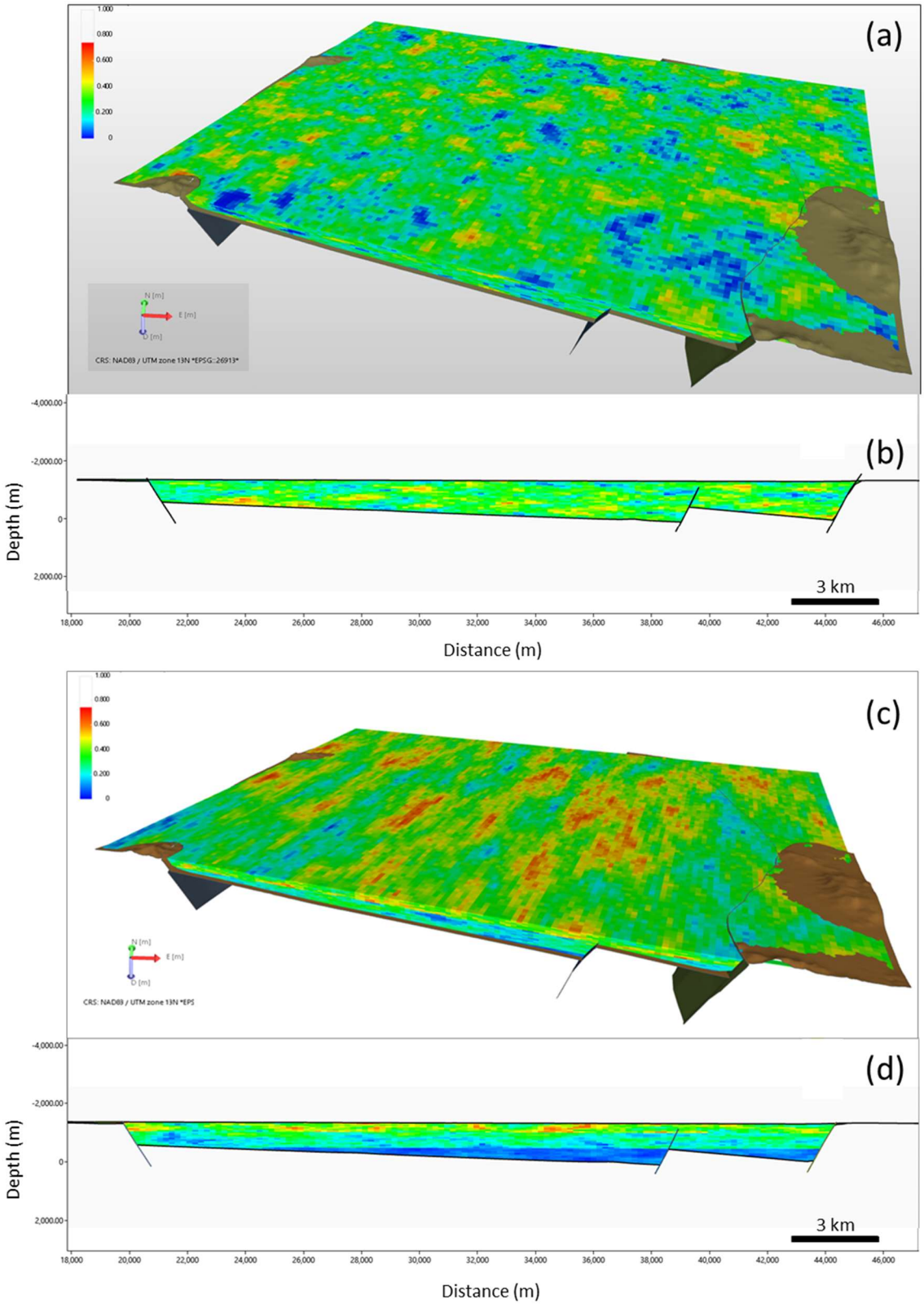

Figure 4-9: Results of porosity modeling in 3D perspectives and basin-normal cross sections for single facies, isotropic (POR-UN-V1; a, b) and for layered anisotropic (POR-3L-V3; c, d) cases.

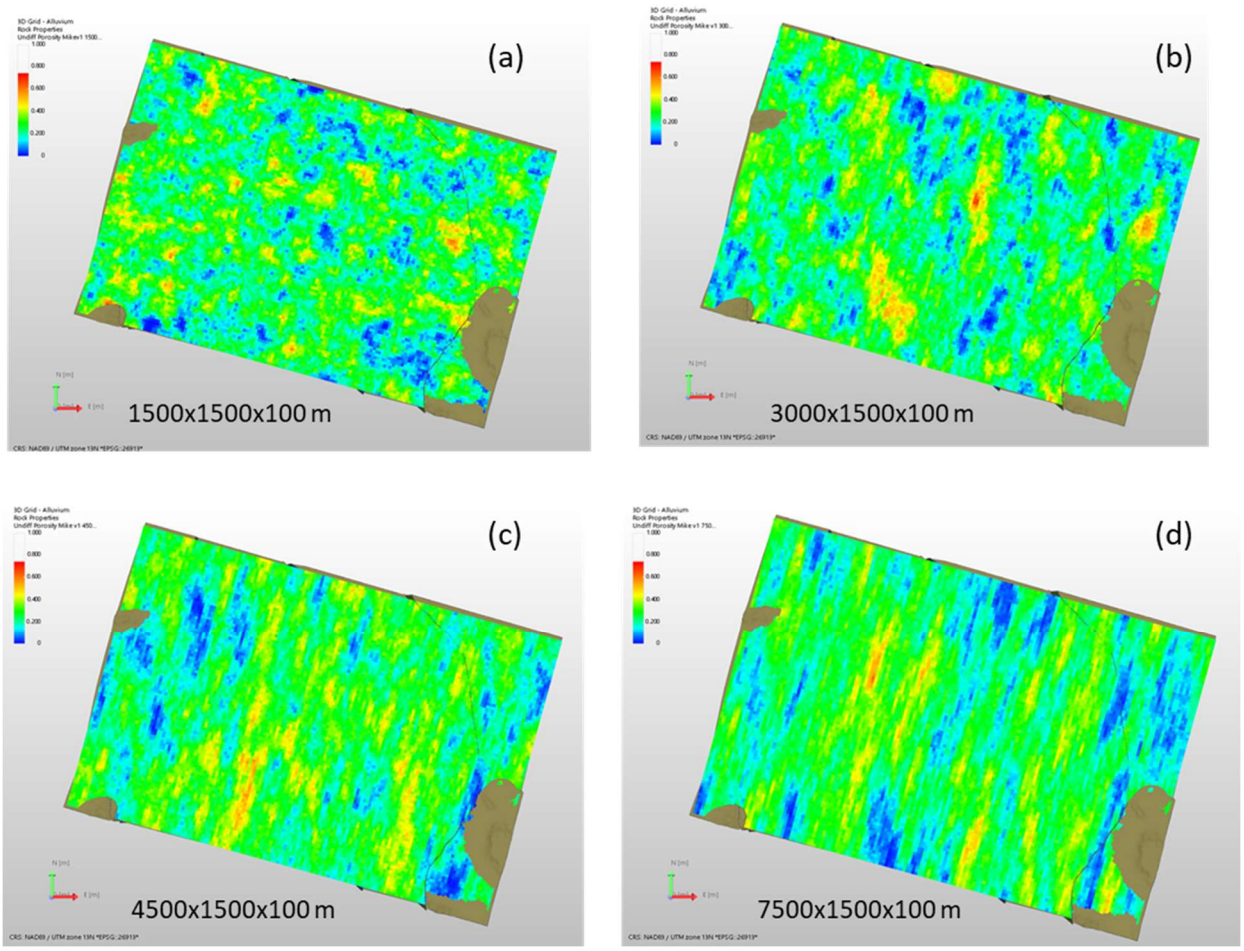

Figure 4-10: Results of porosity modeling for single facies (undifferentiated alluvium) as seen in map view, i.e., top grid layer (k=1): (a) Model POR-UN-V1; (b) Model POR-UN-V2; (c) Model POR-UN-V3; (d) Model POR-UN-V4. Variogram ranges (major horizontal x minor horizontal x vertical). Axis of the major horizontal range is 015° azimuth.

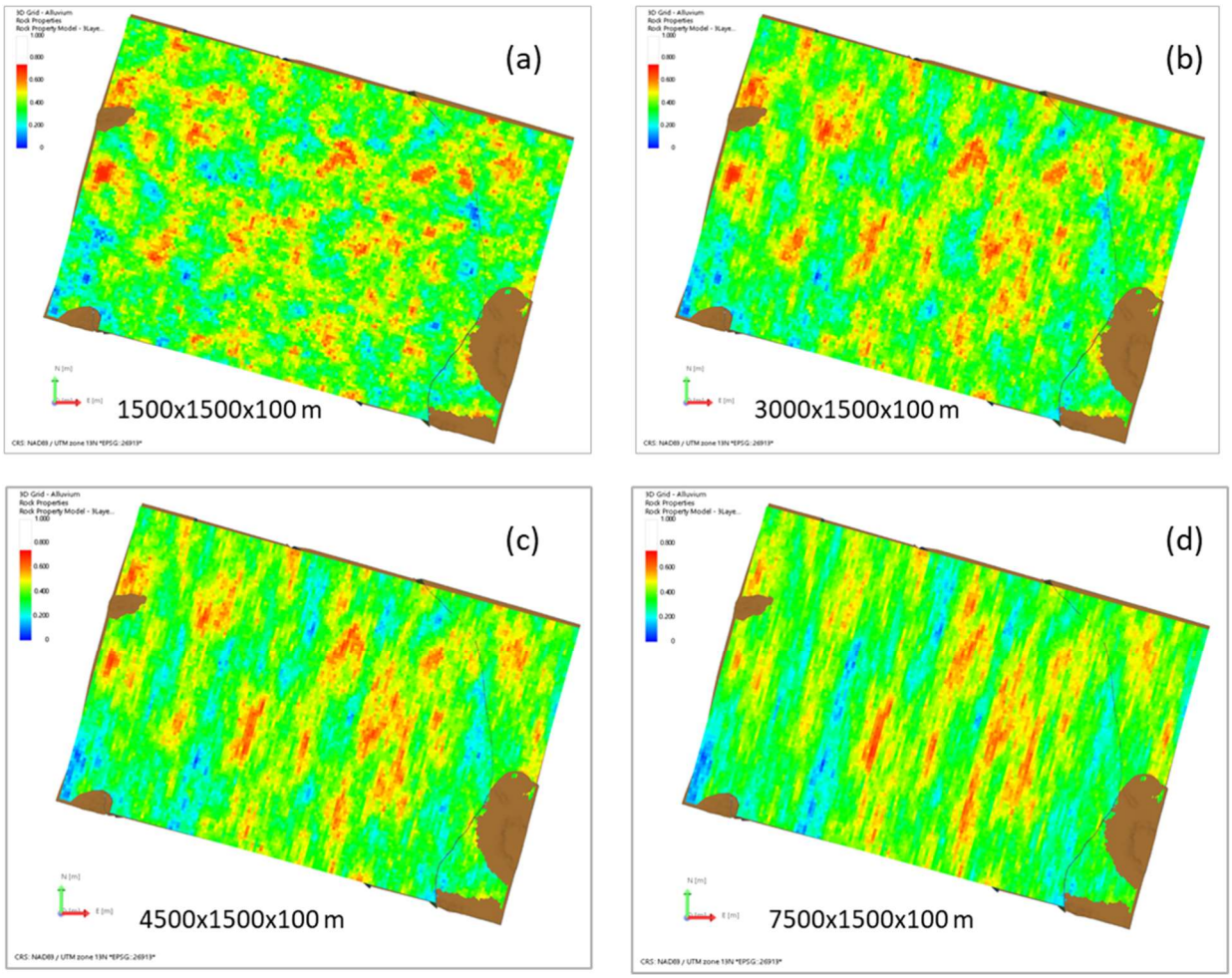

Figure 4-11: Results of porosity modeling for three-layer facies (differentiated alluvium) as seen in map view, i.e., top grid layer (k=1): (a) Model POR-3L-V1; (b) Model POR-3L-V2; (c) Model POR-3L-V3; (d) Model POR-3L-V4. Variogram ranges (major horizontal x minor horizontal x vertical). Axis of the major range is 015° azimuth.

A similar suite of SGS models were generated to model permeability distributions in the alluvium. However, JewelSuite™ would not accept permeability units in m^2, and therefore we resorted to log (10) millidarcies as the unit for calculation and visualization. Permeability in sedimentary rocks typically follows a lognormal distribution (Fetter, 1999; Shepherd, 2009c). For undifferentiated alluvium we used a mean permeability of $1x10^{-12}$ m^2 as reported in Gross et al. (2019). For the three-layer facies models we assigned the Brooks (2017) permeability values for "upper basin fill" and "lower basin fill" to the Upper Gila and Lower Gila units, respectively, and used the log average for the Middle Gila (Table 4-2). Results of the permeability modeling for the Deming sub-basin are presented in Figure 1-1 through Figure 4-15. Histograms of permeability distribution for the three-layer model PERM-3L-V3 are shown as an entire unit and for each layered facies in Figure 4-16. We selected a different color scheme for permeability where dark blue represents high permeability and dark brown low permeability. Model results share many similarities with the porosity models. One key observation to note is the horizontal continuity of high-permeability zones, especially with increasing anisotropy (Figure 1-1 and Figure 1-1). This suggests there may be pathways of high permeability (i.e., "permeability corridors") in the upper portion of the basin-fill sediments.

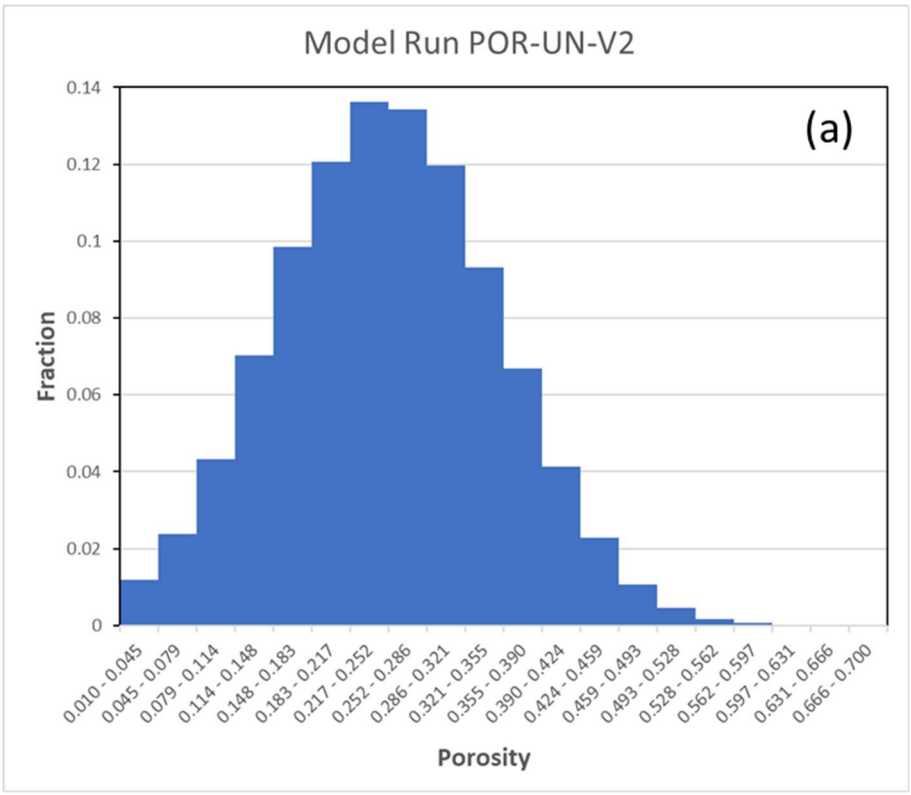

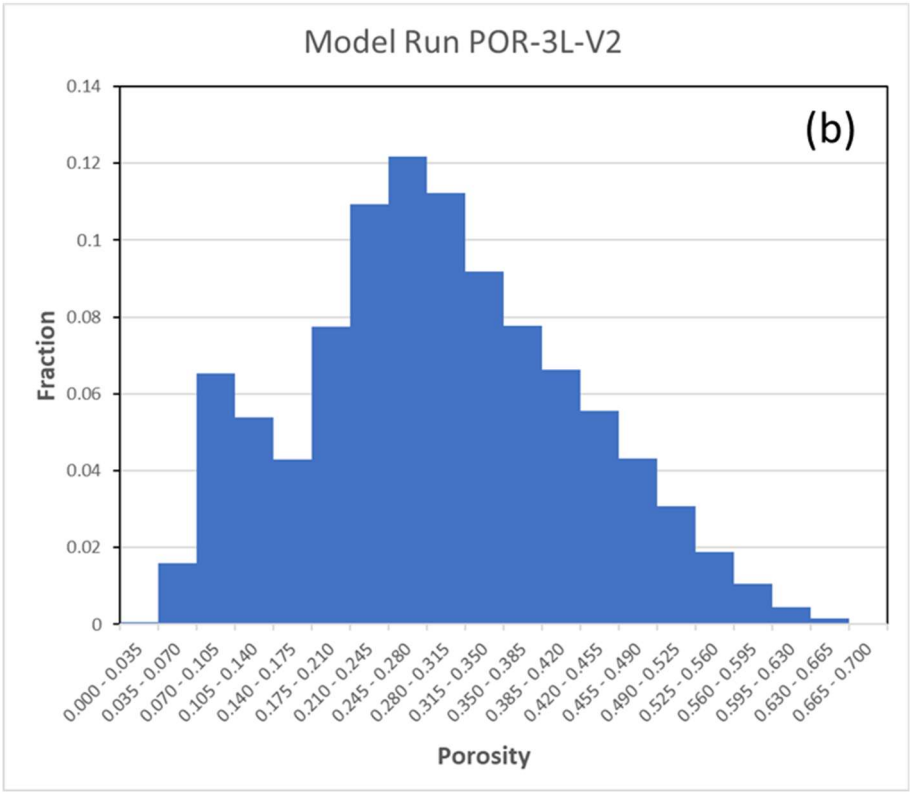

Figure 4-12: Histograms showing the distribution of porosity in grid cells for (a) the undifferentiated (single facies) model POR-UN-V2, and (b) the three-layered model POR-3L-V2.

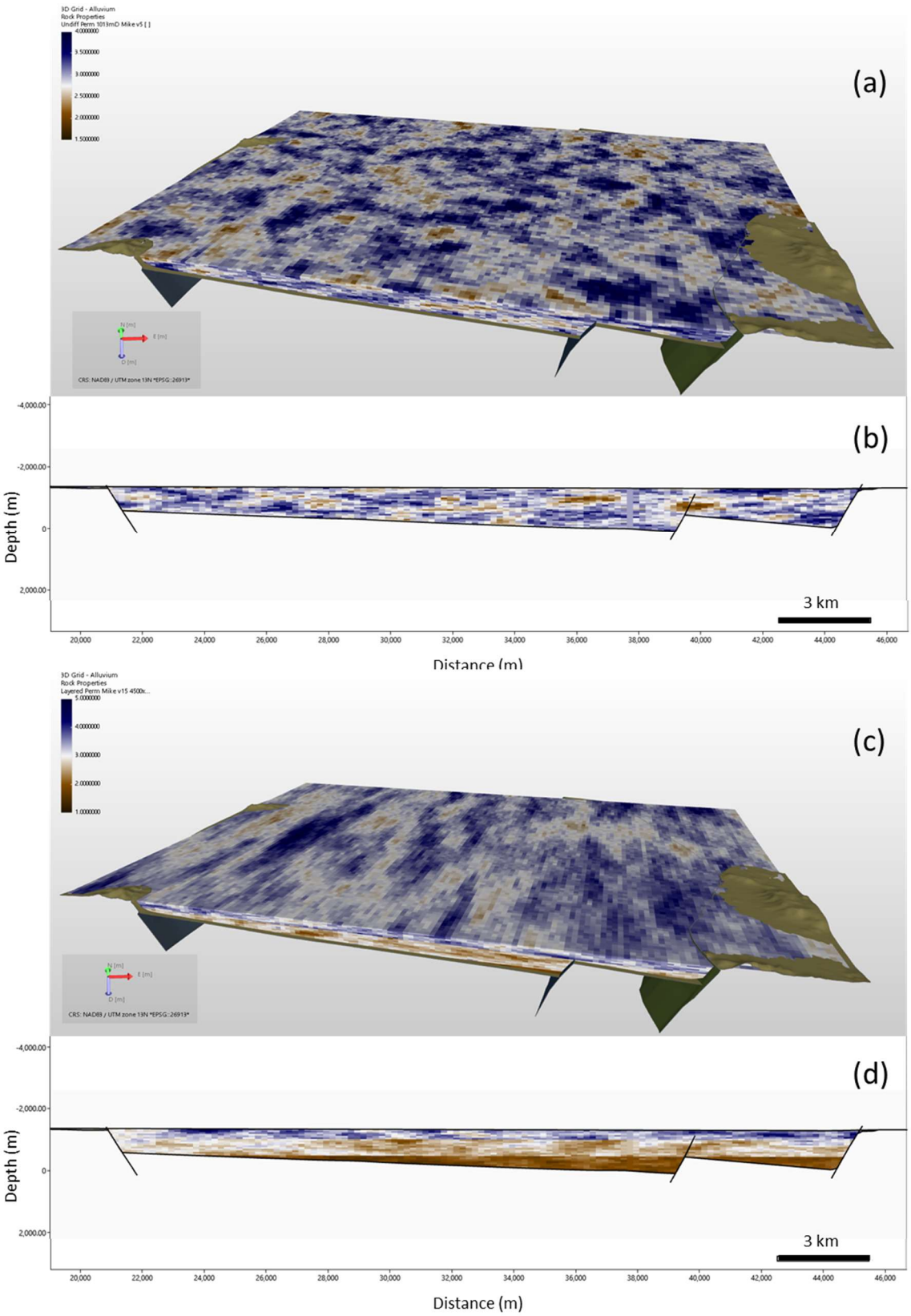

Figure 4-13: Results of permeability modeling in 3D perspectives and basin-normal cross sections for single facies, isotropic (PERM-3L-V1; a, b) and for layered anisotropic (PERM-3L-V3; c, d) cases.

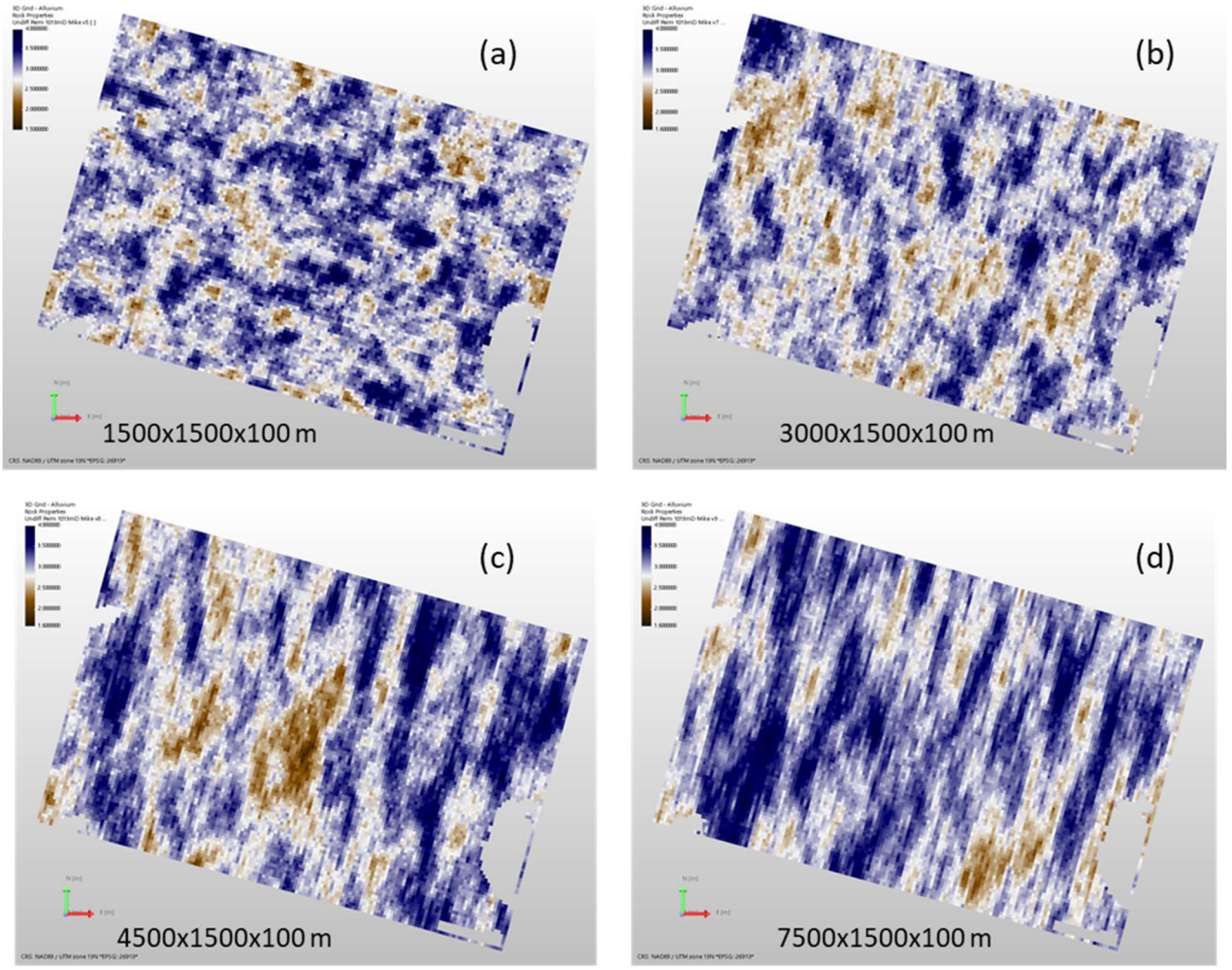

Figure 4-14: Results of permeability modeling for single facies (undifferentiated alluvium) as seen in map view, i.e., top grid layer (k=1): (a) Model PERM-UN-V1; (b) Model PERM-UN-V2; (c) Model PERM-UN-V3; (d) Model PERM-UN-V4. Variogram ranges (major horizontal x minor horizontal x vertical). Axis of the major range is 015° azimuth.

Horizontal anisotropy of physical properties is expected in basin-fill alluvial sediments due to (1) sediment flow during deposition of the alluvium (e.g., channel flow parallel to the basin axis), which controls the geometry of lithofacies units (Gawthorpe and Ledder, 2000; Mack and Stout, 2005) and (2) preferential pathways that develop as a result of post-deposition groundwater flow. Selecting the appropriate degree of anisotropy requires more detailed sampling of the subsurface. Specifically, one needs to evaluate the three-dimensional distribution of hydrostratigraphic units and their physical properties. This can be accomplished through the analysis of coreholes drilled in a grid pattern at the prospect scale (between the sub-basin and repository scales). The preferred direction of permeability may vary across the basin as a function of the depositional environment for each lithofacies, such as axis-parallel for fluvial channels, axis-normal for alluvial fans, and isotropic for lacustrine sediments.

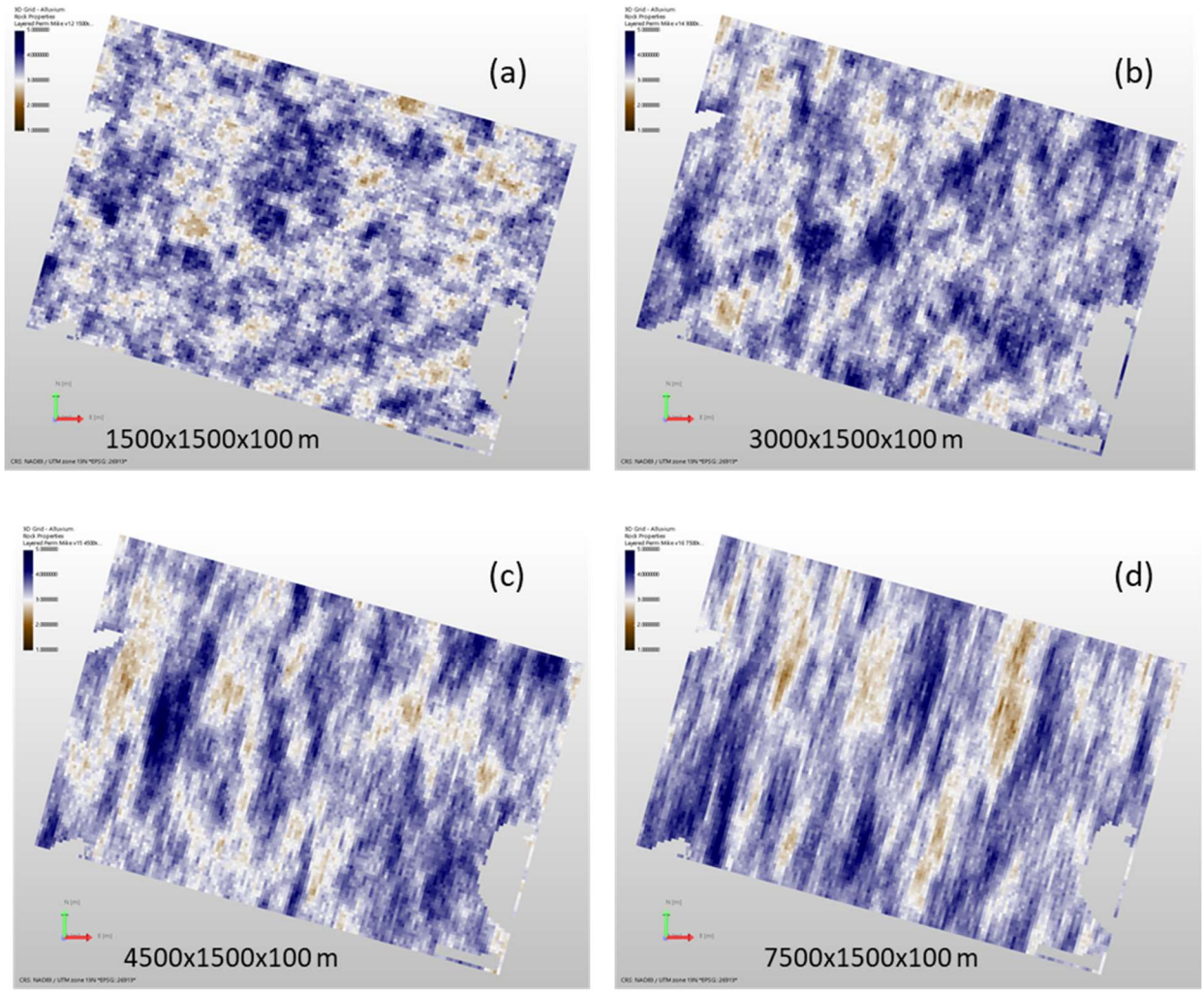

Figure 4-15: Results of permeability modeling for three-layered facies as seen in map view, i.e., top grid layer (k=1): (a) Model PERM-3L-V1; (b) Model PERM-3L-V2; (c) Model PERM-3L-V3; (d) Model PERM-3L-V4. Variogram ranges (major horizontal x minor horizontal x vertical). Axis of the major range is 015° azimuth.

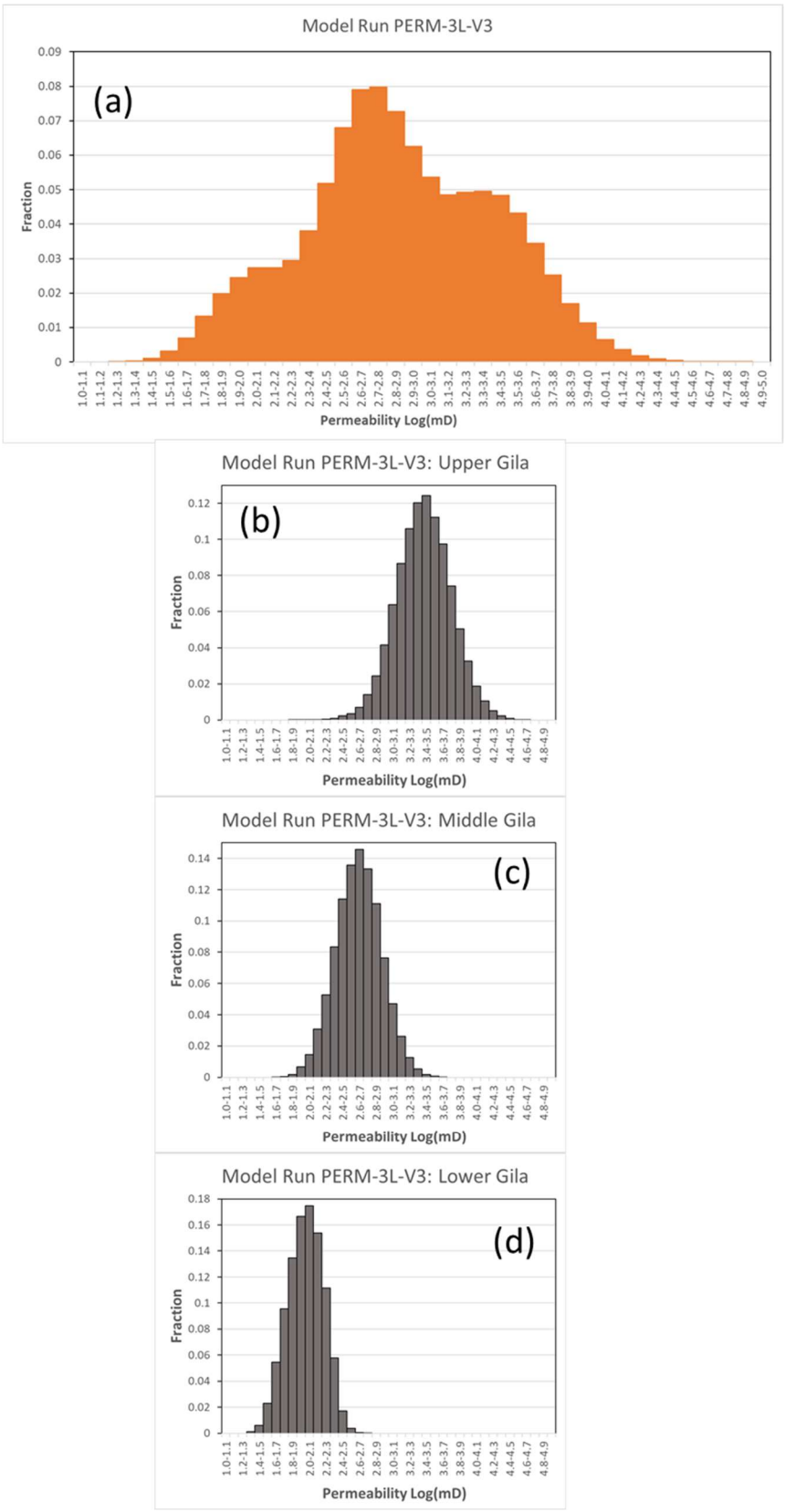

Figure 4-16: Histograms of permeability distribution in grid cells for model PERM-3L-V3. (a) All units combined, (b) Upper Gila, (c) Middle Gila, (d) Lower Gila.

5 Meshing Workflow for Alluvial Basin Case

The workflow outlined herein establishes a connection between JewelSuite™ and downstream geologic modeling applications. This workflow was initially tested in FY19 using synthetic, cube-shaped test cases representing common geologic geometries while development of the full basin JewelSuite™ model was underway. In FY20, the workflow was applied to a small volume extracted from the larger GFM that transects the Central Fault.

We used the following steps for this work. The steps are iterative from building the JewelSuite™ model, to meshing, to the modeling simulations. Each step may reveal changes needed at an earlier step so that all subsequent steps have to be repeated. The iterative nature of this process also highlights the importance of automating the workflow as much as possible.

- Read GOCAD 3D geometry and materials exported from JewelSuite™
- Mesh design, criteria, and considerations
- Create example computational meshes for flow simulations
- Interpolate JewelSuite™ properties to the computational mesh

The simulations were performed using PFLOTRAN (PFLOTRAN, 2020) and FEHM (FEHM, 2020) and compared using the same boundary conditions and computational meshes. PFLOTRAN and FEHM have mesh requirements that ensure the accuracy of simulations used on the mesh. They use a two-point flux approximation across control volume faces that are the Voronoi dual of a Delaunay tetrahedral mesh. Therefore, we use meshing software that can create meshes to meet the Delaunay criteria: LaGriT and Vorocrust.

LaGriT (LaGriT, 2020) is an open source software developed at Los Alamos National Laboratory that provides a variety of meshing tools with capabilities specific to geologic applications and Voronoi control volume solvers. LaGriT is used to generate meshes with control volume discretization such that the underlying control volumes are Voronoi tessellations as required by FEHM and PFLOTRAN. LaGriT also provides tools to write setup files that meet the modeling software requirements. Model setup includes boundary conditions, initial conditions, and properties such as material distribution.

Vorocrust (Vorocrust, 2020) was developed by Sandia National Laboratories and is the first algorithm to generate conforming Voronoi meshes for non-convex domains with curved boundaries. The generated polyhedral cells are true Voronoi cells that are not clipped and hence they maintain convexity, planarity of faces and orthogonality between faces and their dual Delaunay edges. Vorocrust is currently testing capabilities for use in geologic modeling and an example is included in this work. LaGriT is used to create valid surfaces as input for Vorocrust, and to aid in model setup and visualization of the Vorocrust mesh for modeling.

5.1 JewelSuite™ Interface with Meshing

For FY20, we used a small volume of the Deming sub-basin as described in Section 3 to test and refine the GFM handoff to LaGriT. This smaller model extent enabled efficient testing and sharing of files between JewelSuite™ and LaGriT and was used to iterate between mesh generation and simulations before attempting a larger domain.

Figure 5-1 is a vertical slice through the deepest part of the Deming sub-basin model and includes the Central Fault on the eastern side of the sub-basin (Figure 3-14 shows the test-case slice with respect to the full basin domain). There are two material layers: alluvium (orange) and bedrock (green). Below the bedrock is an arbitrary flat bottom. The spatial extent of this example is approximately 10,000 x 400 x 1450 meters. This model is on a diagonal, rotated 15.5 degrees away from the X axis. The transition from JewelSuite™ to LaGriT results in slightly sloped boundaries, i.e., the sides are not straight. For instance, the front varies along a straight line between 0 and -0.0005 m. The top surface has a slight slope with elevation that is defined by the ground surface DEM with a minimum of 1297 and maximum of 1328 meters above mean sea level.

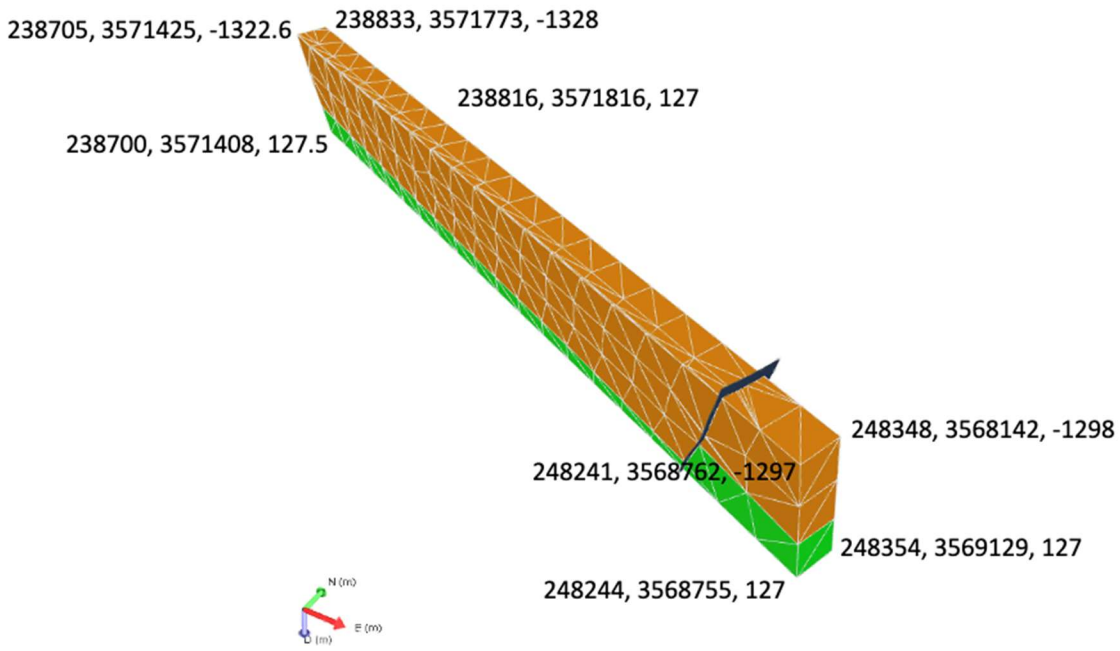

Figure 5-1: JewelSuite™ Example mesh with 2 material zones and a fault with coordinates (rounded integer in meters) at each corner. For JewelSuite™, the Z coordinate is positive depth so negative numbers are above SL, positive are downward depth.

JewelSuite™ can export a tessellated mesh that represents the bounding surface of each geologic volume. The exported mesh must be watertight with no gaps or overlaps between volumes. The mesh formats available for output from JewelSuite™ that were explored include Abaqus, MESH3D (JewelSuite™ mesh3D format) and GOCAD TSolid TETRA format. The GOCAD

file was preferred because it has a consistent file format, includes the geologic model information required for the meshing workflow, and does not contain extraneous data that adds to the file size but is not used.

We developed an interface between JewelSuite™ and LaGriT by adding a GOCAD TETRA reader to the LaGriT software. While many geologic applications use a right-handed coordinate system, JewelSuite™ uses a left-handed coordinate system. The LaGriT GOCAD reader was written to work in general for most applications writing GOCAD, and it can detect the JewelSuite™ convention by the keyword Depth (instead of ELEVATION). LaGriT then does the transformation by multiplying the Z coordinates by -1 and re-ordering the TETRA connectivity so cells are not inside out.

The following coordinates are the 8 corners of the JewelSuite™ mesh in Figure 5-2 converted to the right hand coordinate system, with elevation in meters above sea level.

```
1) 238700, 3571406, -127.164 (lower left corner, min)
2) 248240, 3568760, -127.164
3) 238807, 3571791, -127.164
4) 248357, 3569146, -127.164
5) 238705, 3571423,  1322.135 (upper left corner)
6) 248240, 3568760,  1296.374
7) 238807, 3571791,  1322.418
8) 248347, 3569146,  1296.196 (upper right corner, max)
```

A nice convention of the JewelSuite™ export is the ability to write cell properties to the GOCAD file. The cell property labeled ZoneId represents the geologic volumes or material zones. The CompartmentId cell property are numbers representing ZoneId but divided by fault surfaces so cells on either side of a fault have different identification numbers as shown in Figure 5-2.

LaGriT is used to extract the outside boundary surfaces as well as the internal interfaces as represented by differing cell colors. For ZoneId the surfaces representing a material can be extracted so there is one internal surface between ZoneId 1 and 2. Using CompartmentId the fault surface can be extracted by the surface between CompartmentId 1-2 and 3-4. The extracted surfaces are valid triangulations and used in the meshing process to build a computational mesh. These surfaces can also be used as input for the Vorocrust software representing multiple regions.

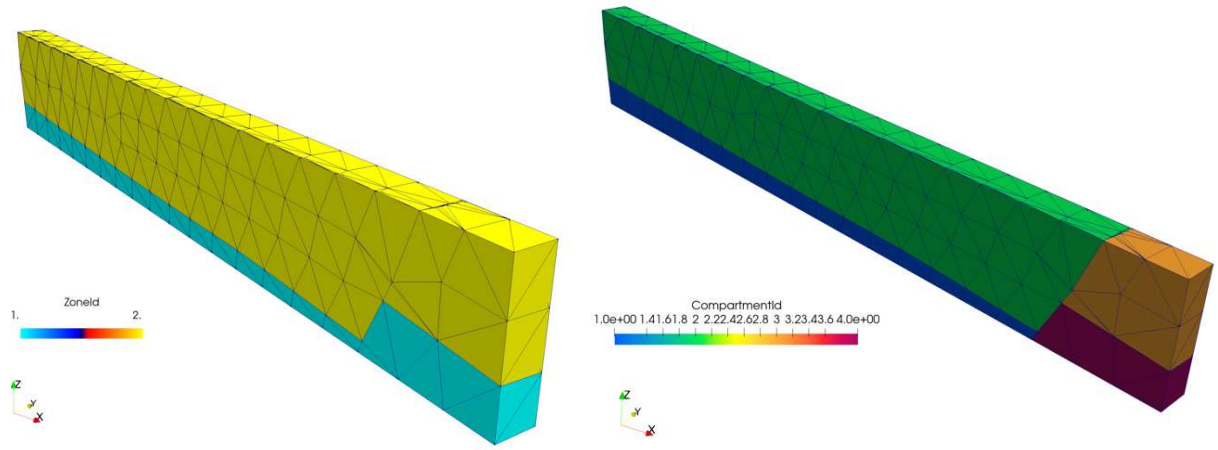

Figure 5-2: Example mesh converted to right hand coordinate system and written in AVS file format showing JewelSuite™ cell properties ZoneId (left) and CompartmentId (right).

5.1.1 GOCAD Mesh File

The GOCAD file format from JewelSuite™ can write user defined vertex and cell properties; it also has default properties available through menu selection. By convention we ignore all user defined properties, but we require the JewelSuite™ cell properties ZoneId and CompartmentId. The GOCAD TETRA mesh file has the following important elements that are used by LaGriT in the meshing workflow. Note the vertex property NodeId is included here as it is often included by default. This property is ignored in the LaGriT workflow.

```
GOCAD TSolid 1 = 3D volume filled tetrahedral mesh

AXIS_NAME "X" "Y" "Z" = x, y, z axis represented
AXIS_UNIT "m" "m" "m" = coordinates in meters

ZPOSITIVE Depth = positive downward distance from 0 (otherwise this is
ELEVATION)

PROPERTIES NodeId = node attributes if they exist, these can be ignored

PROPERTY_CLASS_HEADER NodeId{ = node attribute range of values, can be
ignored
low_clip:1
high_clip:4
}

TETRA_PROPERTIES CompartmentId  ZoneId = cell attributes for compartments and
zones

TETRA_PROPERTY_CLASS_HEADER CompartmentId{ = range of CompartmentId from 1 to
max
low_clip:1
high_clip:3
```

```
}
}
TETRA_PROPERTY_CLASS_HEADER ZoneId{ = range of ZoneId from 1 to max
low_clip:1
high_clip:2
}

VRTX or PVRTX = id, xyz location of element vertices (nodes) followed by
attribute values for that point
TETRA = element connectivity of 4 vertices followed by attribute values for
that element
```

5.2 Meshing for Modeling

The meshing step includes the design and building of appropriate computational meshes for simulations. Specific constraints for accuracy and numerical stability are imposed by the modeling application; these constraints are important because depending on the mesh, you can get a stable but inaccurate solution to the physics (Zyvoloski and Vesselinov, 2006). The design is chosen with consideration of the physics to be modeled, mesh size restrictions versus mesh resolution needed for model features, and the mesh and model information needed by the model application. As such, we optimized our mesh design and meshing method to give the best performance from the modeling application with respect to the difficulty in generating the mesh.

5.2.1 Measures of Mesh Quality

The mesh design determines which quality measures are most important and establishes the criteria by which the mesh quality is evaluated. Some mesh qualities are measured, others are subjective or balanced with other criteria. Quality may relax in one criterion but not in another. For instance, if there is a mesh size restriction, the domain and resolution will be opposing criteria: if the domain is large, resolution must be coarse, but if high resolution is needed, then the domain must be small. The measures we used to determine mesh quality for this work are listed below. The order of priority is dependent on modeling goals and user specifications.

- Mesh size (number of vertices, number of cells) is within user specified range
- Mesh Topology: No holes, fully connected, no duplicate vertices
- All cell volumes are positive and within the user specified range
- Aspect ratio of cells are within the user specified range
- Satisfies Delaunay Criteria or other Modeling Specifications
- Satisfies the needs of the physics to be modeled
- Conforms to the geometric model within user specified range
- Coordinate system and domain are within user specifications
- Adequate Resolution for representation of geostatistical properties

There are various meshing methods, both structured and unstructured, with adaptive refinement to geological features. The easier method is to use a structured mesh with fine resolution, or a coarser mesh that uses octree refinement to increase resolution in user-specified regions of interest. These result in stair-stepped rather than smooth geometries but can be acceptable where the geometry spacing is small relative to the full model domain (Sentis and Gable, 2017). The unstructured approach creates meshes that exactly conform to the geometric model but require some expertise in building the mesh such that it will also meet the Delaunay criteria.

The computational mesh statistics and quality measurements are included to aid in model setup and to understand the quality of the mesh that is being used. This information includes a summary of vertex counts for the various zones, spacing and quantity counts, and the cell and vertex Voronoi volumes. The numbers for the geometric coefficient matrix are reported and can give an indication of local orthogonality by checking for negative coupling coefficients and negative Voronoi volumes.

5.3 Example Computational Meshes for Modeling

Here we present four mesh designs that were tested for their potential to scale to the full model domain. We used a sub-set of the GFM volume which was small enough for many iterations during the workflow and modeling. Computational meshes were created for modeling flow simulations and were used to verify mesh design, quality, and model setup.

The computational meshes were created using different methods including structured, stacked layers, and a Vorocrust polyhedral mesh. We used these meshes to explore resolution in order to determine a spacing that was coarse enough to keep the size small and simulations fast, but with enough resolution to capture the slope of the interface between the alluvium and bedrock. Table 6-1 shows a summary of the mesh types and sizes. A full description of each mesh is provided in the following sections.

Important considerations for our simulations were (1) whether a mesh that was not aligned parallel to an axis would be affected by numerical issues, and (2) the potential difficulty in aligning a mesh to the x-axis. As such, Mesh 1 uses a structured mesh method with flat boundaries and aligned along the x-axis. This was the easiest method to use for model setup, and it satisfies the Delaunay criteria. The structured mesh can later be used to add octree refinement to increase resolution in user specified regions of interest. These structured and octree meshes result in stair-stepped rather than smooth geometries, so spacing is selected such that geometry is acceptable for the simulations.

Mesh 2 is the same as Mesh 1 except the mesh is kept on the diagonal (15.5 ° rotation from the x-axis). All mesh and model setup files are the same for both meshes. Simulations are run and compared using both FEHM and PFLOTRAN each with the same input parameters. Section 6 shows the comparison results.

Mesh 3 uses Vorocrust to generate a Voronoi mesh that conforms to the input surfaces used in Mesh 1 and Mesh 2. The outside boundaries are flat and there is one internal surface following the interface between materials. Vorocrust currently has few controls for the resolution and distribution of cells but does have a maximum radius parameter. The Vorocrust algorithm creates a mesh conforming to the input geometry and guarantees this mesh satisfies the Delaunay criteria needed by the modeling applications.

For Mesh 4, we attempted a method using the surfaces from JewelSuite™ to create a mesh with conforming geometry. The difficulty is designing a mesh that captures the slope but will then connect into a tetrahedral mesh that satisfies the Delaunay criteria. We used the stacked layers method to create a 2.5 dimensional mesh with regular spacing in the *x,y* directions but with layers stacked proportionally between surfaces for variable vertical spacing. Simulations were not run on this mesh as it does not satisfy the necessary Delaunay criteria. The mesh is included here for discussion to illustrate the benefits of this mesh, and also the difficulty and issues in creating a Delaunay mesh.

Table 5-1: Computational Mesh Type Summary for Examples 1-4

	Method	Cell Size (meters)	Vertices	Cells	Min Volume	Max Volume
1	Structured Aligned	50 x 50 x 20	120,992	103,950	8333.33	8333.33
2	Structured Diagonal	50 x 50 x 20	120,992	103,950	8333.33	8333.33
3	Vorocrust	10 – 100 edge lengths	131,043	24,967	1408	2,486,226.20
4	Stacked Layers	50 x 50 x variable Z	38,618	197,269	.0092	73281.45

5.3.1 Mesh 1 Structured Aligned

Structured meshes are the easiest to create. They consist of a rectangular domain broken into cells of equal sizes in 3 directions. When this point distribution is connected into a tetrahedral mesh, it satisfies the Delaunay criteria. The GFM geology is interpolated onto the mesh cells and vertices. This method is often used for large domains with complex geology and faults where the stair-step effect is minimal compared to the full model. The method is also useful for creating quick meshes for multiple simulations to explore possible mesh effects and help determine mesh resolution.

Although structured meshes are not as flexible as unstructured meshes in fitting complex geometry, tests have shown that they provide accurate solutions so long as there is adequate resolution to represent the geometry of the different materials in each hydrogeologic layer. Moreover, there must be enough resolution to account for any large gradients. The sufficiency of grid resolution is usually investigated by running a flow model using various grids of differing resolutions.

Various spacing scenarios were tried from 100 meters to 10 meters. The spacing of 50 meters in the horizontal is adequate for simulations and a good size for many simulations. The width of the mesh was reduced to 350 meters from 399.005 meters so the vertices would align on integer coordinate numbers. We used a vertical spacing of 20 meters to better capture the slope of alluvium caused by the fault. The 50 x 50 x 20 meter spacing results in a mesh size that is easy and fast to run in modeling applications, but still captures enough of the alluvium shape to represent the physics imposed by the geology. For improved numerical accuracy, the lower left corner of the mesh is translated to 0,0. The elevations are unchanged. See the mesh image in Figure 5-3.

Alignment along an axis is the preferred arrangement since modeling setup is much easier. Boundaries are flat on each of the coordinate axes, minimum and maximum coordinate values are on the mesh, and it is easy to locate cells for tracer inputs and other setups. Cells are aligned so faces are in the same direction as the flow simulations.

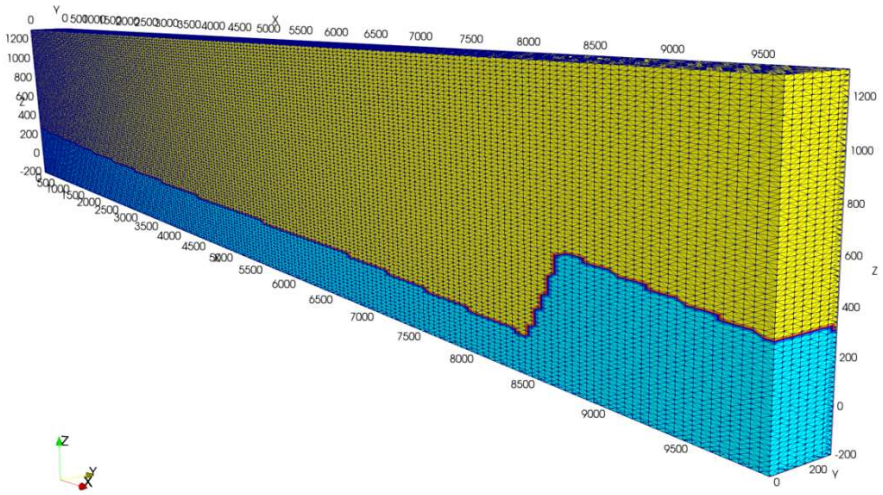

Figure 5-3: Mesh 1 Tetrahedral structured mesh with flat boundaries and aligned with the X-axis. Zone 1 (blue) is bedrock, Zone 2 (yellow) is alluvium.

Mesh 1 satisfies the following criteria:

- Mesh size (number of vertices, number of cells) is within user specified range
- Mesh Topology: No holes, fully connected, no duplicate vertices
- All cell volumes are positive and within the user specified range
- Aspect ratio of cells are within the user specified range
- Satisfies Delaunay Criteria or other modeling specifications
- Satisfies the needs of the physics to be modeled

The following criteria could be improved but are acceptable:

- The top is flat instead of conforming to the alluvium data, interface is stair-stepped.
- Domain is not as wide as desired but adequate for this work
- The resolution may be too coarse for geostatistical properties, but this feature was not used

5.3.2 Mesh 2 Structured Diagonal

Mesh 2 is the same as Mesh 1 except the coordinates remain on the diagonal and are not rotated to align along an axis. This diagonal orientation can be seen in Figure 5-4. Because the mesh vertex numbers are the same as Mesh 1, the setup files for modeling are the same. Only the geometry file with the coordinate information is different.

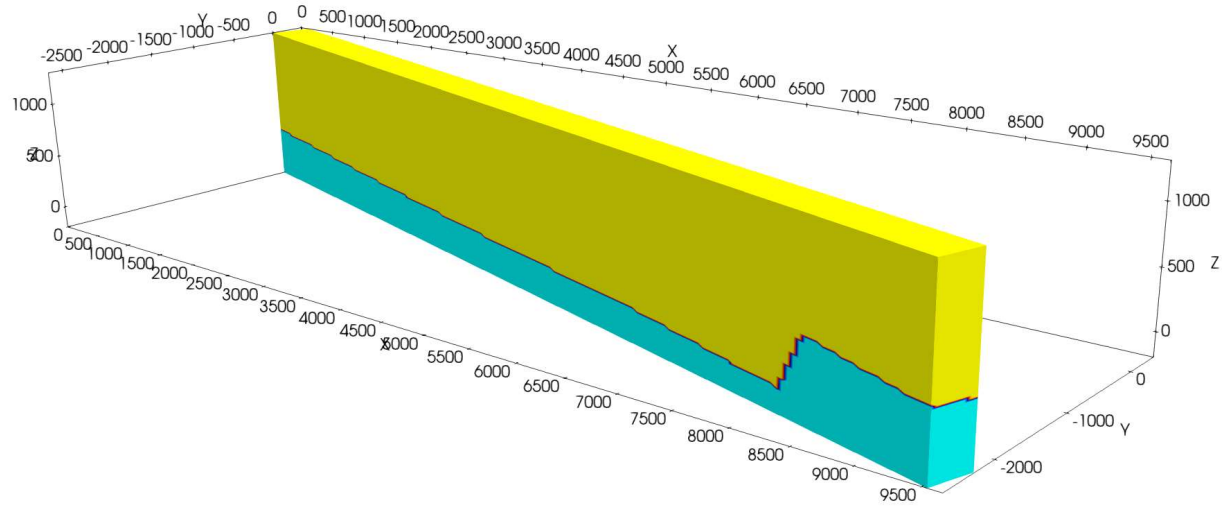

Figure 5-4: Mesh 2 Tetrahedral structured mesh with flat boundaries on diagonal with respect to the axis. Zone 1 (blue) is bedrock, Zone 2 (yellow) is alluvium.

Mesh 2 satisfies the following criteria:

- Mesh size (number of vertices, number of cells) is within user specified range
- Mesh Topology: No holes, fully connected, no duplicate vertices
- All cell volumes are positive and within the user specified range
- Aspect ratio of cells are within the user specified range
- Satisfies Delaunay Criteria or other modeling specifications
- Satisfies the needs of the physics to be modeled

The following criteria could be improved but are acceptable:

- The top is flat instead of conforming to the alluvium data, interface is stair-stepped.
- Domain is not as wide as desired but adequate for this work, cells aligned on diagonal may affect the simulations
- The resolution may be too coarse for geostatistical properties, but this feature was not used

5.3.3 Mesh 3 Vorocrust

This mesh was created using Vorocrust with the parameter maximum radius set to 100 m. This mesh is guaranteed to satisfy the Delaunay criteria, but it was difficult to distribute cell spacing

in a more isotropic manner. The mesh size is appropriate for simulations, but the large range of volumes from 0.0092 to 73,281 cubic meters may impact simulations (Section 6).

Figure 5-5 and Figure 5-6 are images of the outside surface of the Vorocrust mesh showing how the Voronoi polyhedral faces form a triangulation of the outside boundary. This shows a nice result and conforms to the material interface. Figure 5-7 and Figure 5-8 are the Vorocrust mesh clipped at Y = 200 meters and shows the polyhedral cells inside the mesh conforming to the material interface.

At present Vorocrust does not have the tools for locally controlling distribution and resolution, but it will always create a Delaunay mesh that conforms to the input boundaries.

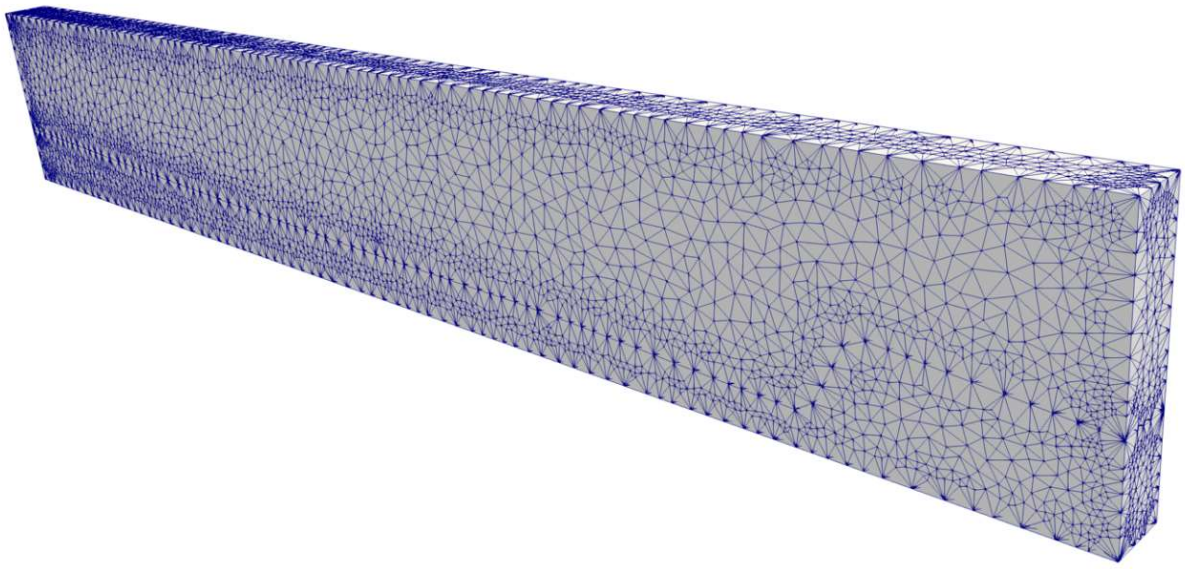

Figure 5-5: Vorocrust Mesh 3 with flat outside boundaries and the material interface from the geologic model

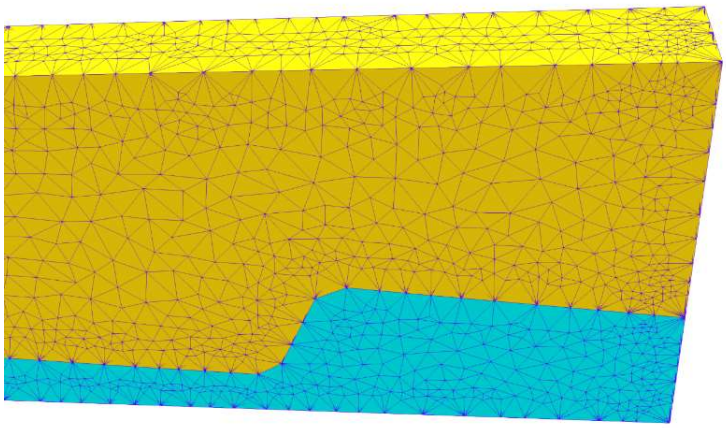

Figure 5-6: Close up of Vorocrust Mesh 3 showing material interface between Zone 1 bedrock (blue) and Zone 2 alluvium (yellow). This shows the distribution of cells along the boundaries and internal to each material region.

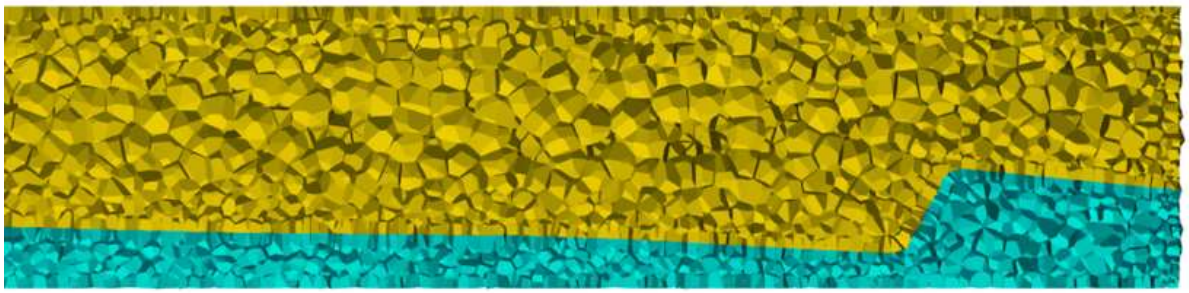

Figure 5-7: Mesh 3 from Vorocrust clipped at Y = 200 meters to show the polyhedral cells that fill the mesh volume.

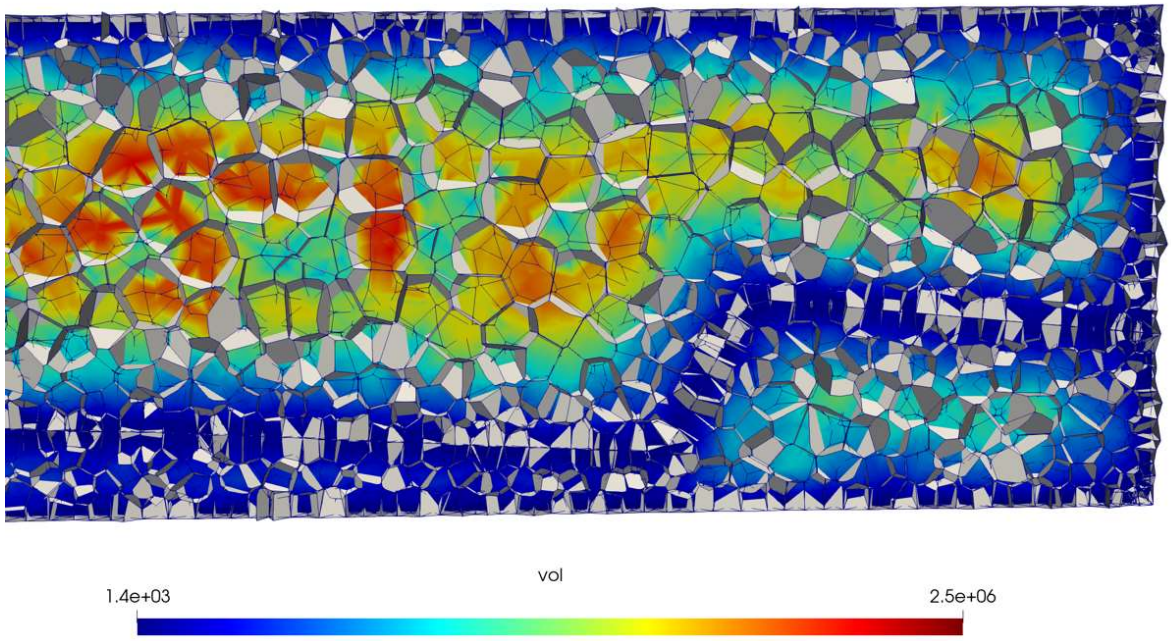

Figure 5-8: Mesh 3 from Vorocrust clipped at Y = 200 meters showing the polyhedral cells with a surface colored by the cell volumes. Cell volumes range from 0.0092 (dark blue) to 73,281 (dark red) in cubic meters.

Mesh 3 satisfies the following criteria:

- Mesh size (number of vertices, number of cells) is within user specified range
- Mesh Topology: No holes, fully connected, no duplicate vertices
- Aspect ratio of cells are within the user specified range
- Satisfies Delaunay Criteria
- Satisfies the needs of the physics to be modeled
- Conforms to the geometric model

The following criteria could be improved but are acceptable:

- All cell volumes are positive, but the large range of volumes may impact simulations
- Domain is not as wide as desired but adequate for this work
- The geostatistical properties were not used and do not apply

We do not have an interface for writing Vorocrust files for FEHM, but a PFLOTRAN interface is being developed. Sandia provided the PFLOTRAN model files from Mesh 3 Vorocrust for our simulations.

5.3.4 Mesh 4 Stacked Layers

This method is used when the surfaces of the GFM need to be represented as accurately as possible. Commonly used for watershed models, the method has been scripted to work with GIS as input data into a LaGriT module called Tinerator. Depending on the vertical resolution and slope of the surfaces it can be difficult to generate Delaunay meshes. Modeling applications that compute on hexahedral or general polyhedral meshes that do not have the Delaunay restrictions are most successful with these types of meshes.

For a model with horizontal non-intersecting surfaces, we can create a computational mesh with conforming interfaces by using a stacked mesh method. We first create quadrilateral surfaces with elevations interpolated from the GFM elevations. The surfaces and intermediate layers are then stacked into a 2 ½ Dimension hexahedral mesh as shown in Figure 5-9.

The hexahedral mesh points are connected into a tetrahedral mesh as required by the modeling applications. The various mesh-layer distributions attempted resulted in undesirable connections crossing the interface between material zones (Figure 5-10). Also, because the top has a slight but non-convex slope, connections are created across the top. The top outside cells can be removed but may result in poor coupling coefficient values. The interface issue can only be fixed by careful selection of layers and resolution along that interface, so connections do not cross the boundary.

The geometric coefficient matrix for this mesh has too many negative coefficients for simulations. The solutions may be stable but inaccurate and transport may have inaccurate local effects. The impact can be mitigated by adjusting the mesh resolution. Generally high aspect ratio tetrahedra (long dimension along the external boundary) are more of a problem. This means that mesh refinement that brings the mesh closer to unit aspect ratios will help.

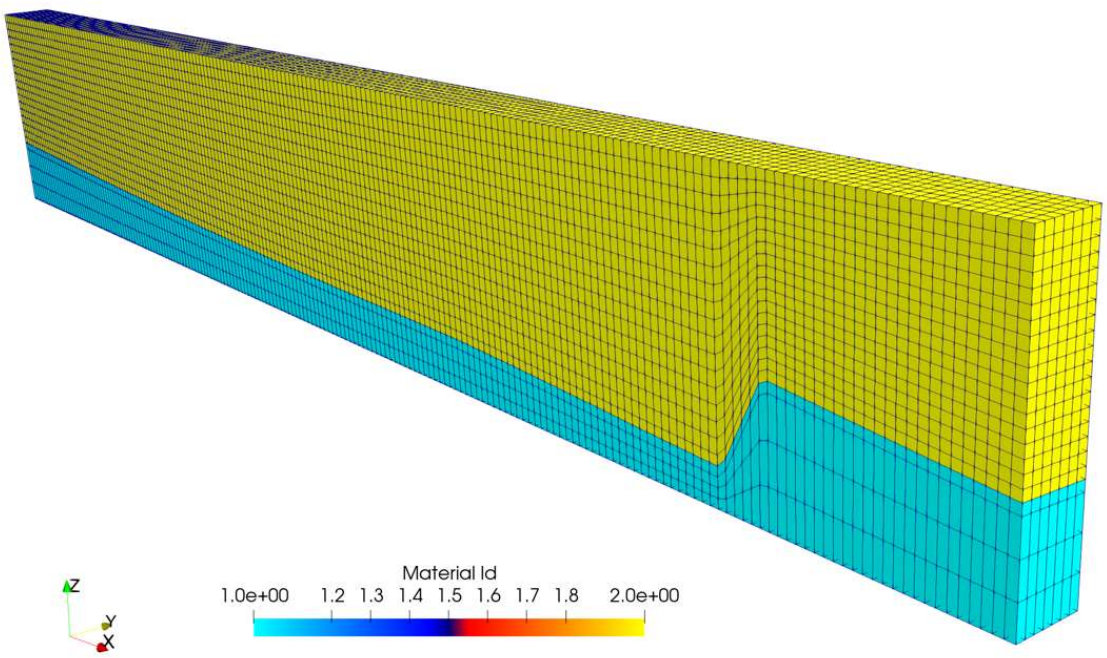

Figure 5-9: Mesh 4 Stacked layer mesh using the GFM top and bottom Alluvium surfaces. The quadrilateral surfaces are stacked into hexahedral cells. These cells align nicely along the interface between the Alluvium (yellow) and Bedrock (blue).

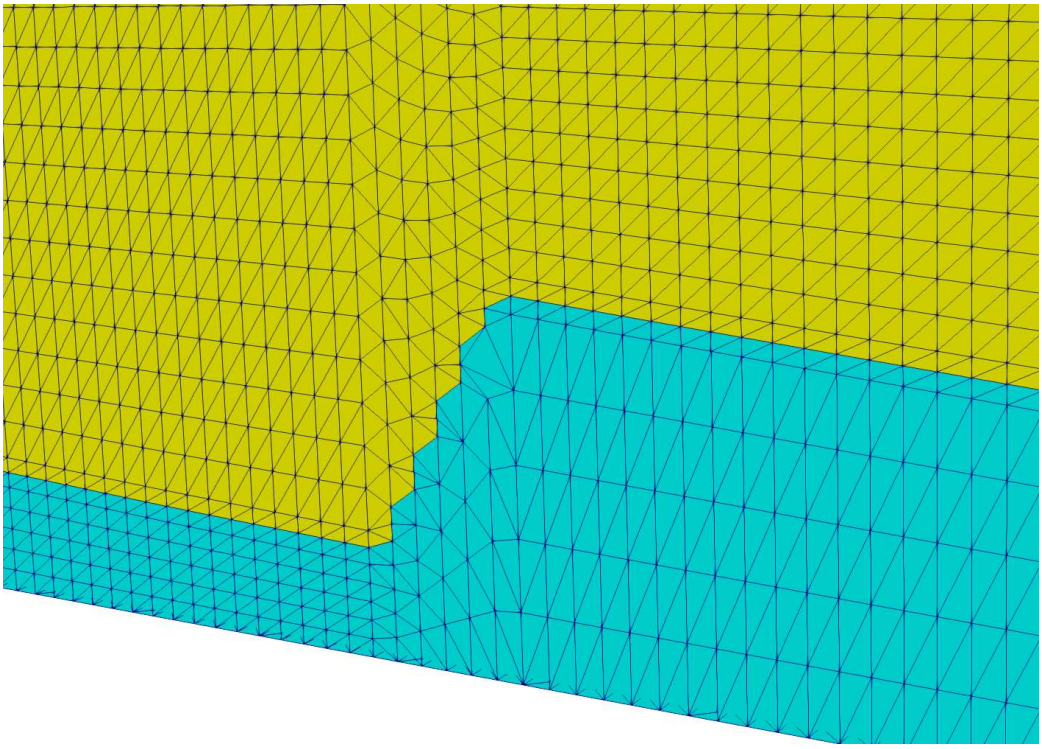

Figure 5-10: Mesh 4 Stacked point distribution is connected into a tetrahedral mesh using the Delaunay algorithm. The smooth interface between material zones is broken by tetrahedral connections crossing the interface between Alluvium (yellow) and Bedrock (blue).

During the evaluation of the mesh, LaGriT was used to report mesh statistics and a summary of Voronoi volumes. This is a quick check to determine if a mesh can be used for simulations. The values for this mesh indicate a problem. The following report shows a large number of cells with a very undesirable aspect ratio less than 0.01. Looking at the summary for the coefficient matrix, we see there are 137 Negative coupling coefficients. Therefore this mesh is not used in simulations.

```
----------------------------------------
elements with aspect ratio < .01:                4661
elements with aspect ratio b/w .01 and .02:        73
elements with aspect ratio b/w .02 and .05:        28
elements with aspect ratio b/w .05 and .1 :         0
elements with aspect ratio b/w .1  and .2 :         2
elements with aspect ratio b/w .2  and .5 :        19
elements with aspect ratio b/w .5  and 1. :    192486
min aspect ratio =  0.2392E-07  max aspect ratio =  0.9517E+00
----------------------------------------
element volumes b/w  0.9210E-02 and  0.2210E+00:       63
element volumes b/w  0.2210E+00 and  0.5304E+01:     1456
element volumes b/w  0.5304E+01 and  0.1273E+03:     3069
element volumes b/w  0.1273E+03 and  0.3054E+04:      174
element volumes b/w  0.3054E+04 and  0.7328E+05:   192507
min volume =   9.2104167E-03  max volume =   7.3281457E+04
---------------------------------------------------------


AMatbld3d_stor: Matrix compress_eps:  0.1000000E-07
AMatbld3d_stor: Local epsilon:  0.1000000E-14
AMatbld3d_stor: *****Negative Coefficients ******
AMatbld3d_stor: Total Number of Negative Coefficients 137
AMatbld3d_stor: Number of Significant Negative Coefs  137
AMatbld3d_stor: npoints =    38618  ncoefs =     532148
AMatbld3d_stor: Number of unique coefs =    285383
AMatbld3d_stor: Maximum num. connections to a node =  19
AMatbld3d_stor: Volume min =   1.7145554E+04
AMatbld3d_stor: Volume max =   3.0769451E+05
AMatbld3d_stor: Total Volume:   5.2253028E+09
AMatbld3d_stor: abs(Aij/xij) min =   0.0000000E+00
AMatbld3d_stor: abs(Aij/xij) max =   1.2251706E+02
AMatbld3d_stor: (Aij/xij) max =   8.4827001E-05
AMatbld3d_stor: (Aij/xij) min =  -1.2251706E+02
AMatbld3d_stor Matrix coefficient values stored as scalar area/distance
AMatbld3d_stor Matrix compression used for graph, not coefficient values
cmotet attribute with voronoi volumes created with name vorvol
```

Mesh 4 satisfies the following criteria:

- Mesh size (number of vertices, number of cells) is within user specified range
- Mesh Topology: No holes, fully connected, no duplicate vertices
- All cell volumes are positive and within the user specified range
- Aspect ratio of cells are within the user specified range
- Coordinate system and domain within user specifications
- Adequate resolution for representation of geostatistical properties

The following criteria could be improved with more time and work:

- Does not satisfies the needs of the physics to be modeled since irregular tetrahedral cells across the sloped interface would be problematic
- Does not conform to the geometric model at the sloped interface
- Does not satisfy mesh modeling criteria, many negative coupling coefficients
- The geostatistical properties were not used and do not apply

5.4 Setup and Files for Modeling

Once the mesh is created, the computational mesh and setup files are written for the modeling application. These include the geometric coefficients for the Voronoi volumes, zone lists that can be used separately or together to identify vertices of various materials, and zone lists for vertices on the boundaries. Vertex or cell sets are written if needed for the simulation, such as a line of vertex to represent a well or fault feature.

These files are similar for both FEHM and PFLOTRAN but they have different file formats. The following model setup files were written.

5.4.1 Mesh Geometry

This file represents the mesh geometry. It includes the mesh vertex id and location and the cell id with connectivity for each tetrahedra. This file is simply a re-format of the LaGriT mesh into a file format required by the modeling applications.

5.4.2 Mesh Geometric Coefficients

The Geometric Coefficients file represents the topology and contains the sparse matrix geometric coefficients (topology, distance, area, volume). A report is generated when this file is written that provides a summary of min-max values and possible issues like negative coupling coefficients. This provides a first step evaluation of the mesh before it is used in the modeling application.

5.4.3 Material Zones

Computational meshes have each vertex and cell labeled with positive integer id. These are referred to as the mesh material or zone ids and represent the geology from a GFM (Section 3). These numbers are used by the modeling application to apply rock properties and other values for simulations. For these computational meshes, material 1 represents bedrock and material 2 is alluvium.

Example Mesh 1 Materials:

```
Model file: tet_material.zone

Material  1 Bottom   has  29356 nodes. #nodes/nnodes is   0.242627605796
Material  2 Alluvium has  91636 nodes. #nodes/nnodes is   0.757372379303
```

5.4.4 Outside Boundary Zones

Boundary files are written to represent areas of the outside faces of the mesh representing each of 6 directions: top, bottom, front, right, back, and left. For FEHM these are lists of nodes in each zone, for PFLOTRAN these are lists of faces in each zone.

Example Mesh 1 Outside Zones:

```
Model file: tet_outside.zone

Face top           1 has      1592 nodes.
Face bottom        2 has      1592 nodes.
Face left_w        3 has       608 nodes.
Face right_e       5 has       608 nodes.
Face back_n        6 has     15124 nodes.
Face front_s       4 has     15124 nodes.
```

5.4.5 Well Column Zones

LaGriT can be used to select columns of nodes within cylindrical regions. A list of node numbers is written for each well zone. For these simulations the well columns are on Y = 200 meters. The first node column to the right of the fault is at 8700 meters. The fault is at X = 8500 meters, while 8700 meters is the edge of fault. The same zone files can be used for both the diagonal and aligned meshes as the node numbers and ordering are the same for both.

Example Mesh 1 Well Zones:

```
Each well has 76 nodes
well_35.zonn at x = 8500
well_36.zonn at x = 8700
well_37.zonn at x = 9000
well_38.zonn at x = 9300
well_39.zonn at x = 9600
well_40.zonn at x = 9900
```

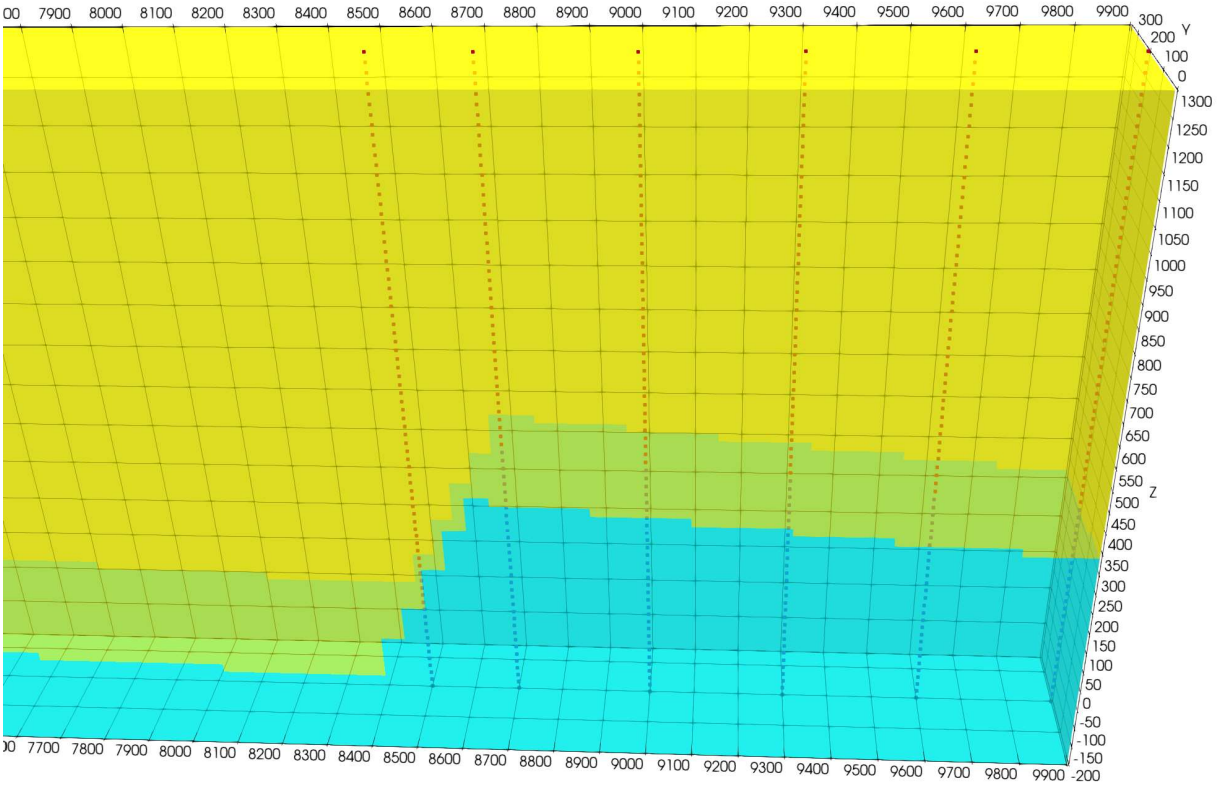

Figure 5-11: Columns are selected to represent well locations (red points) along the tracer pathway and near the middle of the mesh at Y = 200 meters.

5.4.6 Water Table Zones

Water table Zones are selected by using LaGriT to identify nodes above and below the chosen water table elevation of 800 meters. These are written to separate zone files.

Example Mesh 1 Water table Zones:

```
Model Files: wtr_above.zonn wtr_below.zonn

THE PSET   wtr_abv   HAS       39800 POINTS
THE PSET   wtr_blw   HAS       81192 POINTS
```

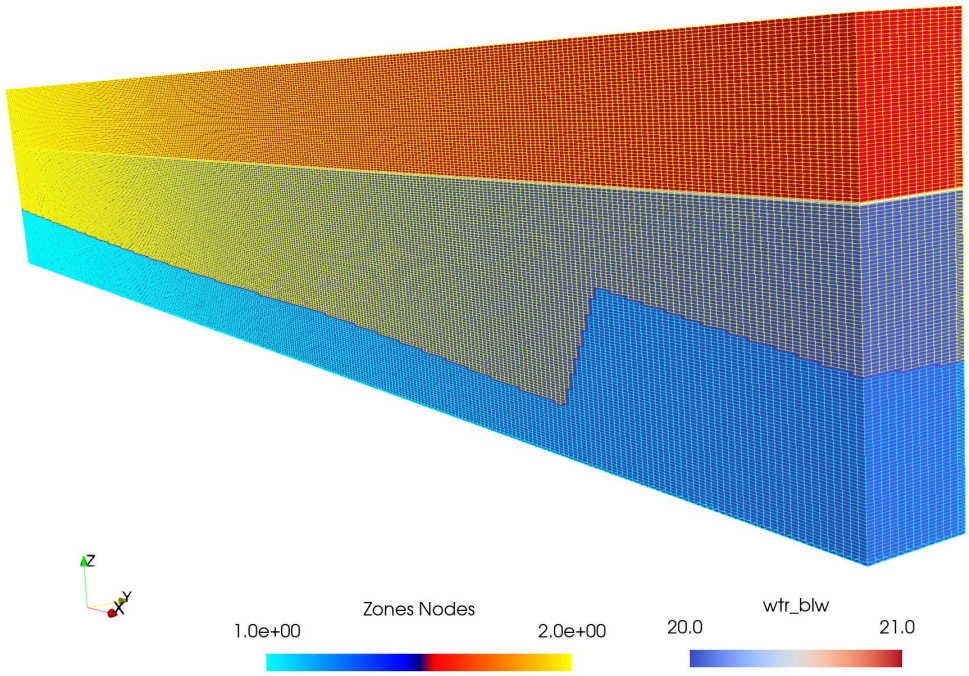

Figure 5-12: Structured mesh showing Water Table Zones above (red) and below (navy blue). Material Zones of Alluvium (yellow) and Bedrock (light blue) are shown.

5.4.7 Tracer Source

LaGriT can be used to identify a tracer source for modeling. A cell or vertex within a geometric box is used to find the number needed. For instance FEHM uses a tracer source at node number 35881 near (3000, 240, 200). For PFLOTRAN the cell with ID 35881 is a cell centered at (3000, 240, 200). The Vorocrust cell center point is located and shown in Figure 5-13.

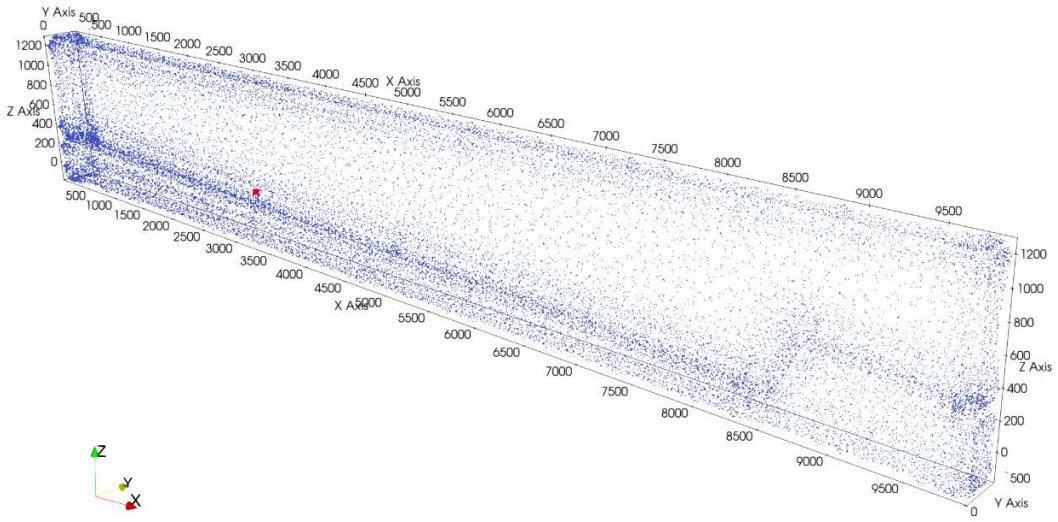

Figure 5-13: Mesh 3 Vorocrust polyhedral cell center points (blue points) and selected tracer source point (red).

5.5 Geostatistical Properties from JewelSuite™

JewelSuite™ has advanced tools for defining geologic properties such as permeability and porosity. We developed a method to read the properties calculated in JewelSuite™ and then apply them to the computational mesh as a mesh attribute that can be used for simulations. Using LaGriT, these property values can be interpolated onto a computational mesh by using the upscale command. This algorithm captures all geostatistical data points located inside a mesh Voronoi volume. Preferably each volume will contain a number of data points. The data points for a volume may have a range of property values. To assign a single value on the mesh, these point values are averaged or selected by a minimum-maximum criterion.

We first tried to export property data in the GOCAD mesh file as vertex or cell properties. However, the resulting file was inconsistent and made the GOCAD mesh file large and complicated. The JewelSuite™ 3D grid can be used to generate a property point set with higher resolution than the computational grid. This is preferred over the 3D mesh, which has very coarse and irregular volumes filled with tetrahedral volumes. Writing the property data sets of disconnected point data from the grid is faster and has smaller file sizes than data exported via the 3D mesh. Some JewelSuite™ file export options were explored, and the best solution is described here.

JewelSuite™ material properties are modeled using an internal 3D grid with resolution controlled by using the *k-layers* option (Section 3). The "no *k-layers*" 3D grid has numerous single, vertical cells to represent each volume, whereas the "*k-layers*" 3D grid contains more complexity within each volume based on the number of *k-layers* selected.

JewelSuite™ exported a test file of *x,y,z* coordinates with their associated property values. For this file, the property value is a calculation of distance from a well inserted into the domain. The property point set is shown in Figure 5-14 and was correctly exported from JewelSuite™ into LaGriT.

The JewelSuite™ point data file is in tabular form with rows of each point *x, y, z* (elevation) followed by the property value. The “#” character is added to each line of the header so LaGriT knows to skip the non-data lines.

```
# 3D Grid 1  (9, 198, 15)  Start Depth 1
# 4
# X  Unit m
# Y  Unit m
# Z  Unit m
# Distance  Template Distance  Unit m
238731.719422316 3571423.93279472 -422.930961234996 6719.94291785036
238779.900945972 3571410.57087416 -423.15766431377  6670.28112964709
238828.082468495 3571397.2089556  -423.386984220641 6620.62472790031
```

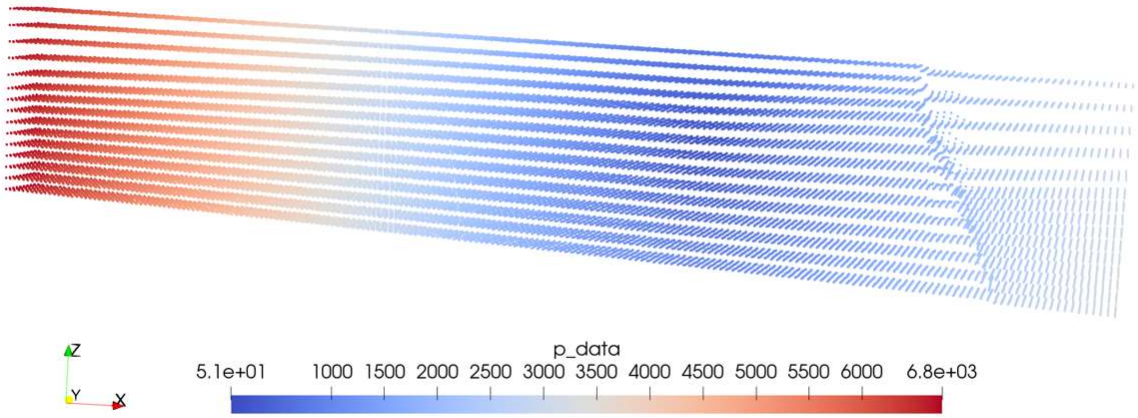

Figure 5-14: Point set property data calculated by JewelSuite™ with distance from a well as the property value.

The property data from this point set is interpolated onto the Mesh 1 computational mesh (Figure 5-15). The sparse result illustrates the importance of spacing for these property data. The computational mesh spacing is 50 x 20 meters, but the point data is about 50 meters in the horizontal, and 100–200 meters vertical. Therefore the property data are sparsely represented on the mesh.

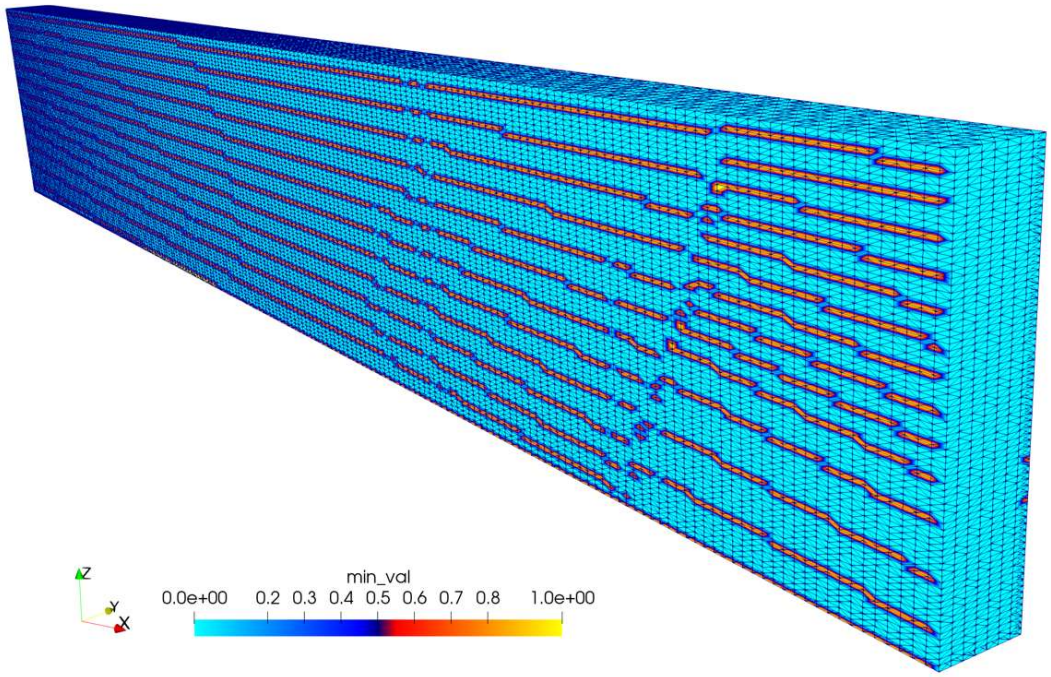

Figure 5-15: Point set property data upscaled to computational mesh. The property value of 1 is upscaled to the computational mesh to show the property data resolution with respect to the computational mesh. Property node sets need to have spacing that is finer than the computational meshes for upscaling to work as intended.

5.6 Mesh Discussion for Full Basin Model

In summary, the easiest method for a computational mesh that satisfies all the modeling criteria is an orthogonal structured mesh with flat boundaries. However, this type of mesh will not have cells that conform to the slopes of the alluvium surfaces. Strategies for improving this include octree refinement at selected regions or stretching the mesh vertically to fit the alluvium surface. Both these methods require simulations to test the sufficiency of the mesh resolution. A better solution would be to run the flow simulations on the full domain structured mesh with flat boundaries, then use the full domain results to inform small regional meshes with high resolution.

The mesh size will be an important consideration for the full domain. As shown by the simulations, a cell size of 50x50x20 meters is adequate for the simulations and the shape of the alluvium zone. Given the size of the alluvium domain, or the full domain which includes the bedrock, the number of mesh nodes will be between 16 and 40 million nodes, requiring PFLOTRAN running in parallel.

The following are numbers based on the JewelSuite™ Mesh exported from the full JewelSuite™ GFM (Section 3, Figure 3-12).

```
Full GFM Domain 33322 x 26498 x 2217 meters
Top Elevation approximately 1300 to 1716 meters
50 m x 50 m x 20 m spacing = 667 x 531 x 111 = 39,313,647 nodes

Alluvium Domain 29200 x 19400 x 1515 meters
Top Elevation approximately 1300 to 1410 meters
50 m x 50 m x 20 m spacing = 585 x 389 x 72 = 16,384,680 nodes
```

The Vorocrust method is promising; it is easy to run and guarantees an optimal, surface conforming, computational mesh for simulations. The controls for spatially variable cell spacing will need to be developed so that control volumes within the mesh are not too large with respect to the simulation that is used. The parameters for these controls are not yet available.

6 Simulations on a Vertical Slice of the GFM

6.1 Verification of Mesh, Model Setup, and Comparison

Here we present results of 8 different geologically representative scenarios to confirm that computations on meshes created from the GFM are valid. First, we show that both FEHM (FEHM, 2020; Zyvoloski et al., 2012) and PFLOTRAN (PFLOTRAN, 2020) porous flow simulators produce results that match analytical solutions. Second, we show that FEHM and PFLOTRAN produce nearly identical results for scenarios that have no simple analytical solutions. Third, we demonstrate that the simulators work well on meshes that are aligned with the simulation coordinate axes and meshes that are aligned with the GFM axes (15.5 degree rotation from the simulation axes, see Figure 5-4). Table 6-1 and Table 6-2 present detailed information on the setup for each of the 8 simulations as well as their material properties. The x-aligned mesh is 9900 m x 350 m x 1500 m. The diagonal mesh shares the same dimensions except that it is rotated by approximately 15.5 degrees. Thus, the diagonal mesh does not have x-min, x-max, y-min, or y-max that match the extent of the grid. For visualization and analytical purposes, results from the diagonal mesh are rotated by 15.5 degrees to align the two sets of output and allow for ease of comparison between the aligned and diagonal meshes.

Table 6-1: Information for the 8 test case scenarios

Scenario	Geologic Test Case	Phase State	Permeability	Flow field	Gravity on?	Top Boundary	Bottom Boundary
1.1	Aligned	Saturated	Isotropic	Upflow	NO	Fixed P	Fixed P
1.2	Aligned	Saturated	Variable	Upflow	NO	Fixed P	Fixed P
1.3	Aligned	Unsaturated	Isotropic	Infiltration	YES	Fixed flux	Fixed sat
1.4	Aligned	Unsaturated	Variable	Infiltration	YES	Fixed flux	Fixed sat
2.1	Diagonal	Saturated	Isotropic	Upflow	NO	Fixed P	Fixed P
2.2	Diagonal	Saturated	Variable	Upflow	NO	Fixed P	Fixed P
2.3	Diagonal	Unsaturated	Isotropic	Infiltration	YES	Fixed flux	Fixed sat
2.4	Diagonal	Unsaturated	Variable	Infiltration	YES	Fixed flux	Fixed sat

Table 6-2: Hydrologic properties for the 4 materials

Rock Case	Permeability (m^2)	Porosity	α (1/m)	n	Residual saturation	Max saturation
Saturated Alluvium	2.65e-12	0.35	NA	NA	NA	NA
Saturated Carbonate	4.80e-15	0.124	NA	NA	NA	NA
Unsaturated Alluvium	2.65e-12	0.35	5.0	2.68	0.01	1.0
Unsaturated Carbonate	4.80e-15	0.124	4.311	1.176	0.053	1.0

6.1.1 Saturated and Unsaturated Runs on the Aligned Mesh

6.1.1.1 Scenario 1.1

The first scenario for the aligned mesh shows that the pressure gradient for an upwelling flow-field is perfectly flat. Gravity is turned off for this scenario so that there is no impact of gravitational potential energy and the flow field will be exactly proportional to the spacing of the constant pressure lines shown in black on Figure 6-1. In Figure 6-1 below, the results are visually identical between FEHM (top) and PFLOTRAN (bottom). The mass flow rate ($\dot{m}$) for this simulation (609 kg/s) is in line with the analytical flow solution, given as

$$\dot{m} = A \cdot \rho \cdot \frac{k}{\mu} \nabla P \qquad \textit{Eq. 1}$$

Assuming A = 400 m^2, ρ = 998.6 kg/m^3, k = 2.65 e^{-12} m^2, μ = 1e^{-3} Pa s, and ∇P= (1.e^5 Pa/1500 m), Eq. 1 yields 6.11 kg/s leaving the top of the model domain. PFLOTRAN gives the same mass flow rate for this problem.

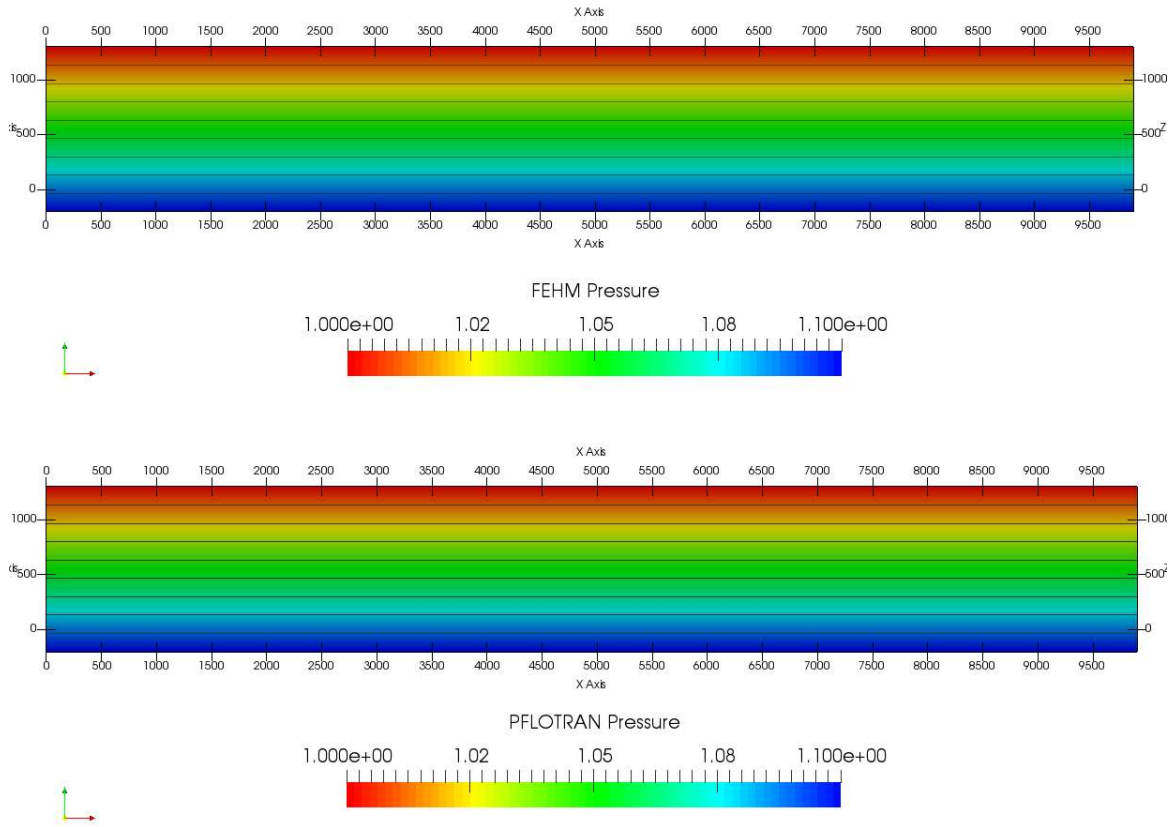

Figure 6-1: Pressure contours for the saturated isotropic permeability run on the aligned mesh.

6.1.1.2 Scenario 1.2

The second scenario for the aligned mesh presents a similar scenario to that of 6.1.1.1. Instead of yielding a perfectly flat pressure gradient for an upwelling flow field, FEHM and PFLOTRAN show that most of the pressure drop occurs primarily in the carbonate (blue) in Figure 6-2, a function of the lower permeability in this unit. Again, FEHM and PFLOTRAN produce visually identical results as shown in Figure 6-3.

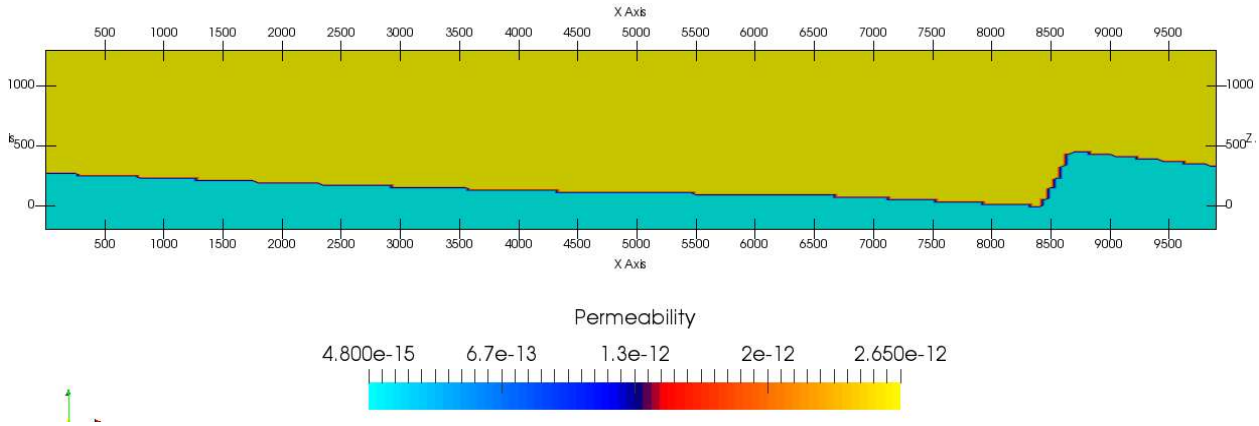

Figure 6-2: Permeability for the aligned mesh in scenario 1.2.

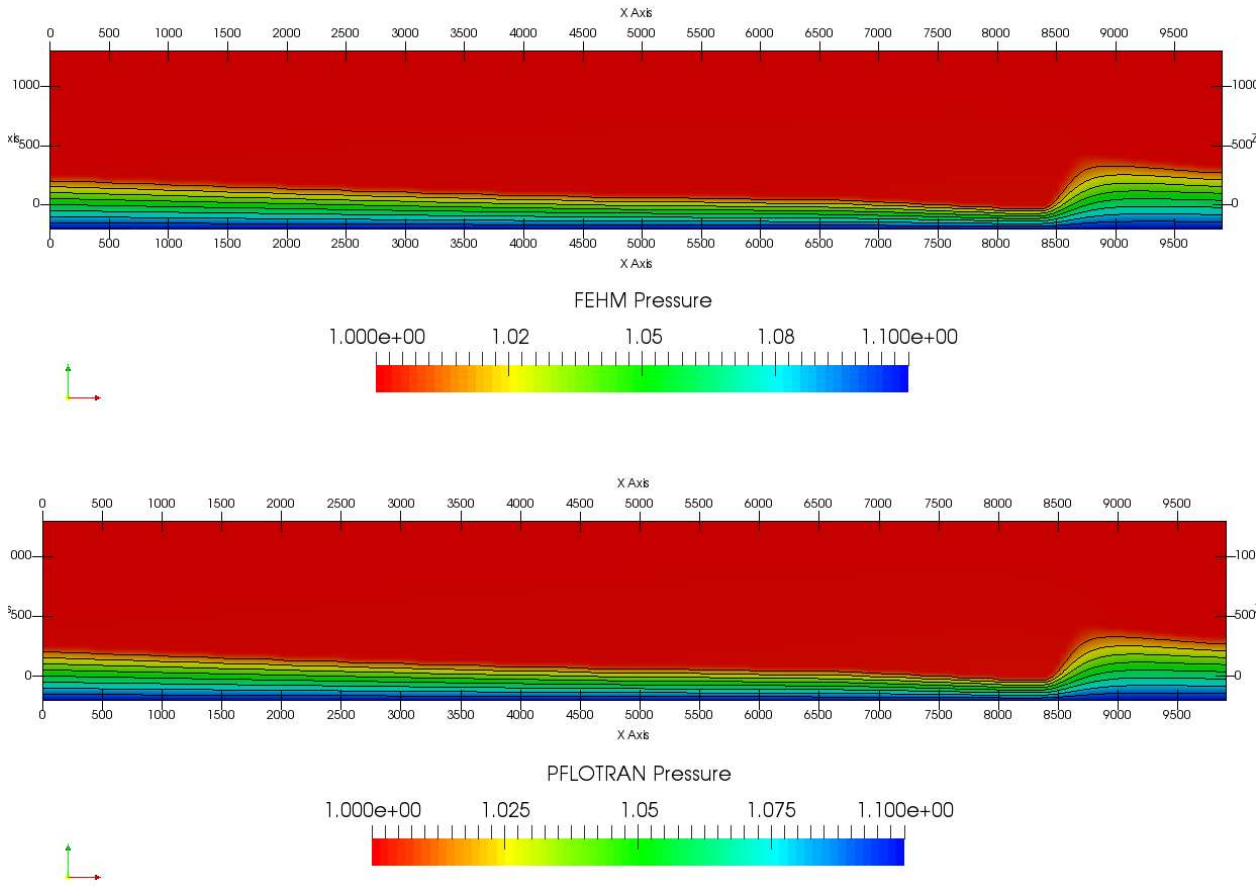

Figure 6-3: Pressure contours for the saturated variable permeability run on the aligned mesh.

6.1.1.3 Scenario 1.3

The third scenario for the aligned mesh presents an unsaturated domain with an isotropic permeability field. The field uses the Santa Fe alluvium properties in Table 6-2. Boundary conditions included a constant infiltration flux at the top of the domain (10 liters/(m^2 year) or 10 mm/yr) and a fixed saturation at the bottom of the domain. Though difficult to see, saturation contours are almost entirely stacked on each other at the very bottom of the mesh, showing no impact of the boundary between the alluvium and the carbonate on the solution. The FEHM and PFLOTRAN results are practically identical in Figure 6-4. (Note the line along the bottom of the PFLOTRAN simulation is an artifact of the ParaView visualization).

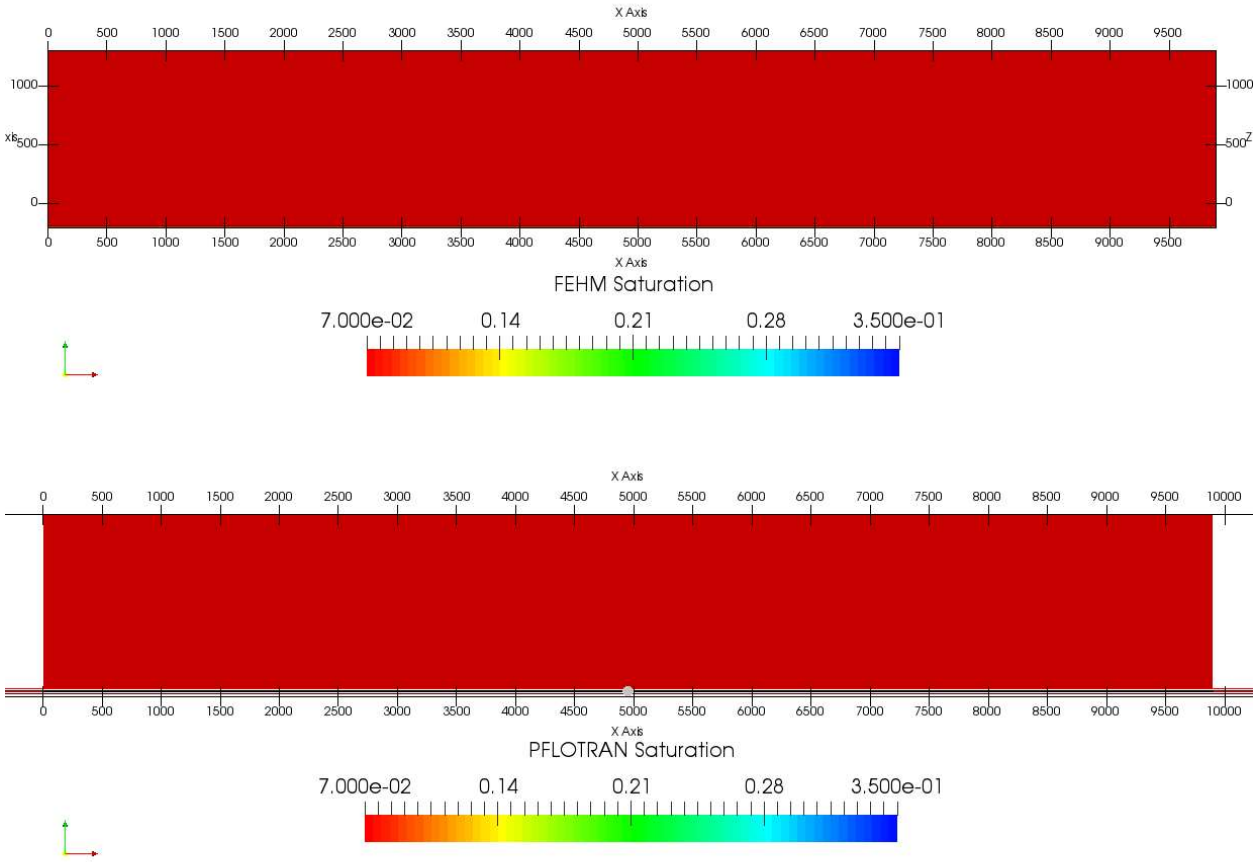

Figure 6-4: Saturation contours for the unsaturated isotropic permeability run on the aligned mesh.

6.1.1.4 Scenario 1.4

The fourth scenario on the aligned mesh presents an unsaturated domain with variable permeability as shown in Figure 6-2. The two materials are assigned the properties detailed in Table 6-2. Boundary conditions included a constant infiltration flux at the top of the domain (10 mm/yr) and a fixed saturation at the bottom of the domain. In Figure 6-5, the FEHM and PFLOTRAN results differ slightly. Nodes directly below the vertical steps in the fault have slightly lower saturation in FEHM than in PFLOTRAN. However, aside from that, saturation contours are very similar between the two codes. Both codes are finding the equilibrium saturation in each unit that permits the applied flux to flow through the domain.

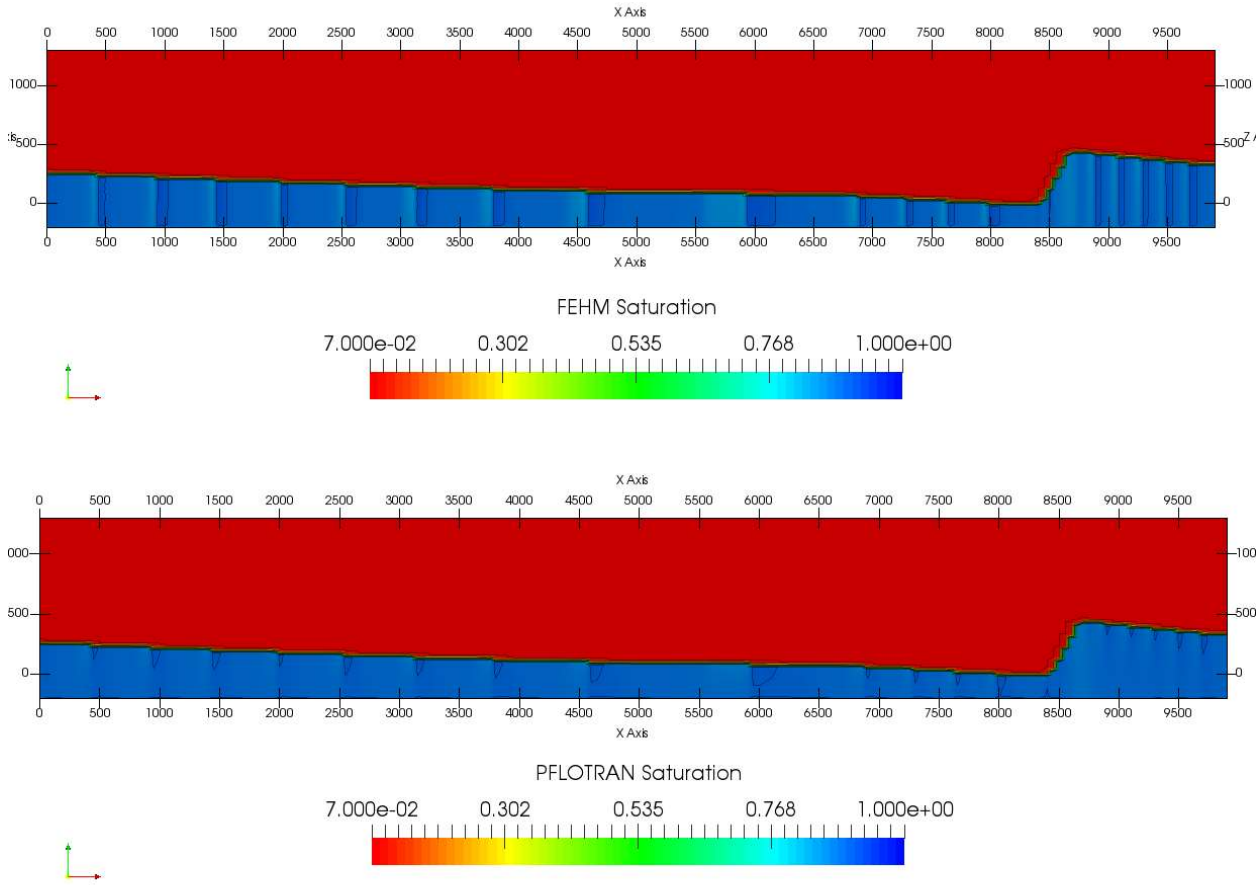

Figure 6-5: Saturation contours for the unsaturated variable permeability run on the aligned mesh.

6.1.2 Saturated and Unsaturated Runs on the Diagonal Mesh

For visual clarity, all images of results in this section have been rotated to align with coordinates following the Deming sub-basin mesh.

6.1.2.1 Scenario 2.1

The first scenario for the diagonal mesh shows that the pressure gradient for an upwelling flow-field is perfectly flat. Gravity is turned off for this scenario so that there is no impact of gravitational potential energy and the flow field will be exactly proportional to the spacing of the constant pressure lines shown in black on Figure 6-6. In Figure 6-6 below, the results are visually identical between FEHM (top) and PFLOTRAN (bottom). However, PFLOTRAN does show one discrepancy in which the flow field is not perfectly flat and is instead at a slight upwards angle from left-to-right. This discrepancy is unique to the saturated isotropic permeability run on the diagonal mesh and could be an artifact of transforming the diagonal mesh in ParaView for visualization.

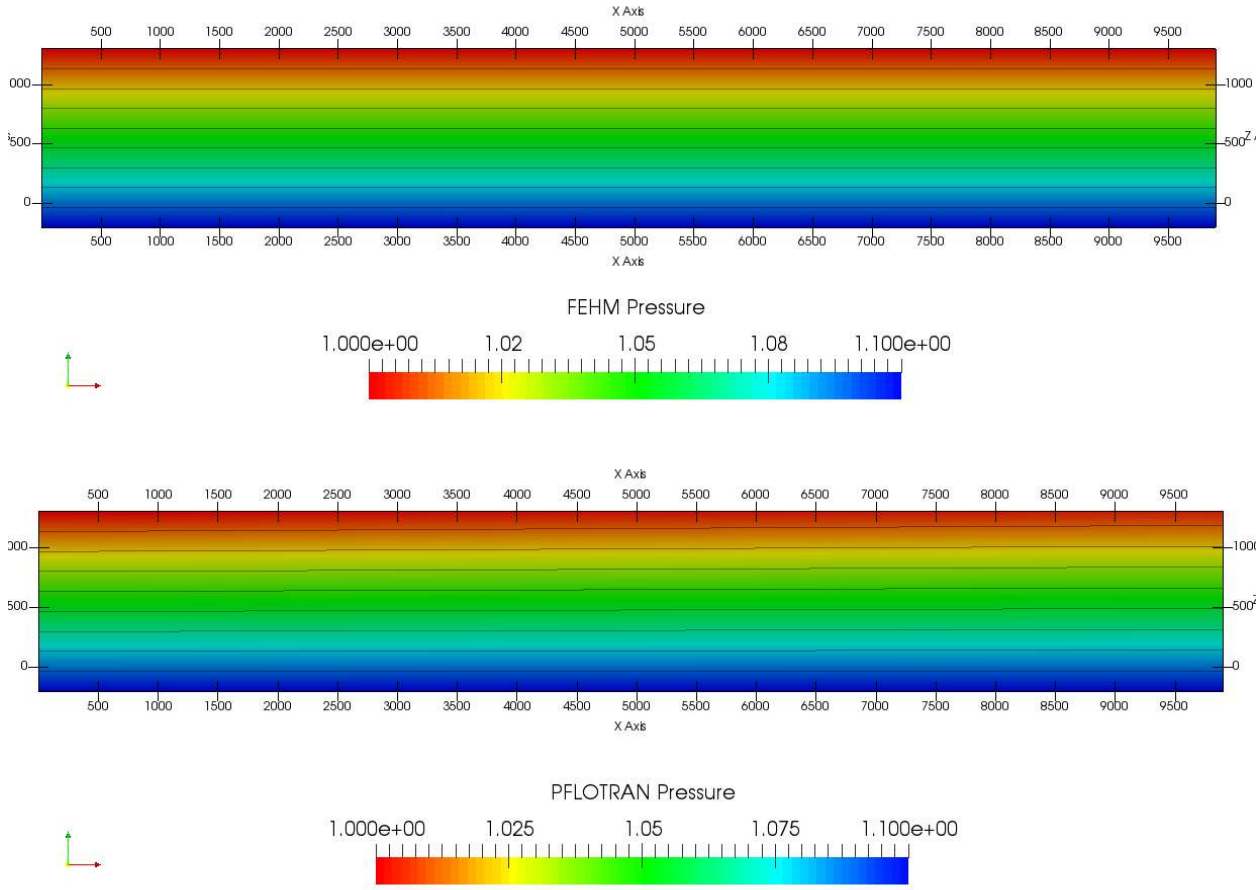

Figure 6-6: Pressure contours for the saturated isotropic permeability run on the diagonal mesh .

6.1.2.2 Scenario 2.2

The second scenario for the diagonal mesh presents a similar scenario to that of 2.1. Instead of yielding a perfectly flat pressure gradient for an upwelling flow field, FEHM and PFLOTRAN show that most of the pressure drop occurs in the low permeability carbonate with very little pressure drop across the high permeability alluvium. Again, FEHM and PFLOTRAN produce visually identical results visible in Figure 6-7.

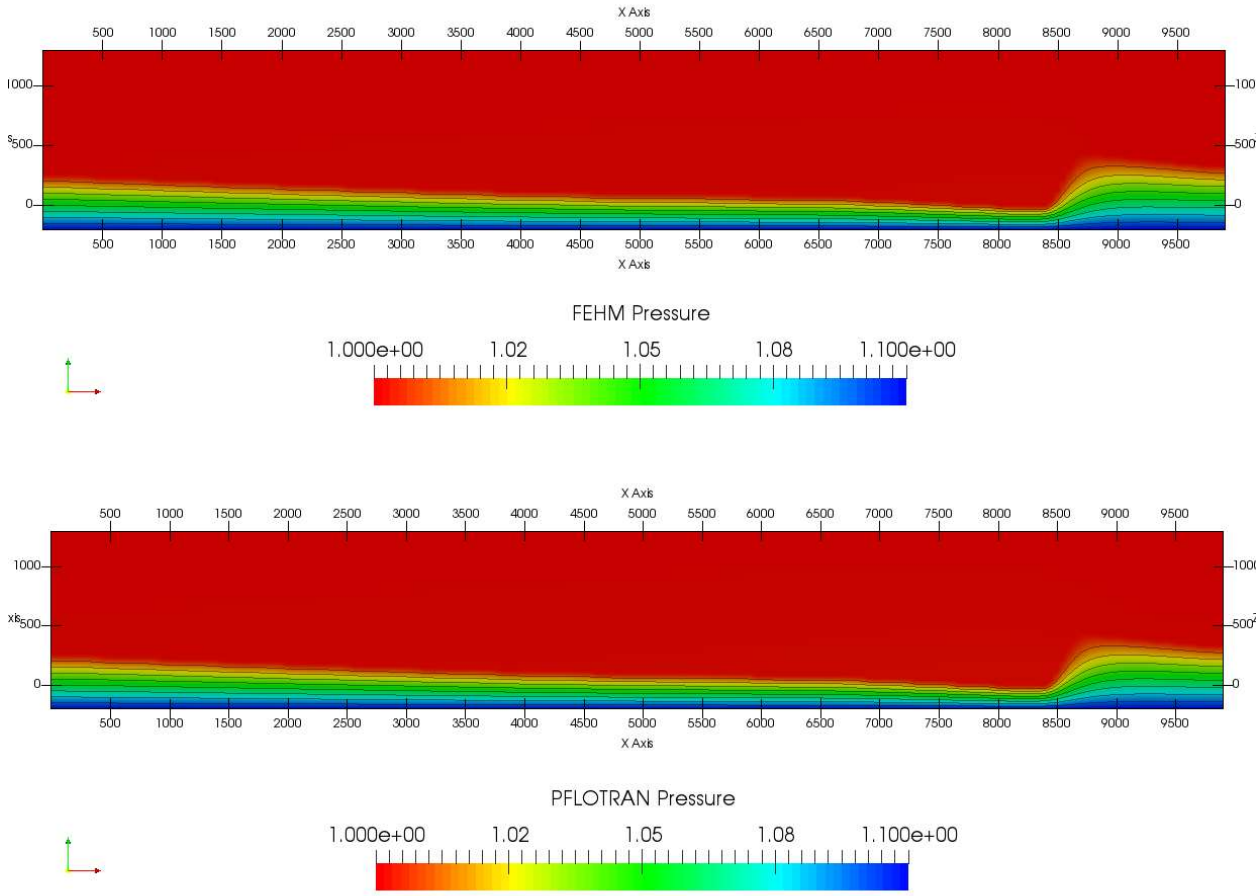

Figure 6-7: Pressure contours for the saturated variable permeability run on the diagonal mesh.

6.1.2.3 Scenario 2.3

The third scenario for the diagonal mesh presents an unsaturated domain with an isotropic permeability field. The field uses the Santa Fe alluvium properties in Table 6-2. Boundary conditions included a constant infiltration flux of 10 mm/yr at the top of the domain and a fixed saturation at the bottom of the domain. Though difficult to see, saturation contours are almost entirely stacked on each other at the very bottom of the mesh, showing no impact of the mesh on the solution. The FEHM and PFLOTRAN results are practically identical in Figure 6-8.

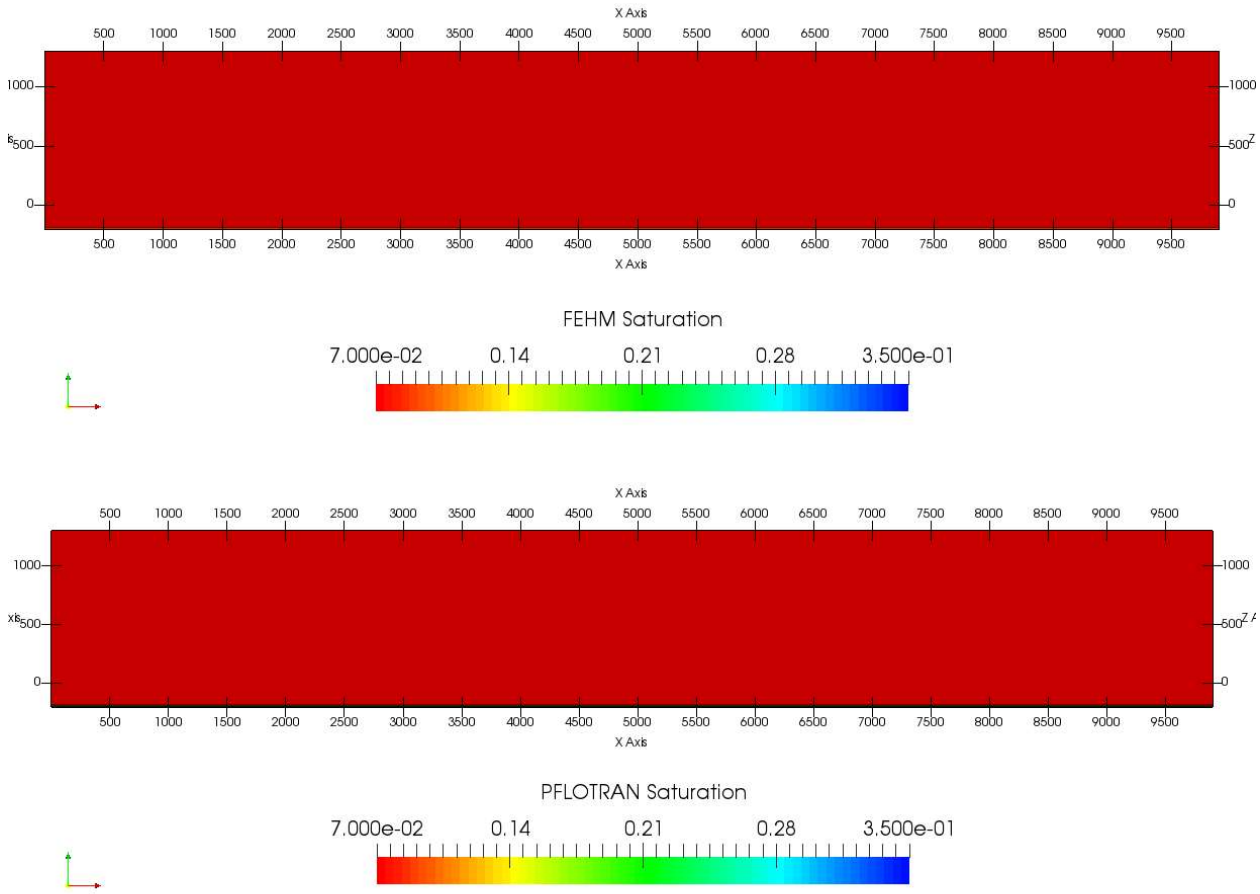

Figure 6-8: Saturation contours for the unsaturated isotropic permeability run on the diagonal mesh.

6.1.2.4 Scenario 2.4

The fourth scenario on the diagonal mesh presents an unsaturated domain with variable permeability as shown in Figure 6-9. The two materials are assigned the properties detailed in Table 6-2. Boundary conditions included a constant infiltration flux of 10 mm/yr at the top of the domain and a fixed saturation at the bottom of the domain. In Figure 6-9, the FEHM and PFLOTRAN results differ slightly. Nodes directly below the vertical steps in the fault have slightly lower saturation in FEHM than in PFLOTRAN. However, aside from that, saturation contours are very similar between the two codes.

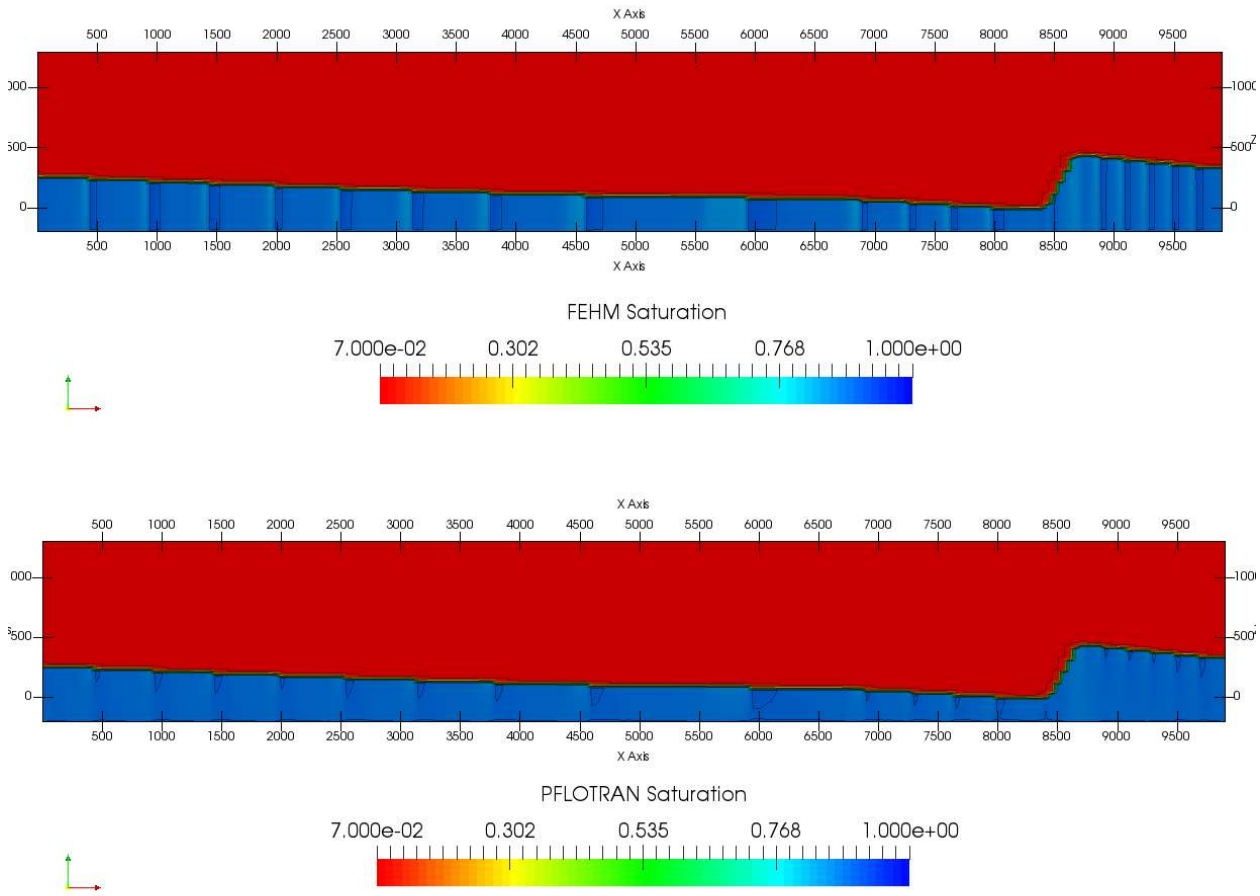

Figure 6-9: Saturation contours for the unsaturated variable permeability run on the diagonal mesh.

Table 6-3: Diagnostic output information for the 8 test case scenarios

Scenario	Geologic Test Case	Permeability Structure	Phase State	Steady-state flowrate (kg/s) **FEHM**	Steady-state flowrate (kg/s) **PFLOTRAN**	Final Simulation Time (yrs)	Model Depth (m)
1.1	Aligned	isotropic	Saturated	6.09E+02	6.09E+02	1000.	1500.
1.2	Aligned	variable	Saturated	5.10E+00	5.10E+00	1000.	1500.
1.3	Aligned	isotropic	Unsaturated	1.1E+00	1.1E+00	10000.	1500.
1.4	Aligned	variable	Unsaturated	1.1E+00	1.1E+00	10000.	1500.
2.1	Diagonal	isotropic	Saturated	6.09E+02	6.09E+02	1000.	1500.
2.2	Diagonal	variable	Saturated	5.10E+00	5.10E+00	1000.	1500.
2.3	Diagonal	isotropic	Unsaturated	1.1E+00	1.1E+00	10000.	1500.
2.4	Diagonal	variable	Unsaturated	1.1E+00	1.1E+00	10000.	1500.

6.2 Numerical Dispersion within the Aligned and Diagonal Meshes in FEHM and PFLOTRAN

The second stage of mesh verification is to compare numerical dispersion of tracer in both FEHM and PFLOTRAN. All simulations in this section have both the coefficient of dispersion (α) and the molecular diffusion set to zero. Thus, any spreading of the initial tracer along the flow path is an artifact of numerical dispersion. Typically, numerical dispersion is a function of mesh spacing and can be approximated as ½ the mesh spacing in the direction of flow (Zyvoloski and Vesselinov, 2006). Because the meshes used by FEHM and PFLOTRAN are identical, we would expect nearly identical numerical dispersion behavior. In total, we present comparisons of five simulations in this section, with both diagonal and aligned tetrahedral (converted to Voronoi cells using LaGriT) meshes compared to the aligned Vorocrust mesh shown in Figure 5-5. Each simulation has two constant pressure boundaries: 4 MPa at the left boundary (x = 0) and 2 MPa at the right boundary (x = 9900). Gravity is turned off for these simulations to simplify the pressure boundaries and the domain is fully saturated. After running the model to steady-state (2.1e2 kg/s water in/out) we inject 1.75e7 mol of tracer into the Voronoi volume with a central node located at x=3000 m, y=240 m, z=200 m. Permeability in the simulation domain on two slices taken at constant y = 250 m and x = 8650 m, respectively, is shown in Figure 6-10. The permeability contrast between the blue carbonate and the yellow alluvium causes water and tracer flowing from left to right to be pushed up and over the carbonate rise (fault) located at x = 8500 m.

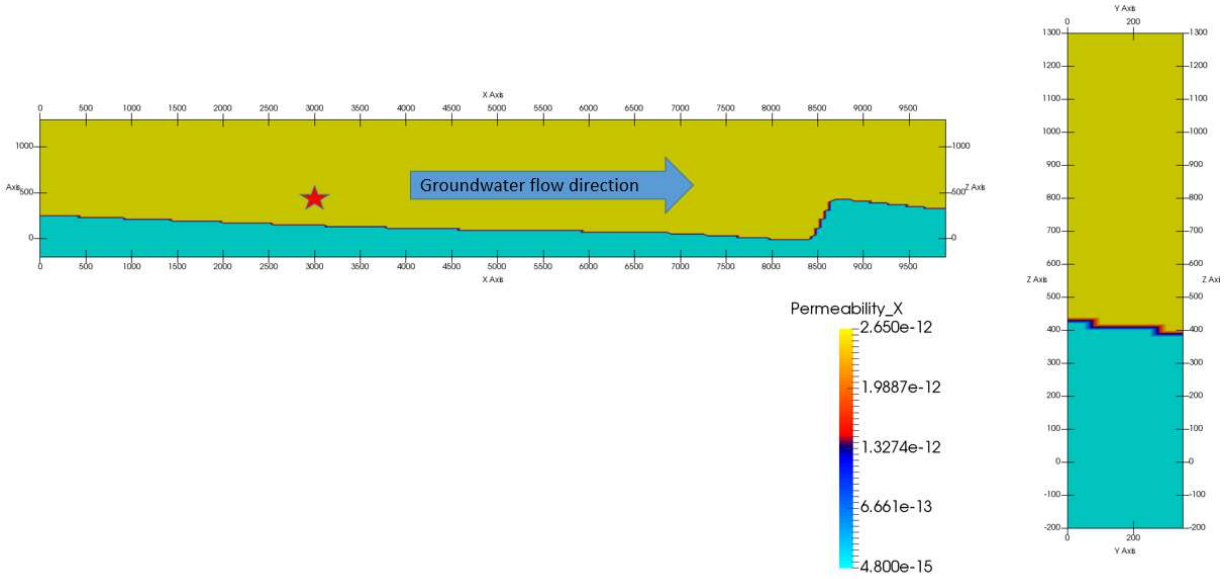

Figure 6-10: Permeability of materials shown in the below slices. Alluvium (yellow) at 2.65e-12 and Carbonate (blue) at 4.8e-15. The red star indicates the tracer release location and the groundwater flow direction is indicated by the blue arrow.

6.2.1 Tracer Dispersion at 20yrs

Figure 6-11 and Figure 6-12 show slices at 20 years taken at constant y = 250 m and x = 8650 m, respectively, along both the x- and y-axes. Figure 6-11 and Figure 6-12 illustrate the differences

in numerical dispersion of tracer between FEHM and PFLOTRAN, where PFLOTRAN seems to have slightly higher numerical dispersion with a longer downstream tail at 20 years.

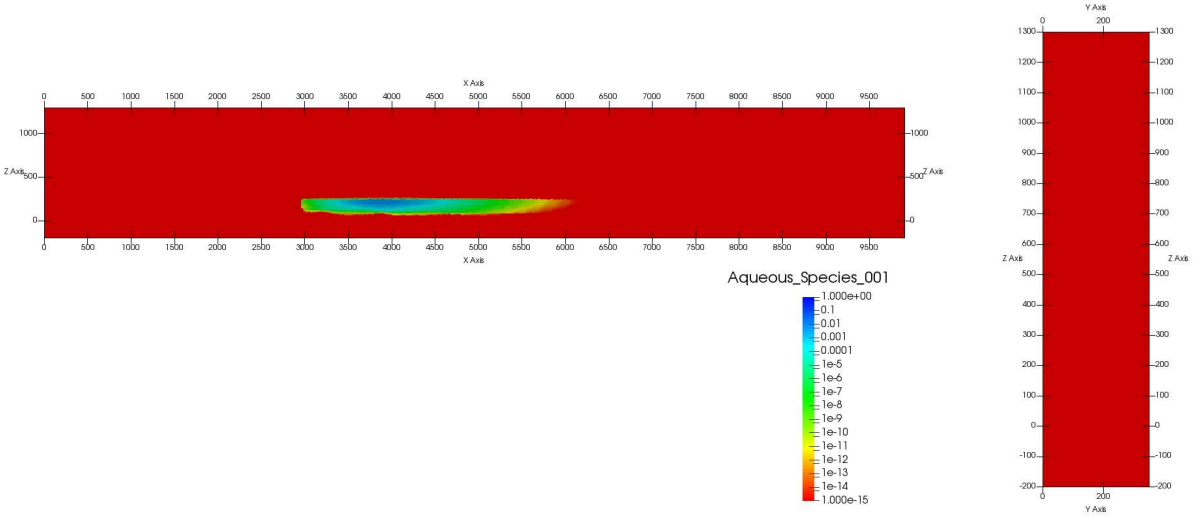

Figure 6-11: Tracer dispersion in FEHM simulation at 20 yrs. Slice (left) taken at y = 250 m. Slice (right) taken at x = 8650 m.

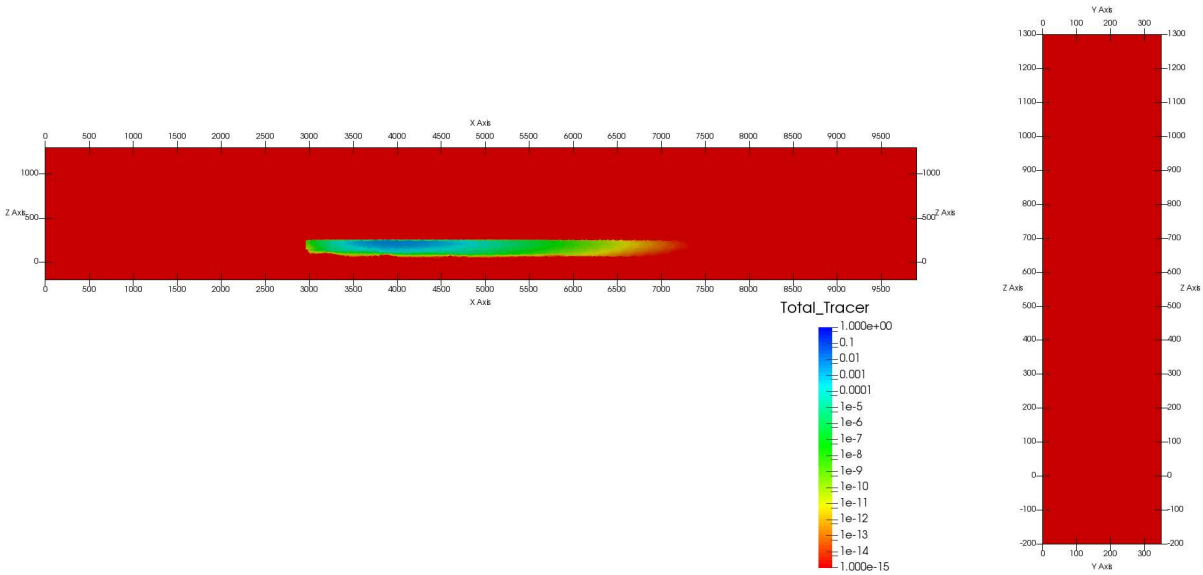

Figure 6-12: Tracer dispersion in PFLOTRAN simulation at 20 yrs. Slice (left) taken at y = 250 m. Slice (right) taken at x = 8650 m.

6.2.2 Tracer dispersion at 100yrs

Figure 6-13 and Figure 6-14 show slices at 100 years taken at constant y = 250 m and x = 8650 m, respectively, along both the x- and y-axes. Figure 6-13 and Figure 6-14 again illustrate the differences in numerical dispersion of tracer between FEHM and PFLOTRAN, where PFLOTRAN

seems to have slightly higher numerical dispersion with higher concentrations having moved more quickly downstream at 100 years.

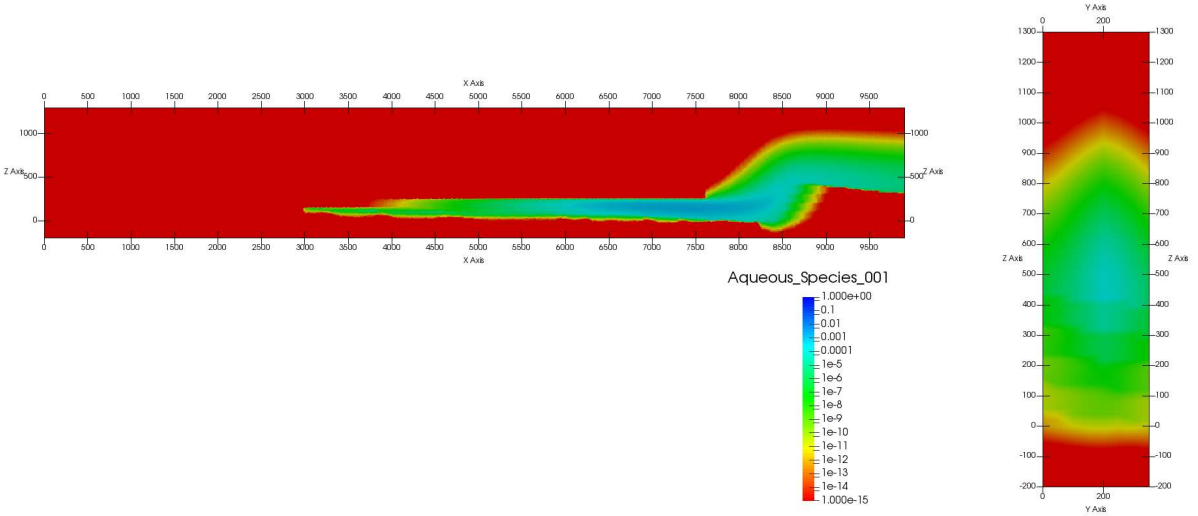

Figure 6-13: Tracer dispersion in FEHM simulation at 100 yrs. Slice (left) taken at y = 250 m. Slice (right) taken at x = 8650 m.

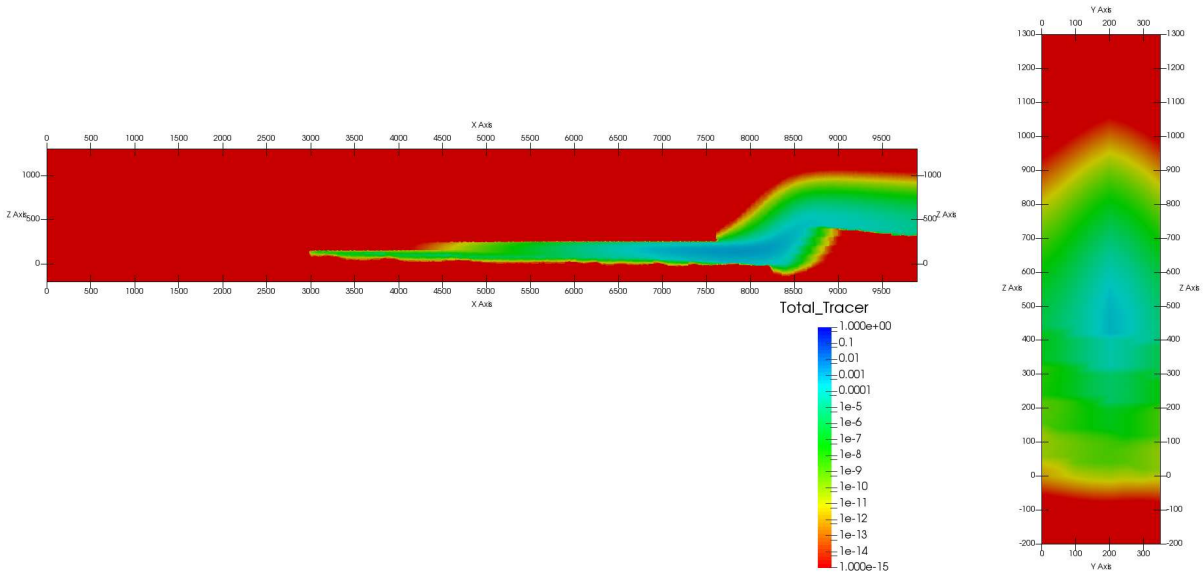

Figure 6-14: Tracer dispersion in PFLOTRAN simulation at 100 yrs. Slice (left) taken at y = 250 m. Slice (right) taken at x = 8650 m.

Figure 6-15 illustrates the total amount of tracer in the model over time for the five simulations in FEHM and PFLOTRAN. FEHM and PFLOTRAN are clearly producing nearly the same mass transfer through the system when using the meshes created by LaGriT. The Vorocrust mesh is showing faster flow through the system, which may be related to larger mesh elements leading to higher numerical dispersion.

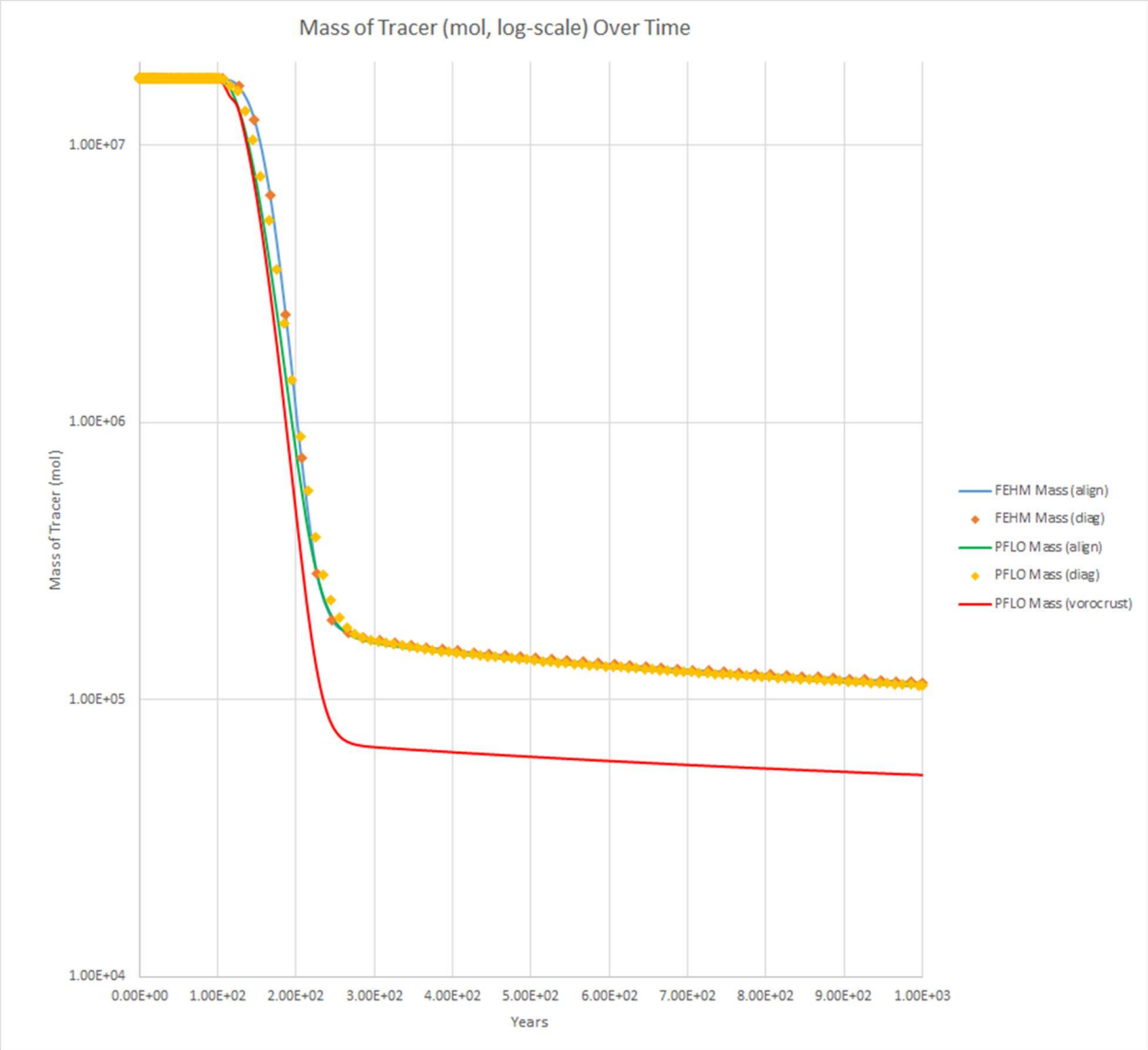

Figure 6-15: Tracer mass versus time in the domain.

6.3 Implantation of a flowing water table in FEHM

Here we describe the process for creating a flowing water table in FEHM. The location of the water table is based on field data from the Deming sub-basin and for the example presented, is assumed to be at a constant elevation of 800 m (see Section 5.4.6). FEHM is used to initialize the mesh with a saturated region such that the nodes at an elevation of 800 m are fully saturated with a pressure of 0.16 MPa. The background infiltration flux for the initialization run is 1 mm/yr, and the simulation runs for 100 years for pressures in the saturated region to equilibrate in the domain. The infiltration flux was set to 1 mm/yr to avoid raising the water table during the 1000 yrs of simulation time. For the initialization, the domain has sealed lateral and bottom boundaries. The output from this simulation is used as an initial condition for a simulation with a fixed mass flow rate of 1.0 kg/s distributed relative to permeability and cell area over the x=0 plane at and below the water table (Figure 6-16). Two sides of the domain

(y=0 and y=350 m) are no-flow, and the x=9900 m boundary is fixed to the hydrostatic pressure generated in the initialization simulation. Infiltration continues at 1 mm/yr, thus the total flux through the system at steady state is 1.1 kg/s. The domain uses the same varied permeability as shown in Figure 6-10. Differences in tracer transport at 1000 yrs for the diagonal mesh (top) and aligned mesh (bottom) for this simulation at steady state are shown in Figure 6-17. The diagonal mesh has noticeably more dispersion with a wider plume. This is expected due to effects of the mesh being out of alignment with the simulation coordinate axes (Zyvoloski and Vesselinov, 2006).

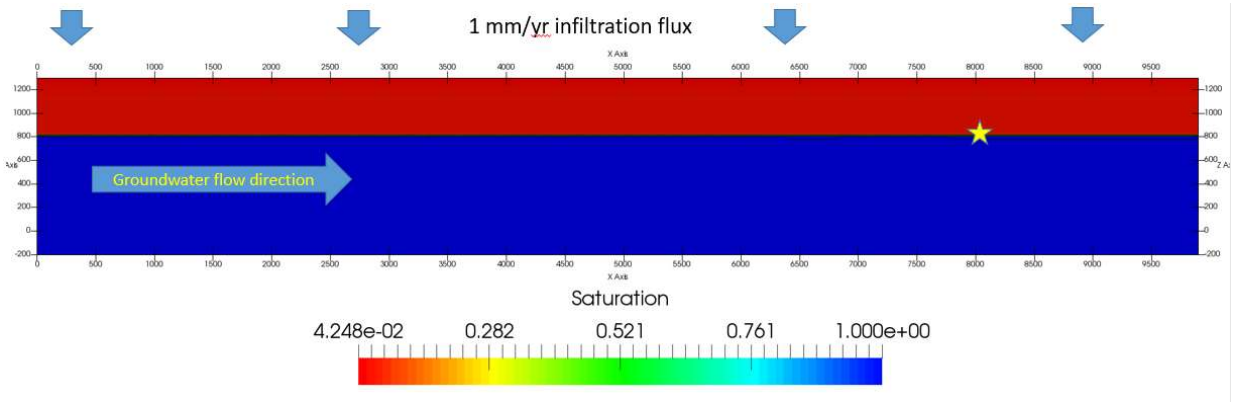

Figure 6-16: Water table simulation using FEHM. The yellow star is the tracer release location.

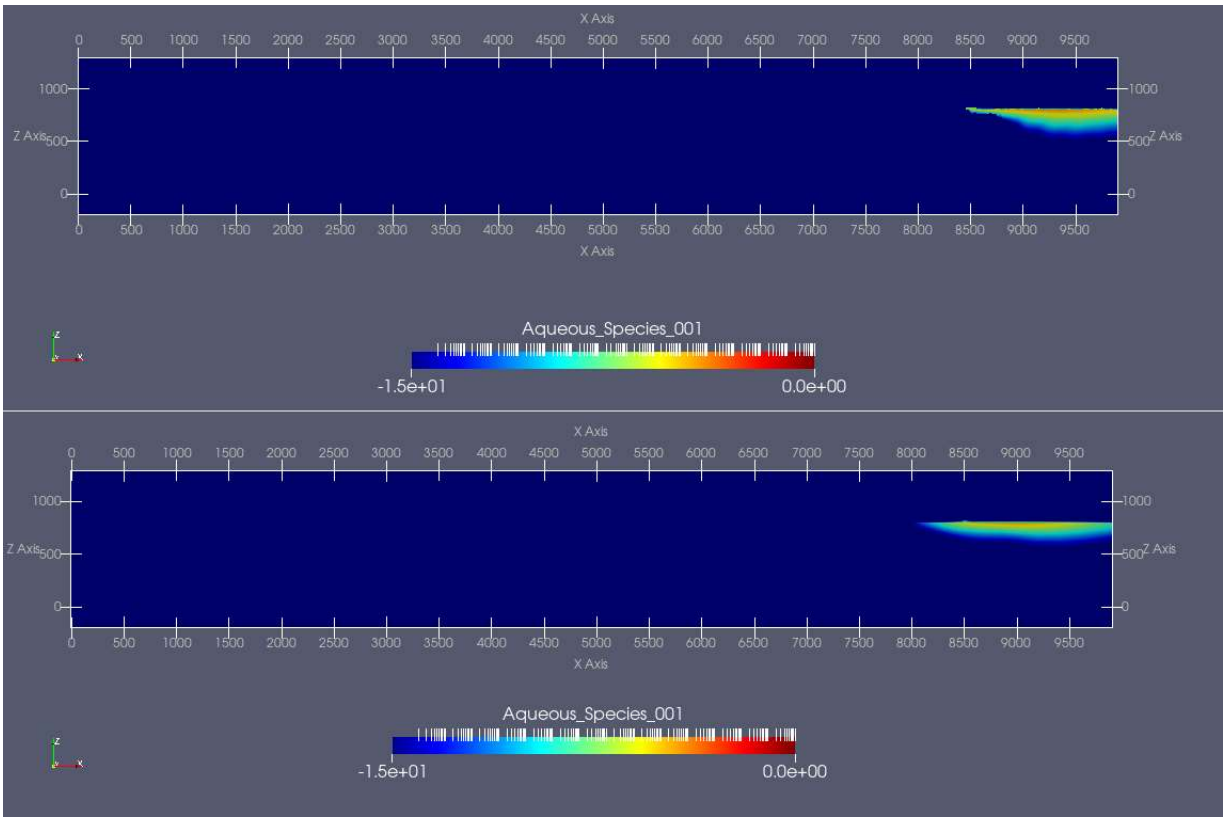

Figure 6-17: Diagonal mesh (top) and aligned mesh (bottom) showing numerical dispersion in FEHM at 1000 yrs after tracer release.

7 Discussion

7.1 Distribution of alluvium thickness

Geologic media under consideration as repositories such as crystalline, argillite and bedded salt remain fairly constant in thickness across the prospect and repository scales. In contrast, the geometry and thickness of sediments in an alluvial basin can vary over relatively short distances (i.e., km scale) because the basins are often fault-controlled and asymmetric. Therefore, alluvial thickness, defined as the vertical distance between the ground surface and the top of bedrock, is one of the most important criteria for identifying potential repositories in alluvial basins. Construction of a comprehensive GFM facilitates production of an alluvial thickness map, which may in turn contribute to high-grading potential repository locations.

Where bedrock is present on the surface the alluvium thickness is zero. In Figure 7-1Figure 6-17 the top of alluvium is transparent, thus revealing the elevation of the top of bedrock. Note the two semi-circular depocenters in blue, located in the hanging wall blocks of the Central and Eastern Faults. This is where the basin-fill sediments are the thickest. Also note the bright orange outcroppings of bedrock where alluvium is absent.

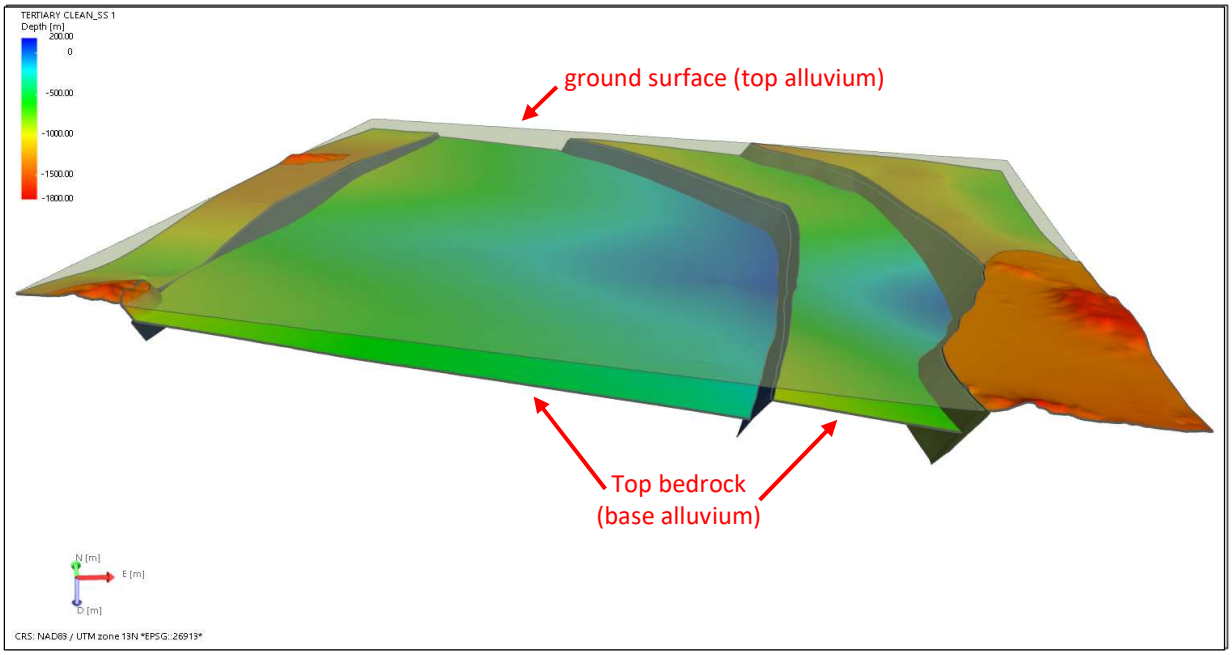

Figure 7-1: Geologic framework model of the Deming sub-basin showing the two surfaces (ground surface and top bedrock) used to create the alluvial sediment thickness map. Color indicates true vertical depth sub-sea. Note two depocenters (blue) and bedrock outcrop (orange).

The alluvium thickness is calculated in the JewelSuite™ workflow as the vertical distance between the two surfaces where both surfaces are present. Those values are then displayed as a contoured thickness map (Figure 7-2b), referred to as an interval isopach map (Tearpock and Bischke, 1991). Repository siting must consider both alluvium thickness and proximity to faults. The isopach map is a valuable source of information that can be used to ensure adequate

geologic buffer (vertical and lateral) and safe distance from faults. If the input data and workflow are of sufficient quality, the GFM can provide detail of alluvium thickness and geometry beyond the resolution of surface geophysical surveys (Figure 7-2).

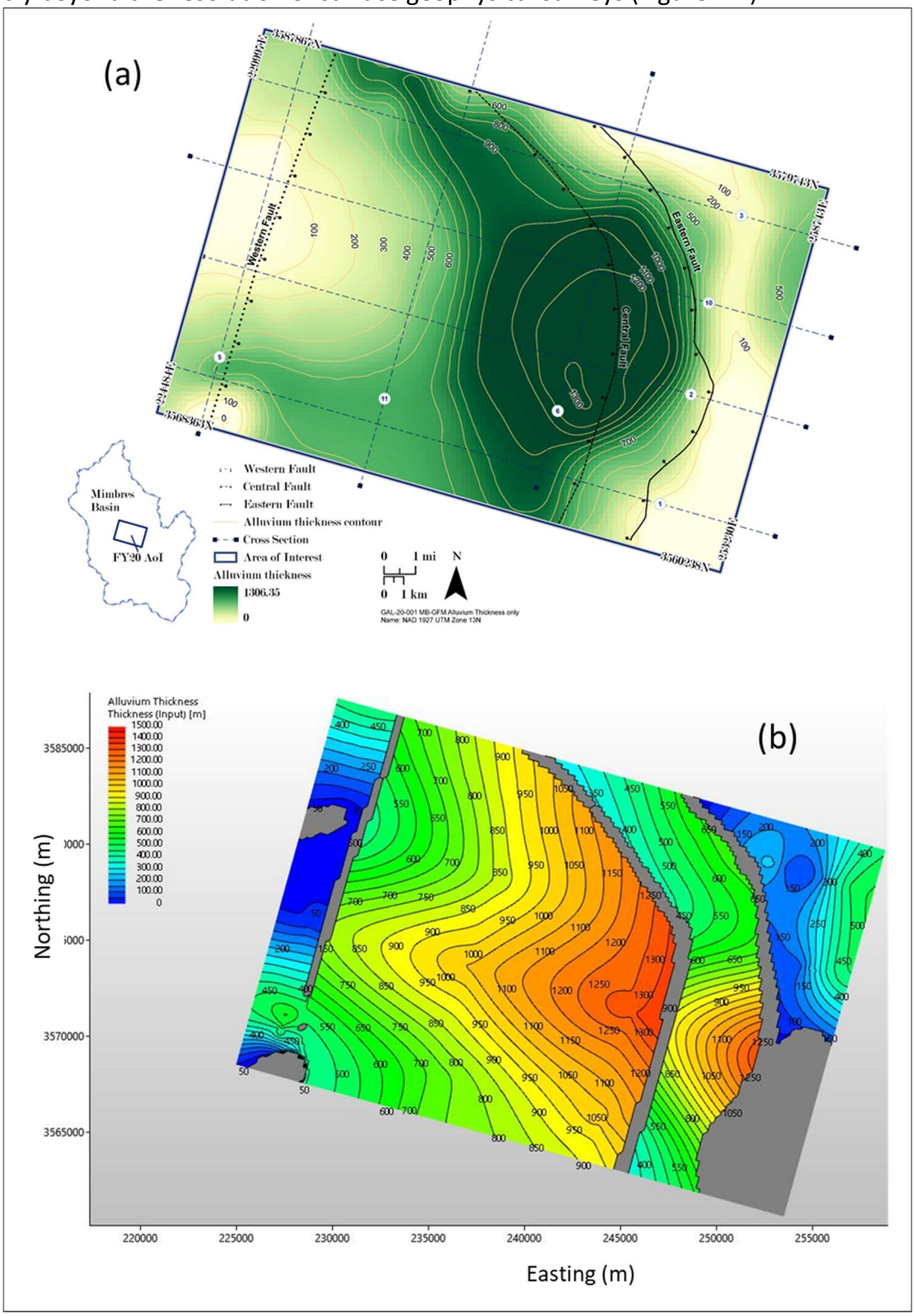

Figure 7-2: Maps of alluvial sediment thickness for the Deming sub-basin derived from (a) gravity surveys (Heywood, 2002) and (b) the GFM from this study. Contour intervals are 100 m.

7.2 Subsurface characterization with facies and property modeling

Facies modeling in JewelSuite™ produces a cross section that closely resembles the interpreted alluvial section (Figure 7-3). The complex geometries of the Gila alluvial fan deposits are captured with remarkable detail in the hanging wall block of the normal faults, including the repeated section above the Central Fault. The Mimbres alluvial fan blankets the top of the section and the stratigraphy is mostly correct except for several isolated cells at the margins of the fluvial deposits. The thin tabular lacustrine sediments, however, are somewhat discontinuous and interbedded with fluvial sediments. This is likely due to the relatively large vertical cell dimensions, which can be remedied by applying a finer resolution grid to a smaller volume of interest. Overall, the method shows promise for expansion into 3D with more extensive subsurface datasets.

The geologic medium surrounding a repository must be properly characterized to model the flow and transport of radionuclides that may escape from the engineered barrier system (EBS). Facies and property modeling within a GFM such as JewelSuite™ can provide insight into the 3D distribution of porosity, permeability and other rock and fluid properties at many scales. This is illustrated with an example of horizontal permeability slices at varying depths in the basin (Figure 7-4). In this 3-layered system, permeability deceases as a function of depth (increasing *k-layer, k*=50 m height). Note also how the basin size and geometry change with depth and are strongly influenced by the Eastern and Central Faults. Similar maps and analyses generated from the GFM are potentially valuable resources for site evaluation and safety assessment but will require a high density of subsurface sampling to properly characterize basin complexity.

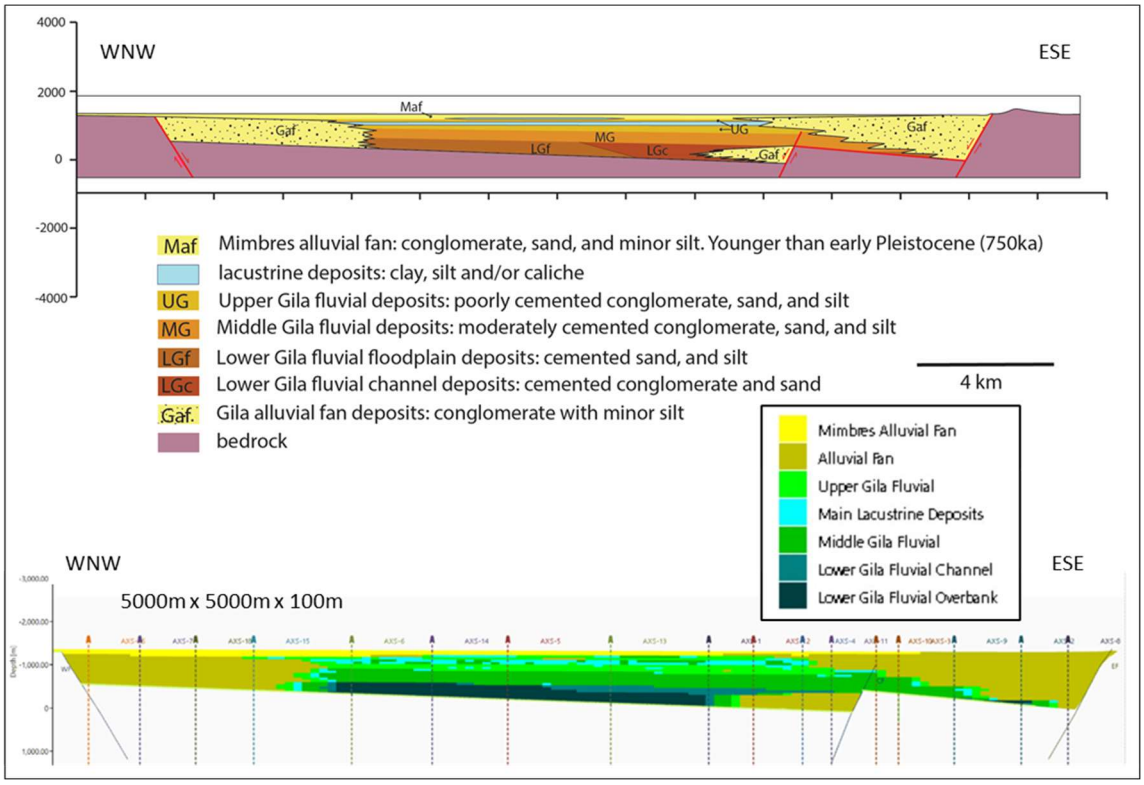

Figure 7-3: Interpreted cross-section of alluvial lithofacies (above) with results of facies modeling (below).

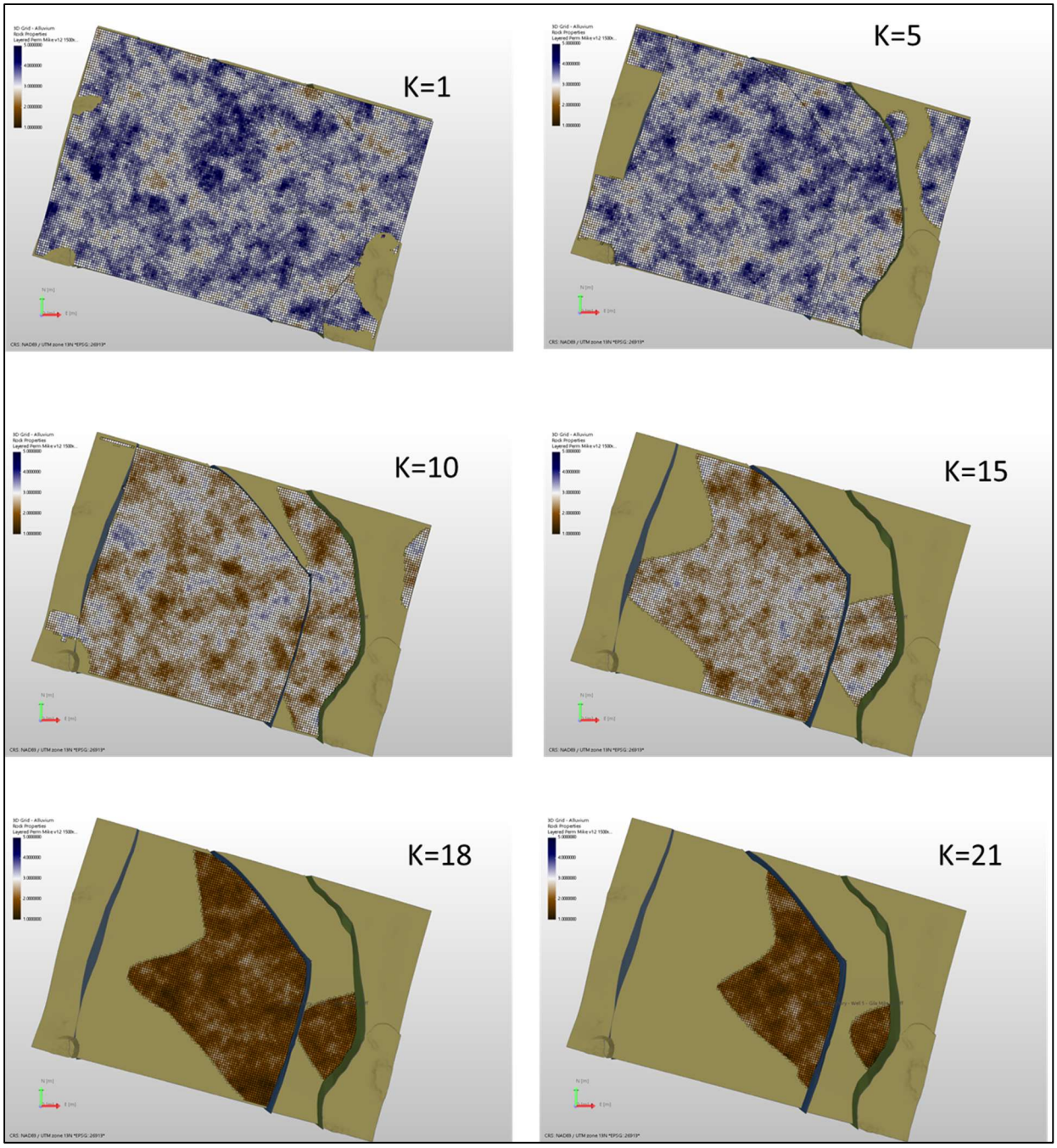

Figure 7-4: Horizontal slices of permeability from model PERM-3L-V1 taken at various depths (k-layers, where each k-layer has a vertical thickness of 50 meters).

7.3 Vertical heterogeneity of physical properties

Physical properties of alluvium are highly variable due to the many basin-fill lithofacies and their complex distribution. Interfingering conglomerates and siltstones at the meter scale are not uncommon, resulting in a highly heterogeneous vertical distribution of porosity and

permeability. This heterogeneity can be approximated with stochastic modeling so long as grid cell size and vertical variogram range are appropriately selected and matched to the scale of observation. As an example, we provide results from Sequential Gaussian Simulation (SGS) models of porosity for the single facies of alluvium (undifferentiated) where the horizontal variogram ranges remain constant (3000 m and 1500 m) and the vertical variogram range increases progressively from 50 m to 500 m. Recalling that the range is the distance between cells above which there is no correlation in property values, the degree of horizontal anisotropy in porosity decreases with increasing vertical range (Figure 7-5). With a vertical range of 50 m the porosity appears as thin horizontal bands (more anisotropic), whereas at a range of 500 m the clusters of high and low porosity resemble large, nearly circular patches (more isotropic).

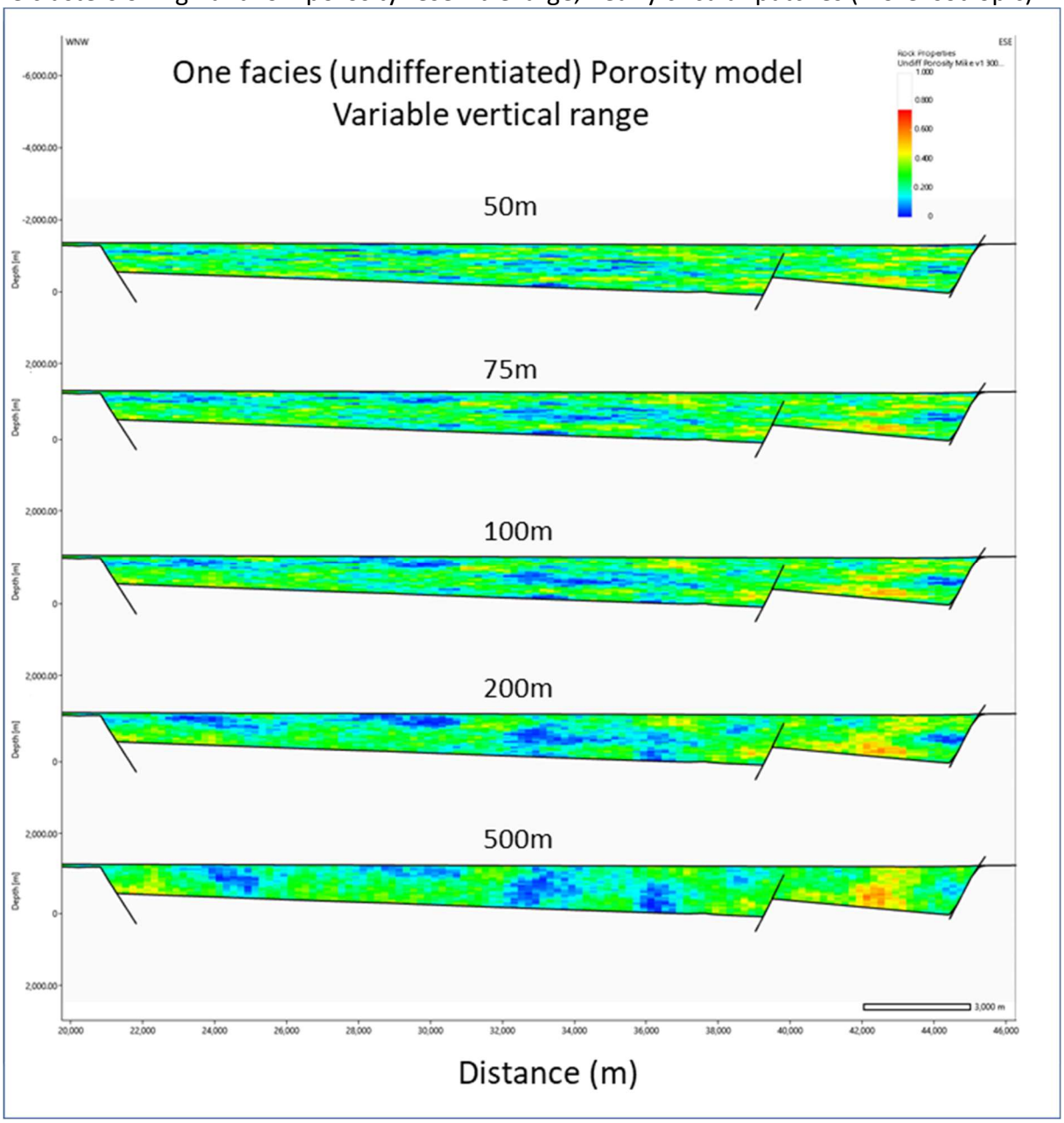

Figure 7-5: Cross sections of porosity for undifferentiated alluvium with constant horizontal ranges (3000 m, 1500 m) and variable vertical ranges assigned to SGS model variogram parameters.

The thin, horizontally elongated bands of porosity for model results at 50–75 m vertical ranges most likely represent the expected lenticular distribution of porosity, which in turn is the product of the layered stratigraphy. However, the sub-basin scale grid has a vertical dimension of 50 m and thus cannot capture the variability in physical properties at the prospect or repository scales. A much finer grid is required to properly characterize and model the alluvial lithofacies at these scales.

7.4 Way forward with computational modeling

Computational meshes created from a slice of the Deming sub-basin GFM have been shown to correctly propagate numerical solutions using the FEHM porous flow simulator for cases of saturated and unsaturated flow with isotropic and heterogeneous permeability distributions. Further, PFLOTRAN has been shown to give nearly identical results for both saturated and unsaturated test problems. Numerical dispersion in both FEHM and PFLOTRAN is consistent using Voronoi conforming meshes created with LaGriT, although dispersion is slightly higher in PFLOTRAN. A single Vorocrust mesh run for the same numerical dispersion problem shows much higher dispersion; however, this is likely due to the larger mesh spacing in the Vorocrust mesh.

The test cases presented in this section show that we are prepared to expand calculations to larger, more complex domains including heterogeneous distributions of permeability such as those generated in the GFM by stochastic modeling. Moving forward, plans call for increased testing of Vorocrust meshes using mesh spacing similar to LaGriT generated meshes so more complete comparisons can be made. Further, we recommend comparing non-dispersive particle tracking to advection/dispersion solutions to better understand the impacts of numerical dispersion on complex domains.

8 Acknowledgements

We would like to thank Florie Caporuscio and Kirsten Sauer for reviewing internal LANL drafts of the report. We are grateful to Sander de Jong of Baker Hughes for providing solutions and insights for our JewelSuite™ modeling efforts. We would also like to acknowledge the generosity of Baker Hughes for providing the team with additional temporary licenses during the remote work phase imposed by COVID-19.

9 References

Abdelkader, A., Bajaj, C., Ebeida, M. S., Mahmoud, A. H., Mitchell, S. A., Owens, J. D. and Rushdi, A. A., 2020, VoroCrust: Voronoi Meshing Without Clipping: ACM Transactions on Graphics, v. 39, p. 1-16, https://doi.org/10.1145/3337680

Anderson, T. W., 1995. Summary of the Southwest Alluvial Basins, Regional Aquifer-System Analysis, south-central Arizona and parts of adjacent states. Professional Paper 1406-A. 44 p. https://pubs.er.usgs.gov/publication/pp1406A

Baker Hughes, 2020, JewelSuite™ 10 Subsurface Modeling User Manual, Delft, The Netherlands, 2324 p.

Belcher, W.R., Elliott, P.E., and Geldon, A.L., 2001. Hydraulic-property estimates for use with a transient ground-water flow model for the Death Valley regional ground-water flow system, Nevada and California: U.S. Geological Survey Water-Resources Investigations Report 2001–4210, 28 p. https://pubs.usgs.gov/wri/wri014210/

Brooks., L.E., 2017, Groundwater Model of the Great Basin Carbonate and Alluvial Aquifer System Version 3.0: Incorporating Revisions in Southwestern Utah and East Central Nevada: US Geological Survey Scientific Investigations Report 2017-5072, 92 p.

Eyal, Y., Bruner, I., Cadan, G., Enzel, Y. and Landa, E., 2002, High-resolution seismic study of the Nahal Darga fan-delta, Dead Sea, Israel, with the aim to relate the surface and subsurface tectonic structures: EGU Stephan Mueller Special Publication Series, v. 2, p. 21-33.

FEHM (2020), https://fehm.lanl.gov/, last accessed July 23, 2020.

Fetter, 1999, Contaminant Hydrogeology, 2nd edition, Prentice Hall, New Jersey, 500p.

Finch, S.T. Jr., McCoy, A. and Melis, E., 2008, Geologic controls on ground-water flow in the Mimbres Basin, southwestern New Mexico in Geology of the Gila Wilderness-Silver City area, New Mexico Geological Society Guidebook, 59th Field Conference, p. 1889-198.

Gawthorpe, R.L. and Leeder, M.R., 2000, Tectono-sedimentary evolution of active extensional basins: Basin Research, v. 12, p. 195-218.

GDACC, 2018, Avis 7.5 Minute Quad 32105, 10M Enhanced DEM, 2005, DEM GeoTIFF: New Mexico Geospatial Data Acquisition Coordination Committee, Albuquerque, New Mexico.

Geologic Map of New Mexico, 2003, New Mexico Bureau of Geology and Mineral Resources in cooperation with the U.S. Geological Survey (scale: 1:500,000).

Gross, M., Bussod, G., Gable, C.W., Kelley, R., Lavadie-Bulnes, A., Milazzo, D., Miller, E., Miller, T.A., Roback, R., Stauffer, P.H., Swanson, E. and Perry, F., 2019, Progress report on the development of a geologic framework model capability to support GDSA, Prepared for the U.S. Department of Energy Spent Fuel and Waste Disposition, LA-UR-19-27943.

Hanson, R.T., McLean, J.S. and Miller, R.S., 1994, Hydrogeologic framework and preliminary simulation of ground-water flow in the Mimbres Basin, southwestern New Mexico: U.S. Geological Survey Water-Resources Investigations Report 94-4011, 118 p.

Harrill J.R. and Preissler A.M., 1994. Ground-water flow and simulated effects of development in Stagecoach Valley, a small, partly drained basin in Lyon and Storey counties, western Nevada. Professional Paper 1409-H. 83 p. https://pubs.er.usgs.gov/publication/pp1409H

Hawley, J.W., Hibbs, B.J., Kennedy, J.F., Creel, B.J., Remmenga, M.D., Johnson, M., Lee, M.M. and Dinterman, P., 2000, Trans-International Boundary aquifers in southwestern New Mexico: New Mexico Water Resources Research Institute, New Mexico State University, prepared for U.S. Environmental Protection Agency, Region 6, and International Boundary and Water Commission; Technical Completion Report-Interagency Contract X-996350-01-3, 126 p.

Heilweil, V.M., and Brooks, L.E., eds., 2010. Conceptual model of the Great Basin carbonate and alluvial aquifer system. U.S. Geological Survey Scientific Investigations Report 2010-5193, 191 p. https://pubs.usgs.gov/sir/2010/5193/

Heywood, C.E., 2002, Estimation of alluvial-fill thickness in the Mimbres ground-water basin, New Mexico, from Interpretation of isostatic residual gravity anomalies: U.S. Geological Survey Water-Resources Investigations Report 02-4007, 15 p.

Kennedy, J.F., Hawley, J.W. and Johnson, M.M., 2000, The hydrogeologic framework of basin-fill aquifers and associated ground-water-flow systems in southwestern New Mexico – an overview, in New Mexico Geologic Society Guidebook, 51st Field Conference, p. 235-244.

Kwicklis, E.M., A.V. Wolfsberg, P.H. Stauffer, M.A. Walvoord, and M.J. Sully. 2006. Multiphase, multicomponent parameter estimation for liquid and vapor fluxes in deep arid systems using hydrologic data and natural environmental tracers. Vadose Zone J. 5:934– 950. doi:10.2136/vzj2006.0021

Los Alamos Grid Toolbox, LaGriT, Los Alamos National Laboratory, (https://LaGriT.lanl.gov), 2020.

Love, D.W. and Seager, W.R., 1996, Fluvial fans and related basin deposits of the Mimbres drainage: New Mexico Geology, v. 18, p. 81-92.

Mack, G.H. and Stout, D.M., 2005, Unconventional distribution of facies in a continental rift basin: the Pliocene-Pleistocene Mangas Basin, south-western New Mexico: Sedimentology, v. 52, p. 1187-1205.

Mariner, P.E., Stein, E.R., Sevougian, S.D., Cunningham, L.J., Frederick, J.M., Hammond, G.E., Lowry, T.S., Jordan, S., and Basurto, E. 2018. Advances in Geologic Disposal Safety Assessment and an Unsaturated Alluvium Reference Case. SFWD-SFWST-2018-000509, SAND2018-11858 R.

PFLOTRAN (2020), https://www.pflotran.org/, last accessed July 23, 2020.

Rinehart, A., Timmons, S., Felix, B. and Pokorny, C., 2015, Groundwater level and storage changes – regions of New Mexico: Technical completion report by the New Mexico Bureau of Geology and Mineral Resources, Socorro NM, 40 p.

Sentis, M.L., Gable, C.W., 2017, Coupling LaGriT unstructured mesh generation and model setup with TOUGH2 flow and transport: A case study, Computers & Geosciences, 2017, DOI:doi.org/10.1016/j.cageo.2017.06.012.

Sevougian, S.D., Stein, E.R., LaForce, T., Perry, F.V., Lowry, T.S., Cunningham, L.J., Nole, M., Haukwa, C.B., Chang, K.W., and Mariner, P.E., 2019, GDSA Repository Systems Analysis Progress Report. M2SF-19SN010304051 SAND2019-5189 R.

Shepherd, M., 2009a, 3-D Geocellular modeling, in M. Shepherd, Oil field production geology: AAPG Memoir 91, p. 175-188.

Shepherd, M., 2009b, Geostatistical methods, in M. Shepherd, Oil field production geology: AAPG Memoir 91, p. 159-174.

Shepherd, M., 2009c, Analysis of rock properties, in M. Shepherd, Oil field production geology: AAPG Memoir 91, p. 99-105.

Sweetkind, D.S., 2017, Three-dimensional hydrogeologic framework model of the Rio Grande transboundary region of New Mexico and Texas, USA, and northern Chihuahua, Mexico: US Geological Survey Scientific Investigations Report 2017-5060.

Tearpock, D.J. and Bischke, R.E., 1991, Applied Subsurface Geological Mapping, Prentice Hall Inc., 648 p.

Thomas, J.M., Carlton S.M., and Hines L.B., 1989. Ground-water hydrology and simulated effects of development in Smith Creek valley, a hydrologically closed basin in Lander County, Nevada. Professional Paper 1409-E. https://pubs.er.usgs.gov/publication/pp1409E

Vorocrust, 2020, https://ip.sandia.gov/technology.do/techID=208, last accessed July 23, 2020.

Zyvoloski, G.A., B.A. Robinson, Z.V. Dash, S. Kelkar, H.S. Viswanathan, R. J. Pawar, P. H. Stauffer, T. A. Miller, S. Chu, 2015. Software Users Manual (UM) for the FEHM Application Version 3.1 - 3.X, Los Alamos National Laboratory document LA-UR-12-24493.

Zyvoloski, G. & Vesselinov, V., 2006, An Investigation of Numerical Grid Effects in Parameter Estimation: Ground water, v. 44, p. 814-825.